Tools and Methods Toward the Advancement of Flight Control for Flexible Aircraft

Jake D. Quenzer

A dissertation
submitted in partial fulfillment of the
requirements for the degree of

Doctor of Philosophy

University of Washington

2019

Reading Committee:

Kristi Morgansen, Chair

Mehran Mesbahi

Eli Livne

Program Authorized to Offer Degree:
William E. Boeing Department of Aeronautics and Astronautics

University of Washington

Abstract

Tools and Methods Toward the Advancement of Flight Control for Flexible Aircraft

Jake D. Quenzer

Chair of the Supervisory Committee:
Professor Kristi Morgansen
William E. Boeing Department of Aeronautics and Astronautics

Flight control of a flexible aircraft is a challenge that has become increasingly relevant over the last several decades. For the large twin-aisle commercial aircraft of today, automatic flight control systems are tasked not only with the traditional obligations of safe and stable flight with agreeable handling qualities for pilots, but are now additionally tasked with the mitigation of structural excursions (where objectives include load alleviation from disturbances including atmospheric turbulence and commanded maneuvers), as well as structural modal suppression (for improving ride quality and decreasing airframe fatigue), and may soon be responsible for the active suppression of aeroelastic flutter. These challenges strain or break the suitability of traditional system design and remedy-driven research efforts have been hampered by the scarcity of dynamics models in the public-domain as well as the cost, complexity, and delicate nature of corresponding experimental test beds. With regard to analysis, the multi-controller system architecture is a natural approach to many of the challenges described. In this work we investigate the robustness of stability guarantees for multi-controller systems via the switched system framework and quadratic common Lyapunov function. With regard to model scarcity, we present the development of the Generic Wide Body aircraft model and its simulation and evaluation environment. Finally, with regard to experimental cost and complexity, we present the development, fabrication, and validation of a low cost aeroelastic test bed.

TABLE OF CONTENTS

Page

List of Figures iii

List of Tables v

Chapter 1: Introduction 1
- 1.1 Literature Review 3
- 1.2 Organization 10

Chapter 2: Background and Preliminaries 12

Chapter 3: Extensions of the Quadratic Stability Margin 18
- 3.1 Characterizing Perturbations 18
- 3.2 Stability Convergence Rate 23
- 3.3 Control System Example 26

Chapter 4: Tolerable Perturbations in Multi-controller Systems 29
- 4.1 Constriction Method 29
- 4.2 Expansion Method 35
- 4.3 Switched System Generalization 40
- 4.4 Incorporating System Structure 43
- 4.5 Examples 48

Chapter 5: Generic Wide Body Model and Simulation Environment 57
- 5.1 Modeling Methods 58
- 5.2 Description 62
- 5.3 Analysis 69
- 5.4 Simulation 78

Chapter 6: Aeroelastic Test Article 81
  6.1 Development 82
  6.2 Modeling 90
  6.3 Pre-tunnel Testing 94
  6.4 Wind Tunnel Test 107

Chapter 7: Conclusion 117

Bibliography 119

Appendix A: Observable Canonical Form 127

LIST OF FIGURES

Figure Number Page

2.1 Examples of multi-controller control system architectures. 13

3.1 Depiction of the quadratic stability margin. 19
3.2 Sign conventions of aircraft longitudinal states and control input. 26
3.3 Traces of state magnitude with random system switching. 28

4.1 Gain margin problem formulation. 47
4.2 Sign conventions of aircraft longitudinal states and control input. 50
4.3 First mode shape of the Generic Wide Body model. 50
4.4 Perturbation bound from random sampling. 53
4.5 Comparison of controlled behavior in response to discrete gust. 55

5.1 Demensions of the Generic Wide Body aircraft. 62
5.2 Generic Wide Body structural stick model. 65
5.3 Generic Wide Body aerodynamic model and wing panel sectioning. 68
5.4 Longitudinal actuators of the Generic Wide Body aircraft. 70
5.5 Partitioning of aeroelastic aircraft dynamics. 77
5.6 Sample analysis of longitudinal flight dynamics. 77
5.7 Top level of the FACET Simulink diagram. 80
5.8 Variation in short period frequency and damping ratio. 80

6.1 Primary elements of the test article and mounting assembly. 83
6.2 Test article mounted in the wind tunnel test section. 84
6.3 Sample of structural optimization results. 87
6.4 Details of the test article aerodynamic configuration. 88
6.5 Details of the test article structural configuration. 90
6.6 General arrangement of sensors and actuators on the test article. 91
6.7 Finite element models of the test article. 93
6.8 Hardware configuration for servo system-identification tests. 95

6.9 Signal flow in servo command and measurement loop. 96
6.10 Signals used for servo system identification. 98
6.11 Estimated frequency response function and candidate transfer functions. . . 98
6.12 Time domain comparisons of transfer functions. 99
6.13 Primary elements of the vibration testing apparatus. 100
6.14 Changes in first wing bending frequency due to aero-shells. 103
6.15 Changes in first wing bending frequency due to foam and tip mass. 104
6.16 Changes in first wing bending damping due to foam and tip mass. 105
6.17 Elevator to wing-root strain transfer function of GVT model. 108
6.18 Power spectral density estimates used for frequency identification 109
6.19 Time histories used in dwell tests for damping ratio identification. 110
6.20 Damping ratio variation with dynamic pressure. 111
6.21 Movement of the rigid-body mode with increasing dynamic pressure. 113
6.22 Identified transfer functions and experimental frequency responses. 115
6.23 Gust input model comparison and transfer function to wing root strain. . . . 116

LIST OF TABLES

Table Number Page

3.1 State and control penalty weights used for LQR controller synthesis. 27

4.1 Tolerable perturbation size comparison for an individual dynamic system. . . 52

5.1 Weight build-up of the Generic Wide Body aircraft model. 66
5.2 Key geometry of the Generic Wide Body aerodynamic model. 69
5.3 Sample eigenvalues of the Generic Wide Body structural model. 71
5.4 Aerodynamic stability derivatives of the Generic Wide Body aircraft. 74

6.1 Overview of test article structural components. 89
6.2 Structural mode shapes of the test article. 94
6.3 Servo transfer function estimate results. 97
6.4 Equipment used in laser vibrometer experiments. 100
6.5 Wing beam properties. 102
6.6 Test configurations of foam-filler experiments. 103
6.7 Full test article structural vibration test results. 106
6.8 Post correlation structural mode shapes and frequencies. 106
6.9 Structural mode shapes and frequencies of the pitch-free model. 107

ACKNOWLEDGMENTS

This dissertation comes at the conclusion of nearly a decade spent working, learning, and growing in the Nonlinear Dynamics and Control Lab. For her support and guidance that began with my first involvement as an undergraduate volunteer, I am sincerely thankful to Professor Kristi Morgansen. The opportunities she has provided over these many years - covering the full spectrum of control theory, modeling, software, hardware, and experiment - have been instrumental to my development as a control engineer.

I am deeply appreciative of the community and camaraderie that I've had the good fortune to be part of in the Nonlinear Dynamics and Control Lab. In particular, I wish to thank Nathan Powel, Brian Hinson, Natalie Brace, Sierra Adibi, Brian Katona, Brian Beechinor, Kimber Hinson, Karine Chen, John Berg, and Alison Zongolowicz for their insights; both on the white board and beyond.

I am also thankful for the support and guidance our collaborators in this effort to improve flight control for flexible aircraft. Special thanks go to Bijan Barzgaran, Professor Mehran Mesbahi, and Professor Eli Livne of the University of Washington as well as Dr. Kioumars Najmabadi, Brian Rupnik, Gregory Clark, Alexander Ho, and Dr. Prachya Panyakeow of Boeing Commercial Airplanes.

Toward my parents, Dean and Debbie Quenzer, I cannot express an amount of gratitude commensurate with the pride and joy I have reaped from their support in all my life's pursuits. Finally, I am thoroughly indebted to Maddie and Charlie for their patience and companionship, and for keeping me sane along the way.

Chapter 1

INTRODUCTION

Aeroelasticity, the interaction between structural deformations and aerodynamic forces, has played a key role in aviation since the beginning of powered flight: wing-warping employed by the Wright brothers for flight control is often noted as a major milestone on their path to success [1]. Following the Wrights' achievement, hinged control surfaces supplanted wing-warping designs and the trend in aviation over the majority of the 20th century was to build airframes as rigidly as weight constraints would allow. Consequently, theory and practice of aircraft stability and control were born under the premise of rigid airframes [2].

In the second half of the 20th century analytic study began to catch up with experimental achievements in aviation; in the 1960s analytic treatments of the dynamics for deformable aircraft were developed [3, 4]. Shortly thereafter, the 1970s brought about a ubiquity of flight control augmentation [2], and research began toward the development of control system features to address undesirable aeroelastic behaviors [5, 6, 7]. Such features include Maneuver Load Alleviation (MLA), Gust Load Alleviation (GLA), and Structural Mode Control Systems (SCMS). All the while, traditional requirements for safe and stable flight were never relaxed but rather became even more challenging to satisfy; increased flexibility in modern aircraft exacerbates the difficulty of designing a complete control system to simultaneously address both traditional and contemporary requirements. Research efforts persist with encouragement from advancements in actuation (e.g., [8]), sensing (e.g., [9, 10]), and control law synthesis (e.g, [11, 12]). However, the problem is not yet "solved" and the challenge is likely to intensify with active flutter suppression looming on the horizon as yet another flight control system responsibility [13].

Through the course of even a nominal flight the modern flight control system is expected to satisfy the performance objectives just described in the face of uncertain and changing plant dynamics. For example, flight dynamics are influenced by the movement of an aircraft's center of gravity as fuel burns. While there exist control synthesis techniques such as linear parameter varying controllers and model reference adaptive control that aim to address plant and objective variations directly, the monolithic controllers they yield have not been widely adopted [14]. The traditional engineering approach has been to decompose the control problem into a finite set of design points where numerous combinations of control objectives and vehicle dynamics are addressed individually; gain schedules or control switching logic are then employed to transition the control system through these point-wise designs as appropriate for a given instant in flight. This point-wise design approach (multi-controller architecture) remains the practical choice for designers [15].

One of the remaining shortcomings in the multi-controller architecture is a lack of guarantees for time varying behavior that occurs during the transition from one design point to the next. The switched system framework is well suited for representing multi-controller architectures and provides tools for the definition and assessment of stability for such systems. For example, common nonlinearities such as actuator dead-zone and saturation have been cast in a switched system representation for stability and performance analysis using quadratic and non-quadratic Lyapunov functions [16]. The Quadratic Common Lyapunov Function (QCLF) is of primary interest in this work because of its relative simplicity in computation and its accommodation of arbitrary system switching.

By itself the QCLF is suited to guarantee stability for a flight control system that makes use of a multi-controller architecture. A guarantee of stability for any control system is subject to the question of robustness: is the guarantee valid if the system dynamics are subject to some real parameter variation? Note that this question differs from that addressed by stability measures such as gain/phase margin or the H_∞-norm for Linear Time Invariant (LTI) systems; these measures indicate variation required to destabilize the system. For a switched system the mechanism of instability is the switching signal, i.e., the order and timing of changes to the system dynamics. In this work we supplant the question of variation required to cause instability with one of variation required to invalidate a stability guarantee.

Beyond analysis there is the question of verification through simulation and validation through experiment. The cost of flight testing new aeroelastic control technologies at full scale is prohibitive. Flight testing of small UAVs can be more affordable but the method suffers from its own challenges regarding scaling, hardware, and flight operations. In both cases obtaining desired disturbance inputs in a repeatable way is challenging; so too is manipulation of the environment and parameters in which aeroelastic control systems are tested. Wind tunnel tests for control studies offer, with adequate wind tunnel gust generation systems, controlled and repeatable environments for controller tests at lower costs than flight tests [17, 18]. Still, construction and experiments with large aeroservoelastic models at wind tunnels such as the NASA Transonic Dynamic Tunnel (TDT) or large low-speed tunnel can be challenging regarding costs, design and construction schedules, and test schedules. There is, therefore, a need for small-scale aeroservoelastic models of flight vehicles for control technology tests that would represent the key physical mechanisms and would allow rapid access at low cost.

1.1 Literature Review

The contributions in this work divide largely into two categories: methods and tools. The literature review is divided accordingly. In the first section we review the landscape of methods in characterizing robustness of stability guarantees for multi-controller systems. In the second section we discuss the state of affairs regarding dynamic models and test beds available to the academic community that support the research and development of aeroelastic control systems. Additionally, a third section summarizes the publication history of the author and the context those works provide to this dissertation.

1.1.1 Multi-controller Systems and Robustness of Stability

While one of the goals in this work is to analyze the robustness of stability for a switched linear system, the methods draw inspiration and context from the analysis of stability robustness for an individual system. Hence, we start with a discussion of analysis methods for individual systems to build that context. There exist a variety of methods to analyze the robustness of stability for Linear Time Invariant (LTI) dynamical systems; variety of analysis methods stems from the variety of ways in which system uncertainty can be expressed. A large subset of control theory is built around the prescription of uncertainty in the frequency domain; e.g., H_∞ analysis and μ-synthesis [19]. For the switched linear system representation of a multi-controller system (as we will review shortly), the mechanism of instability has to do with time varying behavior of a system due to switching. The sensitivity of that behavior is closely tied to the particular time-domain realization under consideration. Consequently, analysis of uncertainty prescribed in the time domain (associated with the realization of choice) is the domain of interest in this work.

For uncertainty prescribed in the time domain, the predominant measures of robustness are the real and complex stability radii [20, 21]. The real stability radius will be detailed in Chapter 2. Briefly, the radius is meant to measure the distance between a given stable system and the set of unstable systems.[1] The complex stability radius is actually related to the inverse of the H_∞-norm of an LTI system and is thus relatively easy to compute. The primary drawback of the complex radius is the same as that of the H_∞-norm: the complex perturbations admitted lack physical interpretation. As summarized in [22], in most studies of system uncertainty complex perturbations are not of direct interest but are begrudgingly utilized as larger sets that include the real perturbations of interest. On the other hand, the real stability radius supplies a result with more direct utility, but is notoriously more difficult to compute [23].

If an individual LTI system with state space realization (A, B, C) is stable, then there are necessarily positive definite matrices P and W that satisfy the Lyapunov equation,

$$A^{\intercal}P + PA = -W. \tag{1.1}$$

---

[1] From that description, one may be reminded of plotting system poles in the complex plane and identifying the pole nearest the imaginary axis. It has been shown that such a distance is a misleading measure of robustness; it was shown that a stable transfer function, under some common assumptions, can be realized with arbitrarily high sensitivity to perturbation [20].

In the 1980s a number of articles were written regarding the sensitivity of the Lyapunov equation to perturbations of each constituent matrix [24, 25, 26, 27]. In the latter works, the authors recognized the utility of considering only perturbations to the system matrix and the corresponding interpretation of a robustness measure. In these cases the authors are able to provide bounds on the size of tolerable system perturbations under various norms, but the bounds provided are notably conservative because of the consideration of complex system perturbations and restrictions on the set of quadratic Lyapunov functions considered.

Also in the realm of perturbations in the time domain, there are a variety of results corresponding to polytopic system uncertainty of the form

$$A(z) = A_0 + \sum_i z_i A_i. \tag{1.2}$$

As noted in [28], the question of interest in these results is to test for the existence of a parameter dependent quadratic Lyapunov function,

$$A(z)^{\intercal} P(z) + P(z)A(z) \prec 0. \tag{1.3}$$

Broadly speaking, the goal then becomes to maximize some measure of size of the parameter vector $\vec{z}$ while simultaneously searching for $P(z)$ that guarantees stability. As noted in [28], this problem of determining maximum polytopic robustness is known to be NP hard. Restricting the perturbations to a hypercube allows the computation of a robustness measure based on the determination of the largest system hypercube (centered at A_0) that can be proven stable with a quadratic Lyapunov function [29]. The robustness measure obtained using the expansion method in Chapter 4 is notionally similar, but regards maximum parameter expansion under an assumed quadratic Lyapunov function.

The multi-controller architecture remains a widely adopted approach for gain scheduled and variable-objective control systems [14, 30, 31, 32]. The switched system framework is recognized for its suitability in representing and providing analysis for the multi-controller architectures, but this practice is not as widely adopted and there remain open questions about how best to utilize the framework [33]. For example, rather than assume an arbitrary switching between controllers, there is a question of crafting an optimal switching signal to achieve some blend of objectives. This notion brings us to the landscape of stability results in the switched system framework.

The results regarding stability and stabilization of switched linear systems are numerous [34]; here the variety stems largely from differing assumptions about switching behavior. The three overall categories of assumption are: arbitrary system switching, constrained switching, and controlled switching. Of these, the arbitrary switching assumption is most appropriate for analysis of multi-controller architectures because it is free of any restriction on the mechanism of switching (for example a pilot or outer-loop digital logic). Within this category, the standard definition of stability for a switched linear system (detailed in Chapter 2) is Global Uniform Exponential Stability (GUES). Measures of robustness for that stability depend on the method by which the nominal system is proven GUES. For example, its noted in [35] that a Lie algebraic condition may be used to prove a system GUES, but that the method is not amenable to sensitivity analysis.

The Quadratic Common Lyapuov Function (QCLF) alluded to previously is an extension to switched systems of the quadratic Lyapunov function associated with an individual LTI system. In the field of switched system analysis the QCLF is somewhat downplayed because it provides only a sufficient condition for switched system stability, i.e., there exist stable switched systems for which no QCLF exists. Multiple Lyapunov functions and piecewise quadratic Lyapunov functions, are some of the alternatives to QCLFs developed in efforts to address its conservatism [36, 35].

There are however reasons to harness the QCLF in the case of multi-controller systems despite its conservatism. First, many control synthesis strategies produce controller transfer functions that are not realized in the time domain until final implementation on the digital computer of a flight vehicle. For a multi-controller system where the controllers are all defined in the frequency domain, it has been shown in [37] that there exist realizations for the controllers such that the resulting switched system has a QCLF. Thus, the concern of a QCLF existing for the multi-controller system is alleviated in many cases. Secondly, the stability guarantee of the QCLF survives the bi-linear transformation when converting the system from continuous to discrete time, as discussed in [38]. The advantage here is that design and analysis can be conducted in continuous time with results that remain valid in the discrete time implementation of a digital flight computer. Finally, the computation of a QCLF is constructed as a Linear Matrix Inequality (LMI). While LMIs are favorable to more general optimization formulations, they still suffer in growth of complexity with system size; however, alternative methods do exist which aim to relax the complexity concerns for larger systems [39, 40]. Finally a slight modification to the LMI construction for a QCLF gives a Generalized Eigen-Value Problem (GEVP) that provides both a QCLF and a lower bound on the exponential rate of decay for the system; yet another advantage of the QCLF over alternative common Lyapunov function formulations.

Toward the goal of quantifying real parameter variation tolerable under a QCLF, the Quadratic Stability Margin (QSM) was developed in [41]. The QSM has a nice geometric interpretation as the amount that a convex system polytope can be positively scaled about its center while remaining stable under a given QCLF. For a polytopic system description, this quadratic stability margin is the return value of MATLAB's "quadstab" algorithm.

1.1.2 Aeroelastic System Modeling and Evaluation

The landscape of tools available for aeroelastic control research is fragmented based on the underpinning mathematical model of flexible aircraft dynamics. The derivation in [3] builds complete aero-structural vehicle dynamics with rigid body and structural dynamics decoupled through the use of the "mean-axis" approximation (only the unforced dynamics are decoupled; coupling occurs through aerodynamic loads). The method assumes relatively small structural displacements and quasi-steady aerodynamics. Of course, the suitability of these assumptions depends on the behavior the model is meant to capture. These assumptions have been traditionally acceptable for the development of control system features such as load alleviation and ride quality management, as we will see later. This method has become the de facto standard, populating the pages of textbooks on flight dynamics [42], automatic flight control [43], and aircraft loads [44].

Alternative modeling techniques challenge either the assumption of linear structural dynamics, quasi-steady aerodynamics, or both. For example, the method in [45] is developed in light of rising interest for High Altitude Long Endurance (HALE) aircraft. These vehicles are extremely flexible and often depart from conventional aircraft configurations; span-loaded configurations tend to dominate the design space. As another example, in [46] the approach is to provide higher fidelity aerodynamic simulation for aeroservoelastic simulations. The higher fidelity dynamics that result from these and similar methods are generally too complex for use in control system design, especially for the case of large commercial aircraft where the assumptions of the original formulation are suitable.

The literature is not entirely devoid of full aero-structural aircraft models. The major drawbacks of most models used in the literature are that model details get withheld as proprietary information, the model details have been lost due to model reduction prior to publication, or the aircraft modeled exhibits aero-structural behaviors that differ greatly from that of a modern commercial aircraft. For example, an attractive model in the literature is the “AX-1” aircraft in [47]. However, the details of the model, and its Matlab/Simulink implementation, are withheld from publication and are not available for public use. Next, there is a Rockwell B-1 Lancer model encapsulated in the Flexsim project in [48]. Flexsim was developed with similar intent as the present effort, but at a time when the popular opinion was that supersonic transports like the Aérospatiale/BAC Concorde would dominate the forthcoming civil aviation landscape. The Flexsim project implements flight dynamics based on a B-1 model, but again, the actual model is not made available for manipulation or for alternative implementations of flight dynamics. The model of the Boeing B-52E Control Configured Vehicle (CCV) in [49] is a makeshift candidate for studying aero-structural interactions with flight controllers; however, the present concern is focused on airframes more closely resembling modern commercial aircraft.

The lack of publically available models capturing commercial aircraft dynamics is evident in a sampling of aeroelastic-control research efforts. For example, reduced order dynamics of the B-52 model have been resorted to for gust load alleviation studies in [50] and [51]. Stability augmentation for large flexible aircraft is the subject of [52], but the underlying model is not disclosed. Gust alleviation for the Airbus A-300 is detailed in [53], but the model is of course withheld. Finally a number of studies for gust load alleviation and shape optimization ([54] for example) have utilized NASA's Generic Transport Model (GTM). However, the GTM is based on a Boeing aircraft and its details are not publicly available.

Purely aerodynamic models are relatively abundant in the literature because they depend primarily on external geometry which is inherently open domain. Full aircraft structural models on the other hand are much less prevalent. This is likely because full aircraft structural dynamics have long been negligible for most flight control concerns. A full aircraft structural model can be found in [55] which corresponds to a fictitious "generic transport aircraft" that is similar in size and weight to the ATR-42 turbo-prop passenger aircraft. The lack of an accompanying aerodynamic model is not particularly problematic as one could be created to match the structure. However, the size and rigidity of the model yield a relatively large separation in rigid body and structural dynamic behaviors which detracts from its utility in aeroelastic control studies.

1.1.3 Previous Work

The impetus to analyze multi-controller architectures began with our work on observability-based guidance for vehicles with range-only localization [56, 57], and was re-emphasized in our development of the control system for an academic underwater glider [58] for which ascent and descent operational modes required stitched modes of control. Assuring stability for a switched system via QCLFs led to the question of tolerable perturbations to system dynamics. The existing measure of robustness for QCLF stability guarantees was the Quadratic Stability Margin (QSM); our effort in Chapter 3 to characterize tolerable system perturbations under a QSM was first published in [59]. In Chapter 4 we proceed to address system perturbations in arbitrary directions (i.e., without regard to the QSM) and consider the implications of different candidate norms for measuring those perturbations; these efforts are detailed in work submitted to the AIAA Journal of Guidance Dynamics and Control [60].

With regard to simulation and experimental efforts, our wind tunnel test experience in [61] and the combined hardware/software development experience gained in [62] were precursors to the efforts herein. Specifically, our software development and control architecture experience from [62] informed the design of the simulation and evaluation environment built around the Generic Wide Body aircraft model detailed in Chapter 5 and reported in the literature within [63]. Our lessons learned in wind tunnel tests from [61] steered many of the design decisions in the development of the aeroelastic test article developed in [64], as well as the gust generation system and real-time control apparatus that round out the aeroelastic test bed detailed in [65] (both of which are recounted in Chapter 6).

1.2 Organization

The work presented herein is organized as follows. Chapter 2 reviews the concepts of multi-controller architectures and the mathematical preliminaries surrounding the switched system framework. The quadratic stability margin is probed for its utility in describing tolerable system perturbations in Chapter 3; the analysis demonstrates the directions of tolerable perturbations under the QSM are restricted to the directions spanned by the polytope of the original system descriptions. In Chapter 4 perturbations of arbitrary direction are considered; the analysis objective is to bound the size of the arbitrarily-directed perturbations. Toward that goal Chapter 4 details two methods of analysis: the first applies a constriction approach to the set of intolerable perturbations, and the second applies an expansion approach to the set of tolerable perturbations. Both methods result in numerical optimization problems that grow in complexity with system dimension; the chapter demonstrates how structure imparted by typical system architecture can be used to simplify these optimization problems. Chapter 5 accounts the development of the Generic Wide Body aircraft model and its traits that make it suitable for the study and evaluation of automatic flight control systems for flexible aircraft. In Chapter 6 we detail the design, fabrication, and validation of a low-cost aeroelastic experimental apparatus. Finally, Chapter 7 provides some discussion of the results in this work and avenues of future investigation.

Chapter 2

BACKGROUND AND PRELIMINARIES

Consider the sampling of multi-controller system architectures depicted in Fig. 2.1; for each case the plant (and its variants) and the compensator (and its variants) are Linear Time-Invariant (LTI). The structure in Fig. 2.1a presents a traditional compensator-in-series architecture where several compensators have been designed to address variations in control objective. Alternatively, the structure in Fig. 2.1b is typical of a traditional gain scheduling approach in which a plant is linearized at a variety of critical design points and controllers are designed "point-wise" for each linearization. Of course, the notion of a multi-controller system is not restricted to a compensator-in-series architecture. Figure 2.1c depicts again a scenario where multiple controllers are designed to address variations in control objective where the architecture is the generalized system that underpins H_∞ and μ-synthesis techniques. For the purposes of this work, each of these architectures will ultimately lead to a family of closed loop dynamics (Fig. 2.1d). In Chapter 4 we will return to the original architectures to leverage simplifications from system structure; until then the family of closed loop dynamics is the focus of attention.

A family of closed loop dynamics results from the architecture in Fig. 2.1a though, for example, the following process: denote a state space realization of the plant dynamics as the matrix tuple (A_a, B_a, C_a), and denote the realization of a single set of compensator dynamics with (A_c, B_c, C_c, D_c). Finally, denote the state vector of the plant as x_a and the state vector of the compensator as x_c. The total state vector is a concatenation of the plant state and

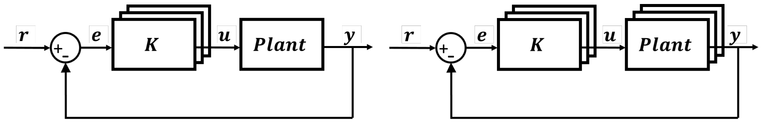

(a) Objective variation (b) Scheduling architecture

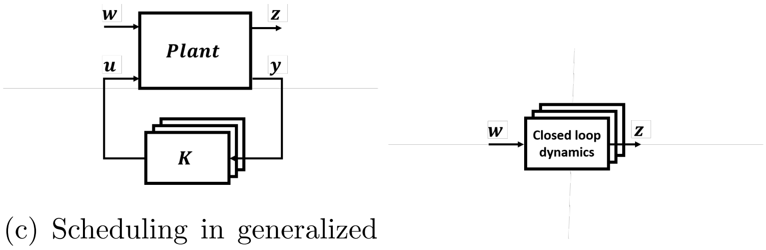

(c) Scheduling in generalized system (d) Closed loop equivalents

Figure 2.1: Examples of multi-controller control system architectures.

the compensator state, $x = [x_a^\intercal,\ x_c^\intercal]^\intercal$, and the closed loop system dynamics are expressed

$$\dot{x}(t) = \underbrace{\begin{bmatrix} A_a - B_a D_c C_a & B_a C_c \\ -B_c C_a & A_c \end{bmatrix}}_{A_{CL}} x(t). \tag{2.1}$$

With N compensators of the same order, the same process is used to produce N different instances of A_{CL}. Such a family of LTI systems is naturally represented as a switched linear system, defined as follows:

Definition 1 (Switched linear system)**.** *The time rate of change of a system state vector* $x \in \mathbb{R}^n$ *is given by*

$$\dot{x}(t) = A_{\sigma(t)} x(t) \tag{2.2}$$

where $\sigma(t)$ *is a piecewise constant function* $\sigma : [0, \infty) \to \mathcal{P}$*, and* $\mathcal{P}$ *is a finite index set,* $\mathcal{P} = \{1, 2, ..., N\}$*. For every index value* $p \in \mathcal{P}$ *the system matrix is of the same dimension,* $A_p \in \mathbb{R}^{n \times n}$*.*

The function $\sigma(t)$ is referred to as a "switching signal" and its purpose is to specify which set of dynamics are active at any given time. Additional details regarding properties of the switching signal (and of switched linear systems in general) can be found in [35]. There exist a variety of methods for characterizing the stability of (2.2) that stem from various assumptions about the switching signal and the nominal stability of each component system (again, see [35] for an overview). In this work, the motivation of multi-controller architectures suggests a pilot or outer-loop digital logic may be responsible for selecting the active set of dynamics and we are therefore encouraged to proceed under the assumption of *arbitrary* switching. In that case, the definition of stability for (2.2) is an extension of exponential stability:

Definition 2 (Global uniform exponential stability)**.** *If, for the solutions of the switched system* (2.2)*, there exist positive constants* $c, \lambda > 0$ *such that the inequality*

$$|x(t)| \leq c|x(0)|e^{-\lambda t} \tag{2.3}$$

holds for all $t \geq 0$*, for all initial conditions, and for all switching signals, then the system is Globally Uniformly Exponentially Stable (GUES).*

Because of the arbitrary switching condition it is necessary that every component system in (2.2) must itself be exponentially stable. One of the key concerns in switched system analysis is that even though (2.2) may be composed entirely of individually stable systems, the time-varying behavior introduced by switching can be destabilizing. To ensure stability in the face of switching, a sufficient condition for (2.2) to be GUES is for the system to admit a Quadratic Common Lyapunov Function (QCLF):

Theorem 1 (Quadratic common Lyapunov function [35])**.** *For the switched linear system* (2.2)*, if there exists a positive definite matrix* P *such that*

$$A_p^\intercal P + PA_p \prec 0, \quad \forall\, p \in \mathcal{P}, \tag{2.4}$$

then the switched linear system is GUES with the quadratic common Lyapunov function $V(x) = x^\intercal Px$*.*

In this definition and in the work to follow, the symbols $\prec$ and $\preceq$ are used to denote definite and semidefinite (respectively) relationships between symmetric matrices. For a switched linear system that possesses a QCLF, a lower bound can be established on the rate of exponential decay in system trajectories:

Definition 3 (Decay rate bound [41])**.** *Decay rate is defined as the largest α such that*

$$\lim_{t \to \infty} e^{\alpha t} \|x(t)\| = 0, \tag{2.5}$$

where $\|\cdot\|$ is the ℓ_2-norm of the state vector: $(x^\intercal x)^{1/2}$. The largest lower bound on the decay rate that can be found using a quadratic Lyapunov function can be found by solving the following generalized eigenvalue problem over a positive definite matrix P and scalar α,

$$\begin{aligned} \underset{\alpha, P}{\text{maximize}} \quad & \alpha \\ \text{subject to} \quad & A_p^\intercal P + P A_p + 2\alpha P \preceq 0, \ \forall \ p \in \mathcal{P}, \\ & P \succ 0. \end{aligned} \tag{2.6}$$

Next, the Quadratic Stability Margin (QSM) is a measure of the sensitivity of the GUES guarantee provided by a QCLF. As defined in [41], the margin makes use of a slightly different description of (2.2). The switched linear system so far has been described as explicitly allowing one of the component systems A_p to be active at any given time. As described in [35], the system can equivalently be expressed as a Linear Differential Inclusion (LDI)

$$A(t) \in \text{conv}\{A_1, A_2, ..., A_N\}, \tag{2.7}$$

where conv$\{\cdot\}$ is the convex hull of the component systems in $\mathbb{R}^{n \times n}$. This form describes a convex polytope according to its vertices; such a polytope can be equivalently described in an affine form where the vertices are defined with respect to the center of the poltope. For example, the set covn$\{A_1, A_2, ..., A_N\}$ is equivalently expressed with respect to a center system A_0 and vertex systems $\hat{A}_p$,

$$\dot{x}(t) = (A_0 + \hat{A}(t))x(t), \tag{2.8}$$

where $\hat{A}(t) \in \{\hat{A}_1, \hat{A}_2, ..., \hat{A}_N\}$. The quadratic stability margin is then defined as a permissible scaling of the system polytope in the affine form:

Definition 4 (Quadratic Stability Margin)**.** *For a polytopic linear differential inclusion* (2.8)*, the quadratic stability margin is the maximal value of a scalar, α, for which there exists a positive definite matrix P such that*

$$A_0^\intercal P + PA_0 + \alpha(\hat{A}_i^\intercal P + P\hat{A}_i) \prec 0, \quad i = 1, 2, ..., N. \tag{2.9}$$

As noted in [41], computing the QSM for a polytopic system is equivalent to a generalized eigenvalue problem; a problem for which numerical methods are well established. Finally, for an individual system (take one of the component systems of (2.2) for example), the real stability radius is a measure on the size of a system perturbation required to destabilize the system:

Definition 5 (Real stability radius [20])**.** *For a given stable system, $A \in \mathbb{R}^{n\times n}$, the real stability radius is defined as*

$$r_{\mathbb{R}}(A) := \inf\{\bar{\sigma}(\Delta) : \Delta \in \mathbb{R}^{n\times n} \textit{ and } (A + \Delta) \textit{ is unstable}\}. \tag{2.10}$$

There is a similar definition for the *complex* stability radius, $r_{\mathbb{C}}$, where the perturbation matrix is allowed to take on complex values, $\Delta \in \mathcal{C}^{n\times n}$. While the complex radius is significantly easier to compute, its allowance of complex perturbations lacks meaningful interpretation when characterizing allowable parameter variations in the state space representations of system dynamics. Whether (2.2) consists of a single system or many, the work to follow deals wholly in the consideration of *real* perturbations, i.e. system perturbations according to the following definition:

Definition 6 (Matrix perturbation)**.** *Suppose an LTI system (a component system of* (2.2) *for instance) with dynamics*

$$\dot{x}(t) = Ax(t), \tag{2.11}$$

where $x \in \mathbb{R}^n$ *and* $A \in \mathbb{R}^{n\times n}$*. This system is assumed globally exponentially stable with a quadratic Lyapunov function* $V(x) = x^\intercal Px$ *corresponding to a decay rate* α*. A real perturbation* $\Delta \in \mathbb{R}^{n\times n}$ *to this system yields perturbed dynamics*

$$\dot{x}(t) = (A + \Delta)x(t). \tag{2.12}$$

Chapter 3

EXTENSIONS OF THE QUADRATIC STABILITY MARGIN

The quadratic stability margin is a long known measure of robustness for the stability of a polytopic (switched linear) system. While the QSM has a nice geometric interpretation, it does not provide a readily interpreted result for a control system designer concerned about the size of tolerable perturbations to system dynamics. In this chapter we investigate the extent to which the long known QSM can provide information about tolerable system perturbations. After characterizing those perturbations, we discuss the tradeoff between the guarantee of perturbation size and the decay rate guarantee for the perturbed system. We conclude the chapter with a simple example involving longitudinal flight dynamics.

3.1 Characterizing Perturbations

The quadratic stability margin as just presented in Definition 4 is a scalar measure of tolerable set expansion. As alluded to in Chapter 1, a perturbation description of the margin is desirable for comparison to parameterized system uncertainty. Toward that goal, let us consider a "nominal" polytopic system;

Assumption 1. *There exists a switched system with an affine polytopic description as in* (2.8) *for which the quadratic stability margin is greater than unity* ($\alpha > 1$)*. The system polytope is the convex hull of* $N > 1$ *vertex systems (*N *finite).*

Because the assumed nominal system has a quadratic stability margin greater than one, the polytopic set

$$\Omega = \mathrm{conv}\{A_1, A_2, ..., A_N\} = A_0 + \hat{A}_p : \hat{A}_p \in \mathrm{conv}\{\hat{A}_1, \hat{A}_2, ..., \hat{A}_N\}, \tag{3.1}$$

can be expanded by scaling to include more systems. Define this expanded set as $\Omega_e : A_0 + \alpha \hat{A}_p$. The same QCLF applies to both sets Ω and Ω_e, which gives that both polytopic systems are GUES. Figure 3.1 depicts an example nominal and expanded polytope. Now we relate the nominal polytope to the expanded polytope in terms of a perturbation to the nominal system dynamics:

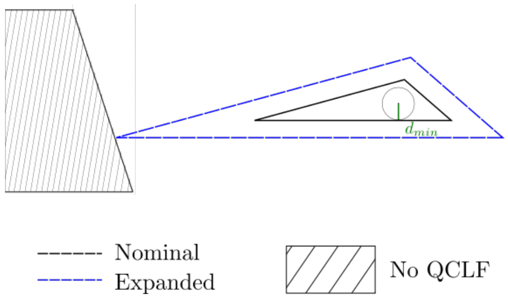

Figure 3.1: Depiction of the quadratic stability margin. The solid triangle represents the nominal system polytope and the blue dashed triangle represents the expanded set of systems. The diagonal hashing represents systems which, if included in the system polytope, do not permit a quadratic common Lyapunov function.

Problem 1. *What are the conditions on a matrix* $\Delta \in \mathbb{R}^{n \times n}$ *such that the perturbed dynamics of* (2.8),

$$\dot{x}(t) = (A_0 + \hat{A}(t) + \Delta)x(t), \tag{3.2}$$

are contained within the set Ω_e*, and are thus guaranteed GUES.*

The approach to Problem 1 is developed in two parts: first we determine the permissible directions of perturbations and then quantify a limit of perturbation magnitude. With respect to direction, we see that perturbations to Ω that yield systems in Ω_e must lie in the span of the points which define Ω.

Lemma 1. *Let* Ω *be the convex hull of* N *points* $\{X_1, X_2, ..., X_N\}$ *in* $\mathbb{R}^{n \times n}$*, and let* Ω_e *be a* *scaling of* Ω*. Given a point* $y \in \Omega_e$*, if* y *is expressed as*

$$Y = X + \Delta,\ X \in \Omega, \Delta \in \mathbb{R}^{n\times n}, \tag{3.3}$$

then $\Delta \in span\{X_1, X_2, ..., X_N\}$*.*

Proof. The point X can be expressed as

$$X = \sum_{i=1}^{N} \lambda_i X_i, \tag{3.4}$$

where $\sum_{i=1}^{N} \lambda = 1$ and $\lambda_i \in [0,\ 1]\ \forall\ i$. By definition, the point Y can similarly be expressed as

$$y = \beta \sum_{i=1}^{N} \hat{\lambda}_i X_i, \tag{3.5}$$

where the same conditions apply to $\hat{\lambda}_i$ as to λ_i and β is a scalar greater than one. Substituting (3.4) and (3.5) into (3.3) and rearranging, we have

$$\Delta = \sum_{i=1}^{N} (\beta\hat{\lambda}_i - \lambda_i) X_i, \tag{3.6}$$

which is an expression of Δ as a linear combination of the points $X_1, X_2, ..., X_N$; *i.e.*,

$$\Delta \in \text{span}\{X_1, X_2, ..., X_N\}. \tag{3.7}$$

□

Thus, we restrict the class of perturbations of (2.8) to those which lie in the span of the nominal systems, $\Delta \in \text{span}\{\hat{A}_1, \hat{A}_2, ..., \hat{A}_N\}$.

Having identified the subspace to which our perturbations must belong, we turn to the task of characterizing the allowable magnitude. As a first step, let us define the minimum distance from the center system of (2.8) to the boundary of the system polytope;

Definition 7 (Distance to boundary)**.** *For a polytopic system as in* (2.8)*, the minimum distance between the center and the boundary of the system polytope is*

$$d_{min} = \min_{x \in \partial P} \|x - X_0\|_F. \tag{3.8}$$

With Definition 7 in place, we proceed to the following result:

Theorem 2. *Let P be a convex $(N-1)$-polytope defined by a center X_0 and N affinely independent points in $\mathbb{R}^n$. Let P_e be the expanded polytope defined by a pure scaling of P about its center by the value $\alpha > 1$. Then the minimum distance between the boundary of P and P_e is $(\alpha - 1)d_{min}$.*

Proof. The nominal polytope P is defined as the convex hull of a finite number of vertex points which means that P can be represented as the intersection of a finite number of half-spaces [66]. Thus, the boundary of P (and therefore the boundary of P_e) can be represented with a finite number of hyperplanes. Let the hyperplanes on the boundary of P be defined as

$$\partial P : \{a_i^\intercal x = b_i,\ i = 1, 2, ..., M\}, \tag{3.9}$$

for some finite integer $M \in \mathbb{Z}$, $a_i, x \in \mathbb{R}^n$, and $b_i \in \mathbb{R}$. The bounding hyperplanes of P_e are then

$$\partial P_e : \{c_i^\intercal x = d_i,\ i = 1, 2, ..., M\} \tag{3.10}$$

with $c_i \in \mathbb{R}^n$, and $d_i \in \mathbb{R}$.

Now take an arbitrary point on ∂P_e and call it x_e. The point on ∂P with minimal distance to x_e must lie on one of the hyperplanes of P. Because P_e is a scaling of P, the two geometries are similar and each hyperplane on the boundary of P_e is parallel to a corresponding hyperplane of P, *i.e.*, there exists an ordering such that $a_i/\|a_i\| = c_i/\|c_i\|\ \forall\ i$.

Now, let x_e belong to a particular hyperplane $\hat{c}x = \hat{d}$. The corresponding hyperplane on ∂P is $\hat{a}x = \hat{b}$. Due to the definition of a convex polytope, every point in P must lie to one side of the hyperplane, $x \in P \to \hat{a}^\intercal x \leq \hat{b}$. Because P_e is an expansion of P it must be that $\hat{a}^\intercal x_e > \hat{b}$. Thus no point in P can be closer to x_e than a point on the hyperplane $\hat{a}^\intercal x = \hat{b}$.

Because $a_i^\intercal x = b_i$ and $c_i^\intercal x = d_i$ are parallel, the minimum distance possible between a point $a_i^\intercal x = b_i$ and a point on $c_i^\intercal x = d_i$ is the distance between the two planes. Thus, for any arbitrarily chosen point on ∂P_e, the minimal distance from that point to a point on ∂P is simply the distance between the associated hyperplanes on ∂P_e and ∂P.

Our next point concerns the scaling and relative distances of hyperplanes to the center of the polytope. In that context, note that the geometry and size of polytope are translationally invariant [66], which means that we can shift the nominal and centered polytopes to be centered at the origin so that $X_0 = 0$. For every hyperplane $a_i^\intercal x = b_i$ and $c_i^\intercal x = d_i$, let us assume that a_i and c_i have been normalized to unit magnitude. Taking the ordering that matches parallel hyperplanes gives $a_i = c_i$. The magnitude of a hyperplane's normal vector where it intersects the hyperplane identifies the minimal distance between the origin and the hyperplane. That distance is b_i and d_i for the hyperplanes respectively defined by $a_i^\intercal x = b_i$ and $c_i^\intercal x = d_i$. Because $a_i = c_i$ are normal vectors, the difference in distance of the two planes from the origin is the distance between the planes, *i.e.* the distance between the planes is

$$r_i = d_i - b_i. \tag{3.11}$$

Recall that the outer polytope is a result of scaling the inner polytope, so points that satisfy $y : c_i^\intercal y = d_i$ must be scaled versions ($y = \alpha x$) of points that satisfy $a_i^\intercal x = b_i$. Thus we substitute $y = \alpha x$ to get

$$c_i^\intercal y = d_i \rightarrow a_i^\intercal \alpha x = d_i \rightarrow a_i^\intercal x = \frac{d_i}{\alpha}. \tag{3.12}$$

Thus, for the two parallel hyperplanes we get that $d = \alpha b$. Substituting this result into (3.11) gives the distance between hyperplanes as

$$r_i = (\alpha - 1) b_i. \tag{3.13}$$

The pair of hyperplanes with minimum distance between them is the pair for which the inner hyperplane has the smallest distance to the origin b_i. Define the minimal value of b_i over all the hyperplanes in ∂P as d_{min}. The result is that the minimum distance between ∂P_e and ∂P is $(\alpha - 1) d_{min}$. □

In the proof of Theorem 2, we have taken for granted that the value of d_{min} is known. This distance can be computed for any convex polytope, but the computation may be rather expensive. The expense is due to the complexity of the so called "facet enumeration problem" which must be completed in order to change the representation of the polytope from a vertex representation to a hyperplane representation. The redeeming quality of the scenario at hand is that polytopic systems generated by switched controllers generally consist of a low number of vertex systems for which the facet enumeration problem is not likely to be overwhelming. Also note that Theorem 2 operates on a polytope defined in $\mathbb{R}^{n^2}$ while the system polytope is defined in $\mathbb{R}^{n\times n}$. To apply the result we simply perform the linear vec$(\cdot)$ operator on the matrix vertex points, i.e., stacking the columns of a matrix to produce a vector.

The minimum distance result of Theorem 2 is the approximation we take in bounding perturbations to the switched system (2.8). From the polytope depicted in Fig. 3.1, it is evident that perturbations of larger magnitude could be applied to a large number of other systems in the original polytope without exceeding the expanded set. In that sense, the perturbation size limitation established can be relatively conservative. We can seek to measure that conservatism by comparing the distance d_{min} with the distance from the polytope center to the farthest vertex point of the original polytope:

$$\eta = \frac{\max_i \|\hat{A}_i\|_F}{d_{min}}. \tag{3.14}$$

Large values of the conservatism measure result when the perturbation bound is small relative to the furthest vertex of the polytope.

3.2 Stability Convergence Rate

Let us return briefly to the key feature of the GUES guarantee; that the quadratic common Lyapunov function for the nominal system guarantees some degree of exponential stability. The specific degree of exponential stability can be quantified by a minimum guaranteed decay rate c. Recall from Definition 3, the largest lower bound on the decay rate provable with a QCLF can be determined by the solution to the linear matrix inequality,

$$A_i^\intercal P + PA_i + 2cP \leq 0, \quad i = 1, 2, ..., N. \tag{3.15}$$

We substitute the centered polytope description of our system dynamics to the LMI:

$$A_0^\intercal P + PA_0 + \alpha(\hat{A}_i^\intercal P + P\hat{A}_i) + 2cP \leq 0, \quad i = 1, 2, ..., N. \tag{3.16}$$

Here we recognize the inherent trade-off between the expansion of the nominal polytope and the remaining decay rate guaranteed by the QCLF. That is to say, when we compute the full value of the quadratic stability margin and proceed to characterize that margin by perturbations to the original system, the resulting switched system with the perturbations added is guaranteed to be exponentially stable, but the decay rate guaranteed can be vanishingly small.

Theorem 3. *For a given system polytope, Ω, that has an established quadratic stability margin $\alpha > 1$ and decay-rate lower bound c, the partially expanded set $\gamma\Omega$ with $1 < \gamma \leq \alpha$, has a decay rate $c_\gamma < c$.*

Proof. Take Ω to be the switched system of Assumption 1. The nominal system has a decay rate bound determined by maximizing c subject to the constraints in (3.16) with $\alpha = 1$. If c has been maximized then the equality of the expression has been reached, else a larger valid value of c exists. We analyze the equality by grouping terms:

$$\underbrace{A_0^\intercal P + PA_0}_{T_1} + \underbrace{A_i^\intercal P + PA_i}_{T_2} + \underbrace{2cP}_{T_3} = 0. \tag{3.17}$$

By default the first term is negative definite $T_1 < 0$, else the nominal polytopic system would not admit a QCLF. Also, by the definition of P and c, the third term is positive definite, $T_3 > 0$. Nothing can be said immediately about the definiteness of T_2. However, T_2 is symmetric, and every symmetric matrix can be expressed as the sum of a positive definite matrix and a negative definite matrix, respectively denoted T_2^+ and T_2^-. Recall that the polytopic system has a finite quadratic stability margin. This property means that for one of the vertex systems,

$$A_0^\intercal P + PA_0 + \alpha(\hat{A}^\intercal P + P\hat{A}) < 0. \tag{3.18}$$

However, the inequality no longer holds for a scaling of $\alpha + \epsilon$ where $0 < \epsilon$. The term $A_0^\intercal P + PA_0$ must be negative definite for the nominal switched system to be stable. The remaining terms on the left hand side of (3.18) are a particular instance of the term T_2 from (3.17). For the critical value of α, the left hand side of (3.18) can be written as

$$T_1 + \alpha T_2^- + \alpha T_2^+ < 0. \tag{3.19}$$

Given that $\alpha+\epsilon$ invalidates the inequality, and T_1 is fixed, it must be the case that $T_2^+ + T_2^- > 0$. Taking the same vertex system in the partially expanded polytope ($1 < \gamma < \alpha$), we see that $T_2^+ + T_2^- > 0$ provides a positive contribution to the left hand hand side of the equality

$$A_0^\intercal P + PA_0 + \gamma(\hat{A}^\intercal P + P\hat{A}) + 2cP = 0. \tag{3.20}$$

Thus, the equality can only be maintained if the decay rate bound, c, is decreased, i.e., $c_\gamma < c$. □

From this result, we recognize that the perturbation magnitude established in Sec. 3.1 may not be as useful in its original form because the perturbations it permits may cause the system to have exceedingly small lower bounds on the decay rate of the exponential stability. However, because we have already assumed the polytopic system has a finite quadratic stability margin, α, and associated QCLF, $V = x^\intercal P^\star x$, we can now specify a desired decay rate guarantee and test to see if there is a corresponding acceptable scaling of the nominal system.

Remark. *Let $P = P^\star$ for a nominal switched system (2.8), and let the desired fixed value of decay rate be c_{des}. If the optimization problem*

$$\begin{aligned}
&\underset{\tilde{\alpha}\in\mathcal{R}_+}{\mathit{maximize}} \quad \tilde{\alpha} \\
&\mathit{subject\ to} \\
&\qquad A_0^\intercal P^\star + P^\star A_0 + \tilde{\alpha}(\hat{A}_i^\intercal P^\star + P^\star \hat{A}_i) + \\
&\qquad 2c_{des}P^\star < 0, \quad i = 1, 2, ..., N
\end{aligned} \tag{3.21}$$

is feasible, then $1 \leq \tilde{\alpha} \leq \alpha$. *If the problem is infeasible, then the desired value of decay rate cannot be obtained.*

Our new, intermediate, value of the stability margin can now be used in place of α in the process described in Sec. 3.1 to provide a restriction on the admissible perturbations to the nominal system such that the resulting switched system not only has a GUES guarantee, but that it has a GUES guarantee with a decay rate no less than the desired c_{des}.

3.3 Control System Example

To demonstrate the application of the perturbation form of the quadratic stability margin, we consider the multi-controlled behavior of the longitudinal dynamics of a conventional aircraft. In a state-space description of the linearized longitudinal dynamics, the state vector is $x = [u,\ \alpha,\ \theta,\ q]^\intercal$ where u is the linear velocity along the body x-axis, α is the angle of attack, θ is the vehicle's pitch angle, and q is the pitch rate. The input to the system is an elevator deflection angle δ_e. Sign conventions for the states and their definitions with respect to the aircraft geometry are depicted in Fig. 3.2.

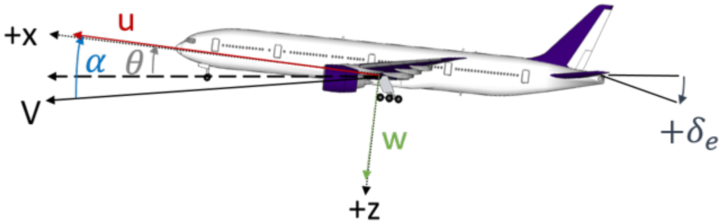

Figure 3.2: Sign conventions of aircraft longitudinal states and control input.

The data used to populate the dynamics model come from the Generic Wide Body aircraft model (will be detailed in Chapter 5). Consider a switched control system composed of full state feedback controllers $K_i,\ i = 1, 2, 3$, where each gain matrix is the result of an LQR controller synthesis. The simplified cost functions for the three controllers are

$$J(x, u) = \int_0^\infty x(t)^\intercal qIx(t) + ru^2(t)dt, \tag{3.22}$$

where I is an $n \times n$ identity matrix. The values of q and r used to synthesize the three controllers are listed in Table 3.1. The costs were not chosen to satisfy any particular design requirement, but the variation of cost between state and control signals demonstrate controllers developed with differing emphasis. The closed loop dynamics for each of the control systems can be expressed as

Table 3.1: State and control penalty weights used for LQR controller synthesis.

Controller	q	r
K_1	2	1
K_2	1	1
K_3	1	2

$$\dot{x}(t) = (A - BK_i)x(t), \quad i = 1, 2, 3. \tag{3.23}$$

Define the vertex points of the system polytope as $X_i \in \mathbb{R}^{4\times4} : \{A - BK_i, i = 1, 2, 3\}$, and the center of the polynomial as $X_0 = \frac{1}{3}\sum_i X_i$. This polytopic system has a quadratic common Lyapunov function with a quadratic stability margin of $\alpha = 2.457$. We proceed to center the nominal polytope, and enumerate its bounding hyperplanes. In this case, the polytope is a 3-polytope in $\mathbb{R}^{16}$. After enumerating the facets of the 3-polytope, the minimal distance from the origin to a point on any of the bounding hyperplanes was found to be $d_{min} = 0.0105$, yielding a maximal perturbation magnitude of 0.0152.

The exponential decay rate guaranteed for the nominal system was 0.27. As a spot test of the result, a perturbation with $\|\Delta\| = 0.0152$ was generated with a random direction within the perturbation space and added to each of the corner systems. For all perturbed systems, the Lyapunov inequality held and the perturbed system dynamics were Hurwitz. In addition, the system was simulated several times from the same initial condition with random controller switching sequences to demonstrate the compliance of the switched system with the exponential decay rate guarantee. The trajectories resulting from those simulations are depicted in Fig. 3.3.

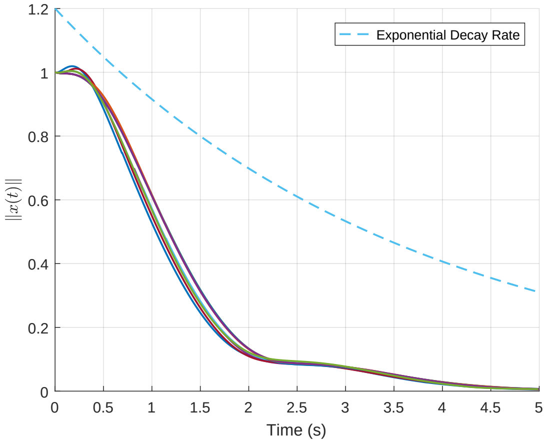

Figure 3.3: Traces of the state magnitude produced by initial condition responses with random control system switching.

From these results, a designer could incorporate system uncertainty in the closed loop dynamics expressions to see if the expected uncertainty falls within the span of admissible perturbations and if so, if they are of acceptable magnitude to preserve the system's GUES guarantee.

Chapter 4

TOLERABLE PERTURBATIONS IN MULTI-CONTROLLER SYSTEMS

In Chapter 3 our focus was to characterize the direction and size of perturbations that a switched system could tolerate, according to the previously defined quadratic stability margin. In contrast, the effort here is directed at the more general question of how large perturbations can be if taken in any direction. We approach the question with two different methods: first by considering the set of intolerable perturbations and constricting down in size to find the smallest of its kind. In the second method we approach from the opposite direction and expand the size of tolerable perturbations to a maximum. The methods are developed against an individual LTI system for simplicity; the generalizations to switched linear systems are presented after both methods have been detailed. Both approaches yield numerical optimization problems which are subject to increased complexity with increased system dimension. We go on to demonstrate how problem structure from typical control system architectures can be used to reduce the optimization complexity for either method. The chapter concludes with some examples of the robustness metrics computed for a mixed objective flight control system.

4.1 Constriction Method

The approach in this section is analogous to the approach of the real stability radius: whereas the stability radius provides a bound on the size of perturbation needed to destabilize a system, we seek to provide a bound on the size of a perturbation needed to invalidate a stability guarantee:

Problem 2 (Tolerable perturbations via constriction)**.** *With respect to the nominal system* *and perturbation of Definition 6 and for a given norm on* $\mathbb{R}^{n\times n}$*, determine the greatest lower bound on* $\|\Delta\|$ *such that the perturbed dynamics* (2.12) *cannot be guaranteed exponentially stable with* $V(x)$*, i.e.,*

$$\inf\{\|\Delta\| : \dot{V} = (A+\Delta)^{\intercal}P + P(A+\Delta) \not\prec 0\} \tag{4.1}$$

The implication of obtaining the bound in Problem 2 is that for any smaller perturbation the perturbed system dynamics are guaranteed to be exponentially stable using the quadratic Lyapunov function $V(x) = x^{\intercal}Px$. In this section of the work we approach Problem 2 in two ways: a direct solution and a relaxation of the direct solution.

4.1.1 Direct Solution

The first result of the work is a direct approach to Problem 2. Toward that result we start with a lemma regarding the solutions of Problem 4.1.

Lemma 2. *The infimum of Problem 2 is achieved by some* $\Delta \in \mathbb{R}^{n\times n}$.

Proof. To start, define the set of perturbations that satisfy the condition $\dot{V} \not\prec 0$,

$$\mathcal{S} := \{\Delta \in \mathbb{R}^{n\times n} : (A+\Delta)^{\intercal}P + P(A+\Delta) \not\prec 0\}. \tag{4.2}$$

The matrix $\dot{V}$ is real and symmetric and thus has strictly real eigenvalues. The set condition requires at least the maximum of those eigenvalues be non-negative,

$$\bar{\lambda}((A+\Delta)^{\intercal}P + P(A+\Delta)) \geq 0. \tag{4.3}$$

Now, let us take $\hat{\Delta} \in \mathcal{S}$ and a scaling coefficient $k \in [0, 1]$. For the scaled perturbation $k\hat{\Delta}$ the time rate of change of the Lyapunov function can be written as a linear (continuous) function of k,

$$\dot{V} = f(k) = A^{\intercal}P + PA + k(\hat{\Delta}^{\intercal}P + P\hat{\Delta}). \tag{4.4}$$

The maximum eigenvalue of $\dot{V}$ is then

$$\bar{\lambda}(f(k)) = \bar{\lambda}(A^{\intercal}P + PA + k(\hat{\Delta}^{\intercal}P + P\hat{\Delta})). \tag{4.5}$$

Because the eigenvalues of a matrix vary continuously with the entries of that matrix [67], and because (4.5) is a composition of continuous functions, the maximum eigenvalue expressed in (4.5) is a continuous function. Now, because A is Hurwitz we have that

$$\bar{\lambda}(f(0)) < 0, \tag{4.6}$$

and from (4.3) we have that

$$0 \leq \bar{\lambda}(f(1)). \tag{4.7}$$

Thus, from the intermediate value theorem for continuous functions, there must exist a value of $\hat{k} \in [0,1]$ such that $\bar{\lambda}(f(\hat{k})) = 0$. This value is the minimum scaling for which $k\hat{\Delta} \in \mathcal{S}$. The homogeneity of norms gives the size of the minimally scaled perturbation as $\hat{k}\|\hat{\Delta}\|$. Because $\hat{\Delta}$ was taken as any element of $\mathcal{S}$, this process can be performed on all elements of $\mathcal{S}$. Define a new set $\mathcal{T}$ that is composed of the minimally scaled version of every element in $\mathcal{S}$. The size of every element in $\mathcal{S}$ is bounded from below by the size of the smallest element in $\mathcal{T}$. Because $\mathcal{T} \subset \mathcal{S}$ there can be no larger lower bound than the size of the smallest element in $\mathcal{T}$. Because $\mathcal{T}$ is defined by operating on elements of $\mathcal{S}$, the lower bound is achieved by some $\Delta \in \mathcal{S}$ and that perturbation yields $\bar{\lambda}(\dot{V}) = 0$. □

Given Lemma 2, the minimal sized perturbation of (4.1) can be assumed, which is necessary for the corollary to follow:

Corollary 1. *Let $\tilde{\Delta} \in \mathbb{R}^{n\times n}$ be the argument satisfying* (4.1)*, then nullity*$(\dot{V}) \geq 1$.

Proof. Note from the proof of Lemma 2 that the minimally sized perturbation in $\mathcal{T}$ requires there be some value of $k \in [0,1]$ such that

$$\bar{\lambda}(f(k)) = 0, \tag{4.8}$$

i.e., the maximum eigenvalue of $\dot{V}$ is zero. The implication follows directly,

$$\bar{\lambda}(\tilde{\Delta}^{\intercal}P + P\tilde{\Delta} + A^{\intercal}P + PA) = \bar{\lambda}(\dot{V}) = 0 \Rightarrow \text{nullity}(\dot{V}) \geq 1. \tag{4.9}$$

□

Equipped with Lemma 2 and Corollary 1 we can proceed to the first main result:

Theorem 4. *Consider the optimization problem over* $\Delta \in \mathbb{R}^{n \times n}$ *and* $\nu \in \mathbb{R}^n$,

$$\begin{aligned} \underset{\Delta,\nu}{\text{minimize}} \quad & \|\Delta\| && \text{(4.10a)} \\ \text{subject to} \quad & (A^\intercal P + PA + \Delta^\intercal P + P\Delta)\nu = \vec{0}, && \text{(4.10b)} \\ & \nu \neq \vec{0}. && \text{(4.10c)} \end{aligned}$$

The optimal value, denoted as γ*, is equivalent to the infimum of Problem 2.*

Proof. By definition, γ corresponds to the size of a perturbation $\Delta^\star$ that renders at least one of the eigenvalues of $\dot{V}$ equal to zero. Suppose this zero eigenvalue is not $\bar{\lambda}(\dot{V})$. The perturbation would belong to the set $\mathcal{S}$ defined in the proof of Lemma 2, but not to the set $\mathcal{T}$. By the method described in the proof of Lemma 2, the perturbation can be scaled by some value $k \in [0, 1)$ such that $\bar{\lambda}(\dot{V}) = 0$. In this case the range of k does not include 1.0 because the maximum eigenvalue was supposed here to be strictly greater than zero. The scaled perturbation that gives $\bar{\lambda}(\dot{V}) = 0$ would satisfy the criteria of the optimization stated for this theorem, and it would have norm $k\|\Delta^\star\| < \|\Delta^\star\|$ which contradictions the supposition that $\Delta^\star$ is the solution to the minimization problem. We can conclude that a perturbation $\Delta^\star$ corresponding to the solution of the stated optimization yields $\bar{\lambda}(\dot{V}) = 0$. Thus the perturbation $\Delta^\star$ satisfies the definition of the lower bound in Lemma 2 as a perturbation of minimum norm for which $\bar{\lambda}(\dot{V}) = 0$; which in turn implies the norm of $\Delta^\star$ is equivalent to the infimum of Problem 2. □

Remark. *If not for the nonzero constraint* (4.10c)*, the optimization problem of Theorem 4 would be a Bilinear Matrix Inequality (BMI) in* Δ *and* ν*. For the sake of implementation in a numerical optimization routine, a finite set of overlapping half spaces can be used to recast the problem as a set of BMIs. Denote* $\vec{e}_i$ *as the unit vector in the i-th direction of* $\mathbb{R}^n$*. A set* *of n BMIs are expressed as*

$$\begin{aligned} \underset{\Delta,\,\nu}{\text{minimize}} \quad & \|\Delta\| \\ \text{subject to} \quad & (A^\intercal P + PA + \Delta^\intercal P + P\Delta)\nu = \vec{0}, \\ & \vec{e}_i^\intercal \nu > 0, \end{aligned} \tag{4.11}$$

followed by another n problems in the opposing half-spaces,

$$\begin{aligned} \underset{\Delta,\,\nu}{\text{minimize}} \quad & \|\Delta\| \\ \text{subject to} \quad & (A^\intercal P + PA + \Delta^\intercal P + P\Delta)\nu = \vec{0}, \\ & \vec{e}_i^\intercal \nu < 0. \end{aligned} \tag{4.12}$$

The original problem is recovered as the point-wise minimum of the $2n$ solutions to (4.11) *and* (4.12)*.*

While methods for solving BMIs continue to improve, the result of Theorem 4 requires a global minimum to the stated optimization problem and BMI optimization problems do not inherently guarantee a global minimum. Thus a designer's confidence in the bound obtained will correlate with confidence in their global optimization tools.

4.1.2 Relaxed Problem

Given its relevance, we restate Weyl's Theorem here for completeness:

Theorem 5 (Weyl's Theorem [68])**.** *Let $A, B \in M_n$ be Hermitian and let the eigenvalues $\lambda_i(A)$, $\lambda_i(B)$, and $\lambda_i(A+B)$ be arranged in increasing order. For each $k = 1, 2, ..., n$ we have*

$$\lambda_k(A) + \lambda_1(B) \leq \lambda_k(A+B) \leq \lambda_k(A) + \lambda_n(B). \tag{4.13}$$

Theorem 6. *The solution to the following optimization problem provides a lower bound to the infimum of Problem 2,*

$$\begin{aligned} \underset{\Delta}{\text{minimize}} \quad & \|\Delta\| \\ \text{subject to} \quad & 0 \leq \bar{\lambda}(A^\intercal P + PA) + \bar{\lambda}(\Delta^\intercal P + P\Delta). \end{aligned} \tag{4.14}$$

Proof. Given a perturbation Δ, $\dot{V}$ can be expressed

$$\dot{V} = (A^{\intercal}P + PA) + (\Delta^{\intercal}P + P\Delta). \tag{4.15}$$

Using Weyl's Theorem, a bound on the maximum eigenvalue of $\dot{V}$ is given by

$$\bar{\lambda}(\dot{V}) \leq \bar{\lambda}(A^{\intercal}P + PA) + \bar{\lambda}(\Delta^{\intercal}P + P\Delta). \tag{4.16}$$

For a perturbation Δ to satisfy the condition in Lemma 2 that $\bar{\lambda}(\dot{V}) = 0$, the upper bound on its maximum eigenvalue must be at least zero. By enforcing the upper bound of (4.16) be non-negegative in the optimization, all perturbations in the set $\mathcal{T}$ of Lemma 2 are included in the feasible space of (4.14). Because the feasible space of (4.14) includes $\mathcal{T}$, the optimal value of (4.14) must be at least as small as the smallest norm of an elment in $\mathcal{T}$. Because the smallest element of $\mathcal{T}$ achieves the infimum of Problem 2, the solution to (4.14) is at least as small as (and is therefore a lower bound on) the infimum. □

This problem is conservative because the constraint enforces the maximum eigenvalue of $\dot{V}$ be possibly greater than zero; however, the minimizing value of Δ may not actually invalidate the condition $\dot{V} \prec 0$. The problem in (4.14) is a convex objective function subject to a concave constraint and is thus not a convex optimization. Yet, this problem may be more numerically tractable with higher confidence of a global minimum than the BMI approach. Finally, motivated by the desire for some assurance of a global minimum, we turn to the dual formulation of the optimization in Theorem 6:

Corollary 2. *Let the optimization problem prescribed in Theorem 6 be the primal problem. The dual problem is*

$$\max_{\mu} \min_{\Delta} \left(\|\Delta\| - \mu(\bar{\lambda}(\Delta^{\intercal}P + P\Delta) + \bar{\lambda}(A^{\intercal}P + PA)) \right), \tag{4.17}$$

where $\mu \in \mathbb{R}$ is a Lagrange multiplier. The solution to the dual problem is a lower bound on the infimum of Problem 2.

Proof. By formulation, the solution to a dual problem ($d^\star$) is a lower bound on the solution to the primal problem ($p^\star$). Because Theorem 6 demonstrates the solution to the primal problem is a lower bound on the infimum of Problem 2, it follows that $d^\star$ must also be a lower bound on the same. □

The advantage to the dual formulation is that it is necessarily convex and thus brings an assurance of a global minimum. The disadvantages are first that the lower bound adds additional conservatism in the result, and second that the norm in the objective function is not necessarily differentiable. A non-smooth objective may introduce more numerical difficulty than the concave optimization of the primal problem.

4.2 Expansion Method

In contrast to the constriction method we turn now to the opposite approach. Rather than determine the smallest intolerable perturbation, here we will expand a set of tolerable perturbations to its limit. First though we take a moment to re-define the system perturbation in a vector form so that the size of a perturbation will be measured with a vector norm in stead of an induced norm.

Definition 8 (Perturbation Map)**.** *Define an operator that maps a scalar $c \in \mathbb{R}$ to a particular entry (i, j) of an $n \times n$ matrix, i.e. $\mathcal{M} : \mathbb{R} \times \mathcal{I} \times \mathcal{I} \to \mathbb{R}^{n\times n}$ where $\mathcal{I}$ is an index set, $\mathcal{I} = \{1, 2, ..., n\}$. The operator $\mathcal{M}$ is defined*

$$\mathcal{M}(c, i, j) = K : \begin{cases} K_{p,q} = c & p = i, q = j \\ K_{p,q} = 0 & \textit{otherwise} \end{cases} \tag{4.18}$$

For a vector of scalars $\vec{c} \in \mathbb{R}^m$, let there be m corresponding i, j pairs. The shorthand notation $\mathcal{M}(\vec{c})$ is used to denote

$$\mathcal{M}(\vec{c}) = \sum_{k=1}^{m} \mathcal{M}(\vec{c}_k, \vec{i}_k, \vec{j}_k). \tag{4.19}$$

The definition of a system perturbation taken in Definition 6 is now replaced with one in which perturbations are defined in a vector space rather than a matrix space.

Definition 9 (Vector perturbation)**.** *Suppose an LTI system (a component system of* (2.2) *for instance) with dynamics*

$$\dot{x}(t) = Ax(t), \tag{4.20}$$

where $x \in \mathbb{R}^n$ *and* $A \in \mathbb{R}^{n \times n}$*. This system is assumed globally exponentially stable with a quadratic Lyapunov function* $V(x) = x^\intercal P x$ *corresponding to a decay rate* α*. A real perturbation is defined* $\vec{\delta} \in \mathbb{R}^m$ *which is mapped to a matrix perturbation* $\Delta \in \mathbb{R}^{n \times n}$ *as*

$$\Delta = \mathcal{M}(\vec{\delta}). \tag{4.21}$$

Thus, the perturbed system dynamics are again expressed

$$\dot{x} = (A + \Delta)x(t). \tag{4.22}$$

With these definitions in place, we can proceed to define the problem of sizing tolerable perturbations with an expansion. Note that in contrast to the constriction method where the choice of norm was left arbitrary, here we specifically identify the ℓ_1 norm in the problem statement.

Problem 3 (Tolerable perturbations via expansion)**.** *Determine the maximum value* $\beta \in \mathbb{R}$ *such that every vector perturbation with* ℓ_1 *norm less than* β *yields a negative definite time rate of change of the Lyapunov function* $V(x)$*,*

$$\max\{\beta : \dot{V} \prec 0 \ \forall \ \vec{\delta} \in \mathbb{R}^m \ \textit{with} \ \|\vec{\delta}\|_1 \leq \beta\}. \tag{4.23}$$

Problem 3 is addressed directly with the next theorem:

Theorem 7. *The maximum value* β *in Problem 3 is obtained as the solution to the optimization problem*

$$\begin{aligned} \underset{\gamma}{\text{maximize}} \quad & \gamma \\ \text{subject to} \quad & (A + \mathcal{M}(\gamma, i, j))^\intercal P + P(A + \mathcal{M}(\gamma, i, j)) \prec 0, \quad i = 1, 2, ..., m, \quad j = 1, 2, ..., m, \\ & (A - \mathcal{M}(\gamma, i, j))^\intercal P + P(A - \mathcal{M}(\gamma, i, j)) \prec 0, \quad i = 1, 2, ..., m, \quad j = 1, 2, ..., m. \end{aligned} \tag{4.24}$$

Proof. The conditions of β in Problem 3 are first that

$$\dot{V} \prec 0 \;\; \forall \; \|\vec{\delta}\|_1 \leq \beta, \tag{4.25}$$

and second that there be no greater constant for which the first condition is true. Toward the first condition: consider a perturbation $\vec{\delta}$ such that $\|\vec{\delta}\|_1 \leq \gamma$ where γ is the optimal value of (4.24). For any index $k = [1, 2, ..., m]$ we have by definition that $|\delta_k| \leq \gamma$, which allows us to express any element δ as $c \cdot \gamma$ where $c \in [-1, 1]$. As a result, the perturbation matrix resulting from $\vec{\delta}$ can be expressed as the following convex combination

$$\mathcal{M}(\vec{\delta}) = \sum_{k=1}^{m} c_k \mathcal{M}(\gamma, \vec{i}_k, \vec{j}_k) \tag{4.26}$$

The perturbed dynamics $A + \Delta$ are thus contained in a polytope formed by the $2m$ vertex systems expressed in the constraints of (4.24). Because $V(x) = x^\intercal P x$ satisfies the conditions of a quadratic common Lyapunov function for the vertex points it satisfies the same conditions for any system in the polytope and thus applies to the perturbed dynamics $A + \Delta$; we have that $\dot{V} \prec 0 \;\; \forall \; \|\vec{\delta}\|_1 \leq \gamma$.

Now assume $\beta > \gamma$. The definition of β implies a perturbation matrix $\Delta = \mathcal{M}(\beta, i, j)$ for any index (i, j) would yield $\dot{V} \prec 0$,

$$(A + \mathcal{M}(\beta, i, j))^\intercal P + P(A + \mathcal{M}(\beta, i, j)) \prec 0, \quad i = 1, 2, ..., m, \quad j = 1, 2, ..., m, \tag{4.27}$$

$$(A - \mathcal{M}(\beta, i, j))^\intercal P + P(A - \mathcal{M}(\beta, i, j)) \prec 0, \quad i = 1, 2, ..., m, \quad j = 1, 2, ..., m. \tag{4.28}$$

If the above conditions were true, β would be a scalar of greater value than γ that is also a feasible value according to the constraints of (4.24): a contradiction to the definition that γ is the optimal value of (4.24). Hence β can be no greater than γ, and γ thus satisfies the conditions of β. □

Note the first part of the proof of Theorem 7 leverages the property of a QCLF providing a stability guarantee for all the systems in a convex polytope; in this case the convex polytope is defined by its vertices. These vertices are the basis vectors of $\mathbb{R}^m$ scaled to length γ.

Instead of using these scaled basis vectors as the vertices, consider a polytope where each basis vector defines a face (supporting hyperplane). This description is precisely that of a hypercube in $\mathbb{R}^m$ with side length 2γ. The set of all perturbations that reside inside this hypercube are succinctly described with the ℓ_∞ norm,

$$\{\vec{\delta} \in \mathbb{R}^m : \ \|\vec{\delta}\|_\infty \leq \gamma\}. \tag{4.29}$$

Note, the set described this way is a ball in $\mathbb{R}^m$ under the ℓ_∞ norm. The perturbations described in Problem 3 constituted a ball in $\mathbb{R}^m$ under the ℓ_1 norm. The method of Theorem 7 was to maximally expand the ℓ_1-ball under the $\dot{V} \prec 0$ constraint. The same method can be applied to the ℓ_∞-ball of perturbations. First, the problem is restated with the new set:

Problem 4. *Determine the maximum value $\beta \in \mathbb{R}$ such that every vector perturbation with ℓ_∞ norm less than β yields a negative definite time rate of change of the Lyapunov function $V(x)$,*

$$\max\{\beta : \dot{V} \prec 0 \ \forall \ \vec{\delta} \in \mathbb{R}^m \ \textit{with} \ \|\vec{\delta}\|_\infty \leq \beta\}. \tag{4.30}$$

Again note that in Theorem 7 the vertices of the perturbation convex polytope were directly enumerated with the basis directions of $\mathbb{R}^m$. The constraints in Theorem 7 codify the requirement that $V(x) = x^\intercal P x$ be a QCLF for the full perturbation ball by enforcing $V(x)$ be a QCLF for the vertices. In order to repeat this process for the ℓ_∞-ball of perturbations, the vertices of the ball must be enumerated for expression as constraints. Denote the set of vertices for a hypercube in $\mathbb{R}^m$ as $\mathcal{V}$ where each vertex $\vec{v} \in \mathcal{V}$ has unit length as measured by the Euclidean norm, $\|\vec{v}\|_2 = 1$. Also, for a hypercube in $\mathbb{R}^m$ centered at the origin, denote the ratio of half-edge length to vertex length (both measured with Euclidean norm) as

$$k_{ev} = \frac{1}{\sqrt{m}}. \tag{4.31}$$

Finally, note that a hypercube in $\mathbb{R}^m$ has 2^m vertices [69]. Now we have sufficient notation to express the expansion method for the ℓ_∞-ball of perturbations:

Theorem 8. *Consider the optimization problem*

$$\begin{aligned} &\underset{\gamma}{\text{maximize}} && \gamma \\ &\text{subject to} && (A+\gamma\mathcal{M}(\vec{v})^\intercal P + P(A+\gamma\mathcal{M}(\vec{v})) \prec 0, \quad \forall\, \vec{v} \in \mathcal{V}. \end{aligned} \tag{4.32}$$

The maximum value β in Problem 4 is $\gamma \cdot k_{ev}$.

Proof. The proof here closely follows that of Theorem 7. The conditions of β in Problem 4 are first that

$$\dot{V} \prec 0 \;\; \forall \; \|\vec{\delta}\|_\infty \leq \beta, \tag{4.33}$$

and second that there be no greater constant for which the first condition is true. Toward the first condition: consider a perturbation $\vec{\delta}$ such that $\|\vec{\delta}\|_\infty \leq \frac{\gamma}{k_{ev}}$ where γ is the optimal value of (4.32). This condition restricts $\vec{\delta}$ to reside in a hypercube centered at the origin of $\mathbb{R}^m$ with edge length $2\frac{\gamma}{k_{ev}}$. The vertices of a hypercube in $\mathbb{R}^n$ centered at the origin are $v \in \mathcal{V}$. Because a hypercube is a convex polytope, and because every point within a convex polytope can be expressed as a convex combination of the polytope vertices, the perturbation vector can be written as a convex combination of the hypercube vertices,

$$\vec{\delta} = \sum_{k=1}^{2^m} c_k \gamma \vec{v}_k, \tag{4.34}$$

where $c_k \in [0 \;\, 1]$. The matrix form of the perturbation can thus be written as a convex combination of matrix perturbations corresponding to the hypercube vertices,

$$\mathcal{M}(\vec{\delta}) = \sum_{k=1}^{m^2} c_k \gamma \mathcal{M}(\vec{v}_k). \tag{4.35}$$

The perturbed dynamics $A + \Delta$ are thus contained in a polytope formed by the 2^m vertex systems expressed in the constraints of (4.32). Because $V(x) = x^\intercal P x$ satisfies the conditions of a quadratic common Lyapunov function for the vertex points it satisfies the same conditions for any system in the polytope and thus applies to the perturbed dynamics $A + \Delta$; we have that $\dot{V} \prec 0 \;\; \forall \; \|\vec{\delta}\|_\infty \leq \gamma$.

Now assume $\beta > \gamma$. The definition of β implies a perturbation matrix $\Delta = \mathcal{M}(\vec{v})$ for any $v \in \mathcal{V}$ would yield $\dot{V} \prec 0$,

$$(A + \gamma \mathcal{M}(\vec{v})^{\intercal} P + P(A + \gamma \mathcal{M}(\vec{v})) \prec 0, \quad \forall\ v \in \mathcal{V}. \tag{4.36}$$

If the above conditions were true, β would be a scalar of greater value than γ that is also a feasible value according to the constraints of (4.32): a contradiction to the definition that γ is the optimal value of (4.32). Hence β can be no greater than γ, and γ thus satisfies the conditions of β. □

Before moving on to the generalization of these results, consider the difference between these last two results. Whereas the consideration of perturbations under the ℓ_1 norm gave rise to an optimization problem with $2 \cdot m$ constraints, the ℓ_∞ norm resulted in 2^m constraints. Despite the larger number of constraints, the ℓ_∞ norm result is likely the more useful measure because of its interpretation as the amount of variation that can be applied to any entry of the system matrix. In fact, the ℓ_∞ norm result here bears most resemblance to the perturbation bound in [27]. The difference is that here the quadratic Lyapunov function can come from any solution to the Lyapunov equation whereas the bound in [27] necessitates the right hand side of (1.1) be twice the identity matrix.

4.3 Switched System Generalization

The results of Section 4.1 and 4.2 were developed under the consideration of an individual LTI system. Here, we address the extension of the prior results to a switched linear system such as (2.2). First, an update to the nominal system under consideration.

Definition 10 (Switched system perturbation)**.** *Suppose a linear switched system as defined in* (2.2)*. Assume the nominal is GUES with a quadratic common Lyapunov function* $V(x) = x^{\intercal} P x$ *corresponding to a decay rate* α*. A real perturbation is defined* $\vec{\delta} \in \mathbb{R}^m$ *which is mapped to a matrix perturbation* $\Delta \in \mathbb{R}^{n \times n}$ *as*

$$\Delta = \mathcal{M}(\vec{\delta}). \tag{4.37}$$

Thus, the perturbed system dynamics are expressed

$$\dot{x} = (A_p + \Delta)x(t), \quad p \in [1, 2, ..., N]. \tag{4.38}$$

To reflect the new nominal system, the statement of Problem 2 is modified as follows

Problem 5 (Tolerable perturbations to a switched system via constriction)**.** *With respect to the nominal system and perturbation of Definition 10 and for a given norm on* $\mathbb{R}^{n\times n}$*, determine the greatest lower bound on* $\|\Delta\|$ *such that the perturbed dynamics* (4.38) *cannot be guaranteed GUES with* $V(x)$*, i.e.,*

$$\inf\{\|\Delta\| : \dot{V} = (A_p + \Delta)^{\intercal} P + P(A_p + \Delta) \not\prec 0, \quad \textit{for some } p\} \tag{4.39}$$

Because the condition $\dot{V} \not\prec 0$ need only be satisfied for some $p \in \mathcal{P}$, the infimum can be determined for each component system and the greatest lower bound on the set of infimums is the minimum value of the set. In other words, the infimum of Problem 5 is determined by computing the infimum of Problem 2 for each component system and then selecting the minimum of those solutions. Thus, the optimization of Theorem 4 can be applied point-wise to the component systems of (2.2) to evaluate Problem 5. The same argument follows for the point-wise application of Theorem 6, and Corollary 2; as these optimizations provide a lower-bound on the infimum of Problem 2, so too does the minimum result of their point-wise lower bounds provide a lower bound to the infimum of Problem 5.

With regard to the expansion method, the problem statement is modified as follows:

Problem 6 (Tolerable perturbations to a switched system via expansion)**.** *Determine the maximum value* $\beta \in \mathbb{R}$ *such that every vector perturbation with* ℓ_1 *norm less than* β *yields a negative definite time rate of change of the Lyapunov function* $V(x)$ *for every component system of* (2.2)*,*

$$\max\{\beta : \dot{V}_p \prec 0 \;\; \forall\, p \in \mathcal{P}, \;\; \textit{and} \; \forall\, \vec{\delta} \in \mathbb{R}^m \; \textit{with} \; \|\vec{\delta}\|_1 \leq \beta\} \tag{4.40}$$

where $\dot{V}_p = (A_p + \mathcal{M}(\vec{\delta}))^{\intercal} P + P(A_p + \mathcal{M}(\vec{\delta}))$.

Note the difference between the problem generalization for the constriction method versus the expansion method: in the constriction method the perturbation need only invalidate a stability guarantee for *some* component system, whereas for the expansion method the perturbation set must be tolerated by *every* component system. Determining the new maximum of Problem 6 is possible through Theorem 7 where the $\dot{V} \prec 0$ condition of the optimization is appended for every component system, i.e., the optimization in Theorem 7 is further constrained as follows:

$$\begin{aligned}
&\underset{\gamma}{\text{maximize}} && \gamma \\
&\text{subject to} && (A_1 + \mathcal{M}(\gamma,i,j))^{\mathsf{T}} P + P(A_1 + \mathcal{M}(\gamma,i,j)) \prec 0, \quad i = 1,2,...,m, \quad j = 1,2,...,m, \\
&&& (A_1 - \mathcal{M}(\gamma,i,j))^{\mathsf{T}} P + P(A_1 - \mathcal{M}(\gamma,i,j)) \prec 0, \quad i = 1,2,...,m, \quad j = 1,2,...,m, \\
&&& \vdots \\
&&& (A_N + \mathcal{M}(\gamma,i,j))^{\mathsf{T}} P + P(A_N + \mathcal{M}(\gamma,i,j)) \prec 0, \quad i = 1,2,...,m, \quad j = 1,2,...,m, \\
&&& (A_N - \mathcal{M}(\gamma,i,j))^{\mathsf{T}} P + P(A_N - \mathcal{M}(\gamma,i,j)) \prec 0, \quad i = 1,2,...,m, \quad j = 1,2,...,m.
\end{aligned} \tag{4.41}$$

The proof that this additionally-constrained optimization yields the maximum in Problem 6 repeats the same logic as the proof of Theorem 7 and is omitted here for the sake of brevity. The optimization in Theorem 8 is similarly subject to additional constraints in addressing the generalization of Problem 4,

$$\begin{aligned}
&\underset{\gamma}{\text{maximize}} && \gamma \\
&\text{subject to} && (A_1 + \gamma\mathcal{M}(\vec{v})^{\mathsf{T}} P + P(A_1 + \gamma\mathcal{M}(\vec{v})) \prec 0, \quad \forall\, \vec{v} \in \mathcal{V} \\
&&& \vdots \\
&&& (A_N + \gamma\mathcal{M}(\vec{v})^{\mathsf{T}} P + P(A_N + \gamma\mathcal{M}(\vec{v})) \prec 0, \quad \forall\, \vec{v} \in \mathcal{V},
\end{aligned} \tag{4.42}$$

where the same logic in the proof of Theorem 8 applies to the generalization and is similarly omitted for brevity.

4.4 Incorporating System Structure

In this section we evaluate some typical system structures that can be exploited to reduce the space of perturbations under consideration. For the vector perturbation defined in Section 4.2 that generates a perturbation matrix though the map $\mathcal{M}$, defining a perturbation matrix with only a subset of non-zero entries is an inherent capability granted by the definition. For the original matrix perturbation defined in Chapter 2 the statement of $\Delta \in \mathcal{R}^{n\times n}$ needs to be constrained as

$$\Delta : \{X \in \mathcal{R}^{n\times n}, \quad X_{i,j} = 0 \text{ if } (i,j) \in \mathcal{Z}\}, \tag{4.43}$$

where the set $\mathcal{Z}$ is the set of ordered pairs (i,j) that correspond to zero entries. This definition of Δ can be substituted for $\Delta \in \mathcal{R}^{n\times n}$ in Problem 2 and in the results derived from Problem 2 without additional modification.

4.4.1 Controller or System Perturbations

Recall from Chapter 2 the example of how closed loop system dynamics can be constructed from a traditional series-compensator architecture. Consider perturbations to just the plant and compensator dynamics,

$$\dot{x}_a = (A_a + \Delta_{A_a})x_a, \tag{4.44}$$

and

$$\dot{x}_c = (A_c + \Delta_{A_c})x_c, \tag{4.45}$$

where $\dim(\Delta_{A_a}) = \dim(A_a)$ and $\dim(\Delta_{A_c}) = \dim(A_c)$. The closed loop dynamics for the perturbed system are

$$\dot{x} = \begin{bmatrix} A_a + \Delta_{A_a} - B_a D_c C_a & B_a C_c \\ -B_c C_a & A_c + \Delta_{A_c} \end{bmatrix} x, \tag{4.46}$$

from which a perturbation matrix can be extracted in the form $A_{CL} + \Delta$,

$$\dot{x} = \left(\underbrace{\begin{bmatrix} A_a - B_a D_c C_a & B_a C_c \\ -B_c C_a & A_c \end{bmatrix}}_{A_{CL}} + \underbrace{\begin{bmatrix} \Delta_{A_a} & 0 \\ 0 & \Delta_{A_c} \end{bmatrix}}_{\Delta} \right) x. \tag{4.47}$$

Some points regarding notation: first, the zeros in (4.47) are a shorthand to indicate a block of appropriate dimension for which every entry is zero; second, the subscripts of the perturbation variables Δ_{A_a}, Δ_{A_c}, etc, do not refer to indices of the larger matrix Δ. These sub-scripted matrices are used as an aid to demonstrate how parameter variations in components of the closed loop dynamics contribute to an overall perturbation matrix. Referring back to the example architectures in Fig. 2.1, the perturbed closed loop dynamics of (4.47) yield a family of switched linear dynamics in the case of several controllers ($i = 1, 2, ..., N$) designed against one plant (Fig. 2.1a)

$$\dot{x} = \left(\begin{bmatrix} A_a - B_a D_{c_i} C_a & B_a C_{c_i} \\ -B_{c_i} C_a & A_{c_i} \end{bmatrix} + \begin{bmatrix} \Delta_{A_a} & 0 \\ 0 & \Delta_{A_c} \end{bmatrix} \right) x, \tag{4.48}$$

or in the case of several plants each with a corresponding compensator (Fig. 2.1b)

$$\dot{x} = \left(\begin{bmatrix} A_{a_i} - B_{a_i} D_{c_i} C_{a_i} & B_{a_i} C_{c_i} \\ -B_{c_i} C_{a_i} & A_{c_i} \end{bmatrix} + \begin{bmatrix} \Delta_{A_a} & 0 \\ 0 & \Delta_{A_i} \end{bmatrix} \right) x. \tag{4.49}$$

The case of several controllers in positive feedback with a single plant (Fig. 2.1c) yields the same family of dynamics as (4.48) but with a change of sign for the two negated terms. All of these architectures accommodate the same structure of perturbation matrix. The zero elements of the perturbation matrix can be excluded in the computation of tolerable perturbations. In the constriction methods these exclusions result in optimization problems with fewer variables of optimization. In the expansion method the exclusions reduce the dimension of the perturbation vector and thus reduce the number of constraints on the convex optimization problem.

One may wonder why perturbations to compensator dynamics are being considered because of the intuition that there is no uncertainty in the compensators, i.e., we have exact knowledge of the compensator realization. One possible reason to investigate compensator perturbations is the uncertainty associated with implementation. For example, finite word lengths and round-off error encountered when implementing potentially high-order dynamics call into question the sensitivity of compensator representation.

In the event that compensator implementation is not a concern the compensator dynamics are not subject to perturbation. The perturbation matrix in the prior developments can be further simplified to consider only perturbations to the plant dynamics,

$$\Delta = \begin{bmatrix} \Delta_{A_a} & 0 \\ 0 & 0 \end{bmatrix}. \tag{4.50}$$

Next, consider perturbations to the input and output matrices of the plant system only,

$$\begin{aligned} \dot{x}_a &= (A_a + \Delta_{A_a})x_a + (B_a + \Delta_{B_a})u \\ y &= (C_a + \Delta_{C_a})x_a. \end{aligned} \tag{4.51}$$

Again using the series-compensator architecture as an example, the closed loop dynamics for the perturbed plant of (4.51) are

$$\dot{x} = \begin{bmatrix} A_a + \Delta_{A_a} - (B_a + \Delta_{B_a})D_c(C_a + \Delta_{C_a}) & (B_a + \Delta_{B_a})C_c \\ -B_c(C_a + \Delta_{C_a}) & A_c \end{bmatrix} x. \tag{4.52}$$

Again separate these dynamics into nominal closed loop dynamics and a matrix perturbation,

$$\begin{aligned} \dot{x} = \Bigg(&\begin{bmatrix} A_a - B_aD_cC_a & B_aC_c \\ -B_cC_a & A_c \end{bmatrix} + \\ &\begin{bmatrix} \Delta_{A_a} - B_aD_c\Delta_{C_a} - \Delta_{B_a}D_cC_a - \Delta_{B_a}D_c\Delta_{C_a} & \Delta_{B_a}C_c \\ -B_c\Delta_{C_a} & 0 \end{bmatrix} \Bigg) x. \end{aligned} \tag{4.53}$$

The structure of the closed loop dynamics perturbation is not surprising: the only variations that can be ruled out are those associated purely with the compensator dynamics.

4.4.2 Canonical Forms

In the case that a plant model originates in the frequency domain (a transfer function identified from input-output signals for example) there is some freedom in choosing the state space representation of the plant; similarly, controllers designed as transfer functions offer freedom in their realizations. Selecting a cononical realization supplies even more exploitable structure in the consideration of system perturbations. For example, consider again the series-compensator architecture of Fig. 2.1a. Assume the plant and compensators are each realized in observable canonical form (see Appendix A for a description). In this form, the only system-dependant entries in the system A matrix reside in its last column. A perturbation on the plant dynamics can be restricted to

$$\Delta_{A_a} = \begin{bmatrix} 0 & 0 & \cdots & 0 & \delta_1 \\ 0 & 0 & \cdots & 0 & \delta_2 \\ \vdots & \vdots & & \vdots & \vdots \\ 0 & 0 & \cdots & 0 & \delta_m \end{bmatrix}. \tag{4.54}$$

A similar reduction can be made on the compensator dynamics. Consider one of the matrix perturbations from the scenarios discussed in the previous section,

$$\Delta = \begin{bmatrix} \Delta_{A_a} & 0 \\ 0 & \Delta_{A_c} \end{bmatrix}. \tag{4.55}$$

If the state dimension of the plant were n and the state dimension of the controllers were m, a generic matrix perturbation to the closed loop dynamics requires the variation of $(n \cdot m)^2$ parameters. With assumption of canonical realizations the matrix perturbation of (4.55) has only $(n + m)$ free parameters.

4.4.3 Gain Margin

The formulations of the constriction and expansion methods are built on the premise of a matrix perturbation to the closed loop dynamics of a switched system; this section has demonstrated the structure inherent in typical system architectures can be used to significantly reduce the scope of the perturbations necessary in the analysis. Recall, the bound obtained from the prior methods describes a limit on the size of perturbation that can be applied in any direction of the perturbation space. In contrast, the last simplification we discuss here arises from the desire to evaluate a perturbation in one particular direction of the perturbation space. The discussion to follow is not a direct application of the methods developed so far, but it is in the spirit of the expansion method and is thus included in this work as a relevant tangential result.

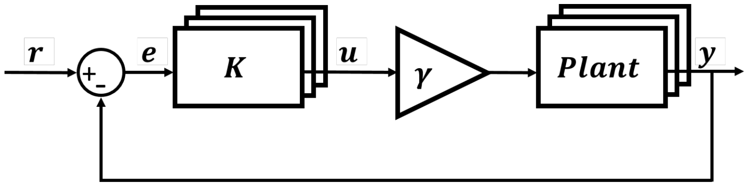

Figure 4.1: Gain margin problem formulation.

Consider the switched linear system architecture depicted in Fig. 4.1. For $\gamma = 1$ the system is identical to the system in Fig. 2.1b. Let us assume the plant models are Single-Input Single-Output (SISO). For any individual closed loop system composed of a plant and its corresponding compensator, the traditional "gain margin" for that LTI system is defined as the maximum γ such that the closed loop dynamics remain exponentially stable (it's of course assumed the nominal system is exponentially stable to begin with). As in the beginning of this work where we sought to extend the stability radius to a measure of robustness for the QCLF, here too we seek to extend the idea of a gain margin to the switched system stability guarantee. First, a definition for the closed loop dynamics of the scaled system:

Definition 11. *For a switched linear system with architecture depicted in Fig. 4.1 the closed* *loop dynamics of a plant compensator pair are given by*

$$A_{CL_p} = \begin{bmatrix} A_{a_p} - \gamma B_{a_p} D_{c_p} C_{a_p} & \gamma B_{a_p} C_{c_p} \\ -B_{c_p} C_{a_p} & A_{c_p} \end{bmatrix}, \quad p \in \mathcal{P} \tag{4.56}$$

For a switched linear system composed of these closed loop dynamics we define the common gain margin as follows.

Definition 12 (Common Gain Margin)**.** *Suppose the closed loop dynamics of Definition 11 are nominally GUES under a predetermined QCLF, $V(x) = x^\intercal P x$. The common gain margin is the maximum $\gamma \in \mathbb{R}$ such that the stability guarantee of $V(x)$ remains valid for the switched linear system, i.e.,*

$$\max\{\gamma : A_{CL_p}^\intercal P + P A_{CL_p} \prec 0 \ \forall \ p \in \mathcal{P}\}. \tag{4.57}$$

Neither the definition of closed loop dynamics or the common gain margin require the plant or plants be SISO in nature; however, if SISO plants are assumed, the common gain margin can be interpreted as the largest traditional gain margin tolerable over all the component plants such that the switched linear system is guaranteed GUES by the original QCLF.

4.5 Examples

As previously mentioned, the multi-controller architecture is a natural approach to many of the challenges in automatic flight control systems. One such challenge that has become increasingly relevant over the last several decades is the flight control design of flexible aircraft. For the large twin-aisle commercial aircraft of today, the automatic flight control systems are tasked not only with the traditional obligation of ensuring safe and stable flight with agreeable handling qualities for pilots, but are now additionally tasked with the regulation of structural behavior where objectives include load alleviation from disturbances including atmospheric turbulence and commanded maneuvers, as well as structural modal suppression for improving ride quality and decreasing airframe fatigue. The control surfaces available for regulation of structural dynamics are the same control surfaces used for flight dynamic control, and the increasing flexibility of newer aircraft structures continues to usher the structural dynamic modes from their traditionally higher frequencies down into the domain of flight dynamic modes. The situation adds up to the need for controllers capable of addressing both traditional and contemporary objectives with one set of actuators to accomplish both.

The Generic Wide Body aircraft model was developed as an openly available aero-structural model for research addressing the synthesis and analysis of flight control laws for flexible aircraft (the development of this model and its suitability for this type of analysis is the subject matter of Chapter 5). While the model is of a complete aircraft (similar to a Boeing 777), the dynamics considered here encompass just a simplified subset of the linear, longitudinal dynamics. The state vector is $x = [u,\ \alpha,\ \theta,\ q,\ \eta_1,\ \dot{\eta}_1,\ \eta_2,\ \dot{\eta}_2]^\intercal$ where u is the linear velocity along the body x-axis, α is the angle of attack, θ is the vehicle's pitch angle, q is the pitch rate, and $\eta_i, \dot{\eta}_i$ are the modal displacement and velocity of the first two symmetric structural modes. Briefly, the modal coordinates arise from approximating structural deformation with a modal basis; see [42] for complete description of the method. The inputs to the system are an elevator deflection angle δ_e and symmetric aileron deflection angle δ_a (meaning both left and right ailerons are deployed in the same direction to the same extent). Sign conventions for the rigid body states and their definitions with respect to the aircraft geometry are depicted in Fig. 4.2 and a depiction of the first mode shape is given in Fig. 4.3.

4.5.1 Individual System

Starting off, we examine the nominal system dynamics of just the rigid body behavior, i.e.

$$\dot{x}(t) = Ax(t), \tag{4.58}$$

where the state is reduced to just $x = [u,\ \alpha,\ \theta,\ q]^\intercal$. These LTI dynamics are exponentially stable with a decay rate bound $\alpha = 0.003$, and a corresponding quadratic Lyapunov function $V(x) = x^\intercal P x$. From these nominal dynamics we compute the real and complex stability radii

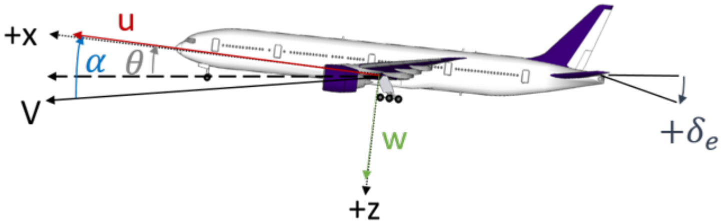

Figure 4.2: Sign conventions of aircraft longitudinal states and control input.

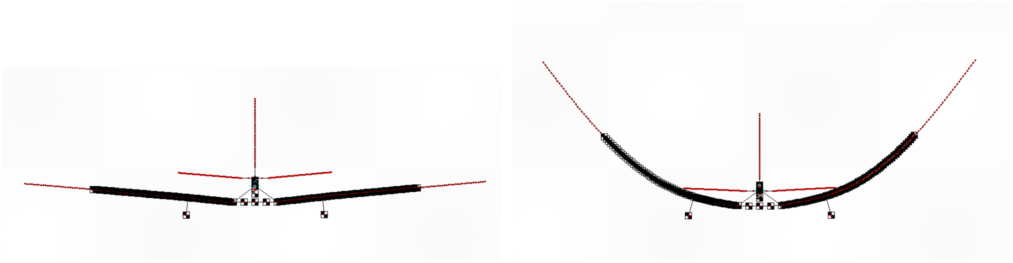

(a) Undeformed shape

(b) First mode shape

Figure 4.3: Front view of structural model demonstrating (highly exaggerated) first mode shape.

(recall these are denoted $r_{\mathbb{R}}$ and $r_{\mathbb{C}}$ respectively). The real stability radius was computed with successive optimizations as detailed in [70]. Also computed for comparison is the bound developed in [26] and reported in [35],

$$\bar{\sigma}(\Delta) \leq \frac{\underline{\lambda}(Q)}{2\overline{\lambda}(P)}, \tag{4.59}$$

where $\underline{\lambda}$ and $\overline{\lambda}$ denote minimum and maximum eigenvalues respectively, and Q is the right hand side of the Lyapunov equation

$$A^{\intercal}P + PA = Q. \tag{4.60}$$

As this bound was first reported in work by G. Hewer and C. Kenny, we will denote the bound as γ_{HK}.

Using the nominal QLF, we approximated the tolerable perturbation bound via constriction (denoted γ_{direct}) with the BMI formulation and the Frobenius norm; for this example the BMIs were solved with YALMIP [71] and MOSEK. Similarly, the relaxed constriction method was solved using the Frobenius norm (denoted $\gamma_{relaxed}$). Regarding the expansion methods, the tolerable perturbation bound was computed via the ℓ_1-ball expansion (denoted γ_{ℓ_1}); the convex optimization problem was formulated and solved with CVX [72, 73]. Table 4.1 summarizes the computed results in decreasing magnitude.

The real stability radius provides an upper limit on any of the perturbation bounds; i.e. no perturbation bound should be larger than the real stability radius. It's worth re-emphasizing that the radii are distances to instability while the perturbation bounds are distances to loss-of-guarantee. That said, the perturbation bounds having similar order of magnitude for this basic set of dynamics is promising for their utility as design metrics. Note that the unit ℓ_1 ball is smaller than the unit sphere associated with the Frobenius norm. Thus, we expect the ℓ_1 perturbation bound to be at least as large or larger than the bounds from the constriction method using the Frobenius norm. Table 4.1 shows that this requirement is satisfied for the relaxed formulation but not for the direct solution, which is an indication that the direct solution did not achieve its global minimum. Finally note that the prior bound, γ_{HK}, is several orders of magnitude smaller than the other bounds obtained.

As a secondary comparison of these results, consider Fig. 4.4. The figure reports an upper bound of matrix perturbation size (using the Frobenius norm) obtained by a random sampling of matrix perturbations. More specifically, a number of random matrix perturbations are sampled with each matrix entry normally distributed in the range $[-1,\ 1]$. The resulting matrix perturbation is scaled to have unit norm and thus provides a single sample of a direction in $\mathbb{R}^{n\times n}$. For a number of such randomly sampled directions, the maximum tolerable scaling of all sampled directions is then computed to provide an estimate of the true bound. The figure demonstrates the expected trend: with a larger number of sample directions the estimated bound decreases. The drawback to this Monte Carlo type of analysis is also demonstrated in the figure: the result approaches the bound $\gamma_{relaxed}$, but is not monotonic (unless samples are re-used) and the computational demand can be much higher. The nominal system is in $\mathbb{R}^{4\times 4}$, but with 7500 samples the sampling method has only loosely converged. With all computation done on the same commodity hardware (3.5 GHz CPU and 16 GB RAM) $\gamma_{relaxed}$ was computed in approximately 0.2 seconds while the sampling method with 7500 samples required approximately 4.3 minutes (the ℓ_1 expansion method took approximately 1.1 seconds).

Table 4.1: Tolerable perturbation sizes for GWB longitudinal flight dynamics.

Method	Value
$r_{\mathbb{R}}$	9.65×10^{-4}
γ_{direct}	4.42×10^{-4}
$r_{\mathbb{C}}$	6.52×10^{-5}
γ_{ℓ_1}	1.70×10^{-5}
$\gamma_{relaxed}$	1.02×10^{-5}
γ_{HK}	3.95×10^{-10}

Whereas all the bounds reported in Table 4.1 addressed full matrix perturbations, the next part of this example demonstrates the utility of interpretation from reduced parameter considerations. First, note that the linear longitudinal dynamics are composed from dimensional stability derivatives as

$$\begin{bmatrix} \dot{u} \\ \dot{\alpha} \\ \dot{\theta} \\ \dot{q} \end{bmatrix} = \begin{bmatrix} X_u & X_\alpha & -g & 0 \\ \frac{Z_u}{V-Z_{\dot{\alpha}}} & \frac{Z_\alpha}{V-Z_{\dot{\alpha}}} & 0 & \frac{V+Z_q}{V-Z_{\dot{\alpha}}} \\ 0 & 0 & 0 & 1 \\ M_u + M_{\dot{\alpha}}\frac{Z_u}{V-Z_{\dot{\alpha}}} & M_\alpha + M_{\dot{\alpha}}\frac{Z_\alpha}{V-Z_{\dot{\alpha}}} & 0 & M_q + M_{\dot{\alpha}}\frac{Z_q}{V-Z_{\dot{\alpha}}} \end{bmatrix} \begin{bmatrix} u \\ \alpha \\ \theta \\ q \end{bmatrix}. \tag{4.61}$$

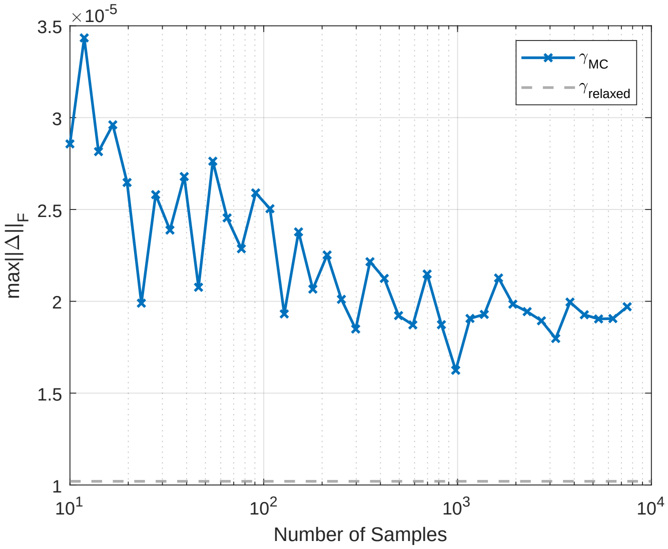

Figure 4.4: Perturbation bound from random sampling.

A flight dynamics textbook, such as [74], will have a summary of the formulation of linear longitudinal flight dynamics and for definitions of the dimensional stability derivatives. The ℓ_1-expansion method is now used to determine the total mount of perturbation tolerable to the dynamics of forward speed, u. Assuming gravity is well known, the uncertainty in the dynamics of u depends only on the X_u and X_α dimensional stability derivatives. We apply the ℓ_1-expansion method where only perturbations to this first and second entry of the matrix are considered. The result is $\gamma_{\ell_1} = 0.0017$. The nominal values of these derivatives are $X_u = -0.0039$ and $X_\alpha = 6.1518$. So the result yields the intuition that the stability guarantee is far more sensitive to variation of X_α; i.e. a 42% variation in X_u is required to invalidate the guarantee compared to a 0.03% necessary change in X_α.

As another case, consider the ℓ_∞-expansion method used to determine the maximal variation of $M_{\dot{\alpha}}$. Using the reduced parameter formulation, only the nonzero entries of the last row of the system matrix are considered for variation. The result is $\gamma_{\ell_\infty} = 2.634 \times 10^-5$. Using this bound, and assuming the other parameters are fixed, we can determine the corresponding tolerable variation in $M_{\dot{\alpha}}$. As a demonstration, take the first entry of the last row and consider the perturbation to result from a change in $M_{\dot{\alpha}}$,

$$M_u + M_{\dot{\alpha}}\frac{Z_u}{V - Z_{\dot{\alpha}}} + \gamma_{\ell_\infty} = M_u + (M_{\dot{\alpha}} + \delta_{M_{\dot{\alpha}}})\frac{Z_u}{V - Z_{\dot{\alpha}}}. \tag{4.62}$$

The expression can be solved for the admissible variation, $\delta_{M_{\dot{\alpha}}}$. The tolerable variation is computed this way for each of the three nonzero terms in the last row of the system dynamics matrix. The smallest of these values is then an amount of variation that can be tolerated by the system; the result for this example is $\delta_{M_{\dot{\alpha}}} = 0.0817$ which is approximately 59% of $M_{\dot{\alpha}}$. Note that the ℓ_∞-expansion method was necessary for this evaluation because the parameter variation impacts multiple terms and must therefore be tolerated simultaneously by each dependent term (as compared to the ℓ_1 class of results where the perturbation can only impact a single entry at its fullest extent).

4.5.2 Multi-objective Control

Our multi-controller analysis involves the full state vector including rigid body and structural dynamic states. A multi-controller design is utilized to address the following difference in control objectives. The first objective regards desirable longitudinal handling qualities; it was found in [75] that consistently positive pilot ratings were reported if the closed loop response from commanded pitch rate to measured pitch rate matched the following transfer function

$$\frac{q}{q_{cmd}} = 18.8\frac{(s + 0.576)(s + 0.78)}{(s + 0.59)(s^2 + 1.673s + 1.416)(s + 10)}. \tag{4.63}$$

The second objective is the reduction of wing-root bending moment incurred from aerodynamic loading. Part 25 of the Federal Aviation Requirements stipulates a procedure for determining the worst-case gust that an airframe must be designed to sustain. The profile of the gust is expressed mathematically as

$$U(x) = \frac{1}{2}U_0\left(1 - \cos\frac{2\pi x}{2H}\right), \tag{4.64}$$

where U is the gust velocity, U_0 is a nominal amplitude, H prescribes the gust length, and x is the independent variable over which the profile is being defined (see [76] for details). A gust load alleviation controller should nominally be able to address the worst case gust, and so alleviating load from this profile (or a disturbance of similar magnitude and frequency content) forms the design criteria of a gust load alleviation controller. Using the generalized system architecture of Fig. 2.1c and the H_∞ synthesis method, two controllers were designed where the model matching and gust load alleviation objectives were incorporated in both designs, but with differing weighting functions to emphasize one objective over the other. Figure 4.5 shows a comparison of the open loop and closed loop load in response to a discrete gust ("HQ" denotes the controller emphasizing handling qualities, "WRB" denotes the controller emphasizing wing-root bending). Note, the structural damping of the GWB model is an adjustable parameter which in this case was left intentionally low so as to provide an exaggerated structural response (the same nominal model was used for both controllers).

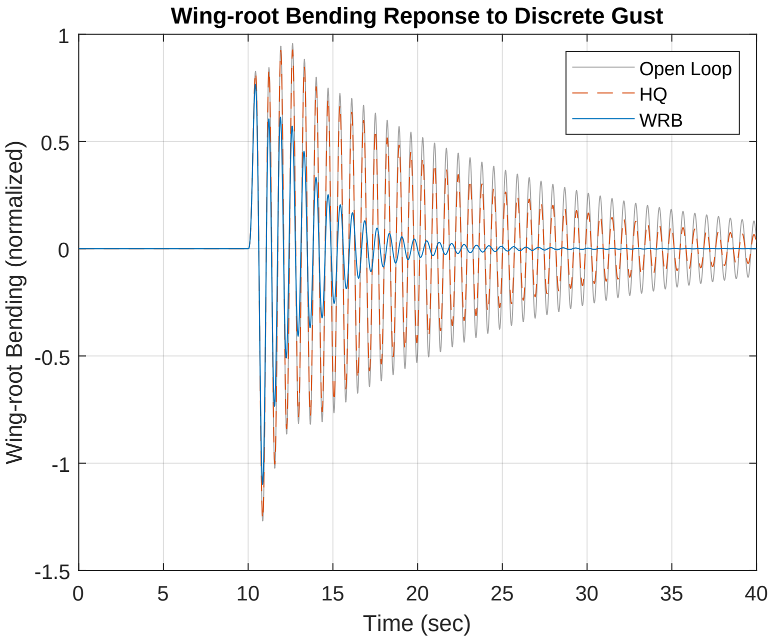

Figure 4.5: Comparison of controlled behavior in response to discrete gust.

Using the expansion method with a full matrix perturbation and CVX again to solve, a value of $\gamma_{\ell_1} = 1.103 \times 10^{-}7$ was computed. The constriction method, using the relaxed method and the max-norm, was solved using MATLAB's fmincon which computed a value $\gamma_{relaxed} = 0.974$. Recall that the constriction methods necessitate a global minimum be determined for a non-convex problem. As the max-norm over-bounds the ℓ_1 norm, the result from the constriction method should be smaller than the expansion method because full matrix perturbations were considered. Given that the constriction result does not satisfy that criteria, it's apparent the global minimum was not found. This example demonstrates the drawback of the constriction methods.

Chapter 5

GENERIC WIDE BODY MODEL AND SIMULATION ENVIRONMENT

One challenging aspect of designing flight controllers for modern flexible aircraft comes from the decreasing distinction between rigid body flight-dynamic modes and structural vibration modes. Long standing design practice has been to design flight control systems with intentional bandwidth limitations and filters to prevent interaction of the flight controllers with structural dynamics. Rigid body models used in flight control design often use aerodynamic derivatives that are corrected to account for the static deformation of the structure at a given condition, but structural dynamics are otherwise neglected [77]. Aero-structural modeling has typically entered the design cycle as a critical sizing condition on lifting surfaces that are subject to aeroelastic divergence or flutter [78]. As a result, most aero-structural models available do not bother with full aircraft structural definitions. Also, as modern aircraft design processes progressively transition to holistic approaches, there is increasing interest in exploiting the ability of flight control systems to alleviate structural/aerodynamic design constraints [32]. Studies in flight control involving aero-structural models need to be able to assess the impact of changes in configuration/structure on the control system and/or the possibilities for control systems to permit configuration or structural changes. Thus, there exists a need for a complete aero-structural model in an un-reduced and modifiable form. The Generic Wide Body (GWB) aircraft model presented in this work is meant to fulfill that need.

The contribution here is an aero-structural model fit for evaluation of flight control investigations involving structural interactions with rigid body flight behaviors, e.g. structural mode control, maneuver load alleviation, gust load alleviation, etc. While we discuss the development of flight dynamics models, the main model is provided in an unreduced form ([63]) so that future studies can assess the impact of true model changes on control law performance or design. In accordance with that motivation of accessibility, the model has been developed and provided in terms of industry-standard NASTRAN modeling elements. The particular modeling elements implemented imply the use of standard model analysis techniques, i.e. finite element structural analysis and doublet lattice aerodynamic analysis; analysis techniques having assumptions consistent with the flight dynamics assumptions imparted on the structural mode and load alleviation controllers mentioned previously. The provided model is thus capable of supporting many future investigations of flight control systems on flexible commercial airframes.

5.1 Modeling Methods

If the intent is to use the completed aero-structural model to develop and simulate flexible aircraft dynamics, then the desired complexity of the dynamics largely dictate complexity requirements on the model. The primary goal here with the aero-structural vehicle dynamics is to evaluate control law interaction and design when structural modes cannot be assumed out-of-bandwidth. This goal does not require the consideration of large structural displacements, large aerodynamic incidence angles, or large changes in mass or inertia. These simplifications lend application of the modeling techniques to be described in the following.

5.1.1 Structural Modeling

The standard tool for evaluating structural dynamics of an airframe is a Finite Element Analysis (FEA). A useful summary of the finite element method and its application to aircraft structures is available in [44]. To briefly summarize: a complete structure is approximated by an interconnection of numerous “finite elements”. Mass and stiffness properties of the individual elements are used with the interconnection relationships to determine global mass and stiffness properties for the total structure. This computational approach allows the displacement of a continuously deformable structure to be approximated by a finite number of degrees of freedom.

It is well understood that the accuracy of FEA depends on the ability of the underlying finite element representations to faithfully capture the responses of their physical counterparts [79]. Proper element selection is the primary difficulty in generating any Finite Element Model (FEM). Fortunately, maximum model fidelity is not always necessary. In the same way that a wing box structure can be approximated by an "equivalent beam", simple beam elements can be tuned to exhibit the same large scale behavior as higher fidelity representations the same structural segment. Thus, the structural engineer concerned with stress concentrations or buckling of a skin on a wing box will work with a high fidelity FEM of the structural segment in question, while a flight dynamics engineer concerned with structural vibration noise in an inertial measurement unit will require a full vehicle model without the need for a high degree of local accuracy in stress or strain evaluation.

A "stick-model" is a common term used to describe a FEM composed of discrete masses connected by beam elements. Due to the nature of conventional aircraft structures, i.e. structures subject to small displacements and structures having components that are slender in form, a stick model is often preferred for the expression of structural dynamics because its dimensionality can be orders of magnitude less than a full fidelity model. And again, the structural properties of the simple elements can be tuned to match the bulk behavior of higher fidelity models or experimental data near desired conditions.

5.1.2 Aerodynamic Modeling

Just as in structural modeling, our selection of aerodynamic modeling techniques depends on the required level of fidelity. The basic concerns in flight control of a flexible commercial aircraft occur in subsonic flight at benign angles of attack. Also, the dynamic behaviors are not significantly impacted by imprecision in aerodynamic drag estimates. These circumstances allow the use of potential flow aerodynamic theory in evaluating aerodynamic properties of the vehicle. An overview of potential flow methods and their application to the computation of aircraft aerodynamic characteristics can be found in [80]. Basically, the surfaces of the aircraft are approximated as lifting surfaces in a linear potential flow. A discrete set of points on each surface are used to enforce flow conditions by varying source/sink and vortex strengths to solve for a consistent flow field. Pressures experienced by the lifting surfaces are computed from the flow solution to provide aerodynamic forces and moments.

Potential flow methods allow decent approximation of aerodynamic forces on large and complicated airframes. However, the neglect of viscous effects requires drag estimation to be computed/approximated by some other means. Also, results are only valid for small angles of incidence to the flow as flow separation is not captured. Assuming these limitations are acceptable, potential flow methods are analogous to simple elements from FEA in that the potential flow results can be tuned to match high fidelity fluid simulations or wind tunnel data. The potential flow theory of choice in NASTRAN is the Doublet Lattice Method (DLM). Details about the method can be found in [81]. The doublet lattice method is an extension of the vortex lattice method that allows for unsteady (harmonically gusting) flows.

5.1.3 Aero-structural Coupling

Fluid-structure interaction, or relating structural displacement to changes in the aerodynamic forces and visa versa, is one of the large challenges in modeling aeroelastic structures. More complicated structural deformations require more complicated relationships to describe aerodynamic geometry changes. However, because of the small displacement assumptions made in the stick model approximation and the simplistic aerodynamic geometry of flat aerodynamic panels, the relationship between structural displacements and aerodynamic geometry can be defined by a simple linear spline. Such a spline is used to map translational and rotational displacements of a structural segment to changes in the flow field of an associated aerodynamic panel; the spline-based relationship is invertible so that forces generated on an aerodynamic panel can be mapped to applied forces and torques on associated points on the structural. Using these splines, the aerodynamic and structural models are combined in a numerical analysis to characterize steady or unsteady aeroelastic behavior. Such analysis is the final step in processing model data to provide input for a flight dynamic model.

5.1.4 Development Process

Model development of the GWB began with the collection of publicly available data for aircraft in the reference segment of commercial aviation, i.e., Airbus A350-1000 and Boeing 777-300ER. A vast majority of the geometry, weight, and performance information were collected from *Jane's All the World's Aircraft* [82]. Those data were supplemented by values published by Boeing [83] in reports generally used for airport planning.

The next step in the development process was to generate a structural model. For this task the NeoCASS [84] (Next Generation Conceptual Aero Structural Sizing) suite of Matlab modules was employed. NeoCASS starts with a parameterized representation of the aircraft geometry, payload requirements, and performance requirements. From there a stick model geometry is created. Structural and nonstructural mass is allocated to beam elements and discrete mass elements respectively. Then, beam properties (EI, GJ) are tuned based on assumed material properties and some standard applied load cases from civil aviation requirements. The procedure of mass allocation and beam property tuning is iterated upon to arrive at an optimized stick model. This stick model is expressed in terms of NASTRAN model elements.

Next, an aerodynamic model had to be created in a manner compatible with the geometry constructed as part of the NeoCASS model construction. The aerodynamic elements used were those in NASTRAN that are compatible with the doublet lattice potential flow method described in the previous section. Spline elements were then defined to relate displacements of structural elements to changes in aerodynamic behavior and vice versa.

Finally, control surface elements were defined. Control surface geometry is where the model most diverges from the reference aircraft. As will be detailed later, the GWB has been outfitted with many more wing-board control surfaces than are currently employed on the reference aircraft. This point was the end of the raw model development. Fight dynamics models were then developed using analysis results from a static aeroelastic trim solution run by NASTRAN. While the interest of this work goes beyond a single flight dynamic model, this final step will be elaborated upon in Section 5.3 as a suggested use case of the raw model data.

5.2 Description

5.2.1 General Aircraft Data

As previously noted, the GWB is a twin engine, wide body, commercial jet transport representative of airframes in the Airbus A350-1000 / Boeing 777-300ER market segment. Figure 5.1 depicts the bulk dimensions and layout of the 340 passenger aircraft. The vehicle is presumed capable of cruise at Mach 0.8 with a service ceiling of 13,000 m.

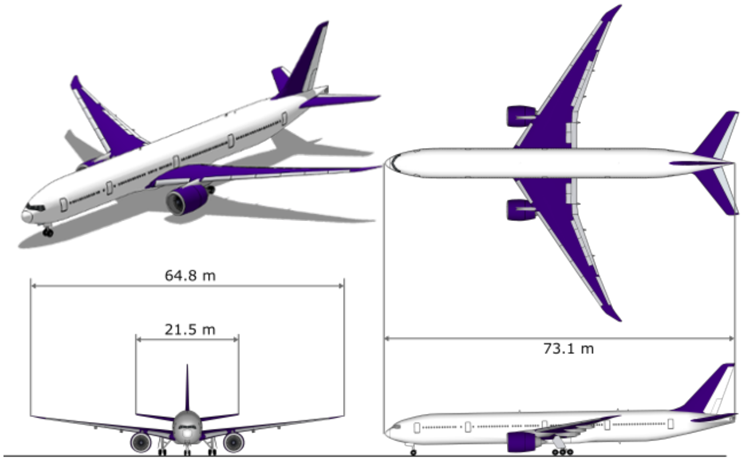

Figure 5.1: Overall dimensions of the Generic Wide Body aircraft based on reference aircraft [82].

5.2.2 Structural Model

The structural model is composed using the following types of NASTRAN modeling elements (see [85] for complete element descriptions and format specifications):

GRID Defines the location of a geometric grid point, the directions of its displacement, and its permanent single-point constraints.

CBAR Defines a simple beam element.

PBAR Defines the properties of a simple beam element.

RBE2 Defines a rigid body with independent degrees-of-freedom that are specified at a single grid point and with dependent degrees-of-freedom that are specified at an arbitrary number of grid points.

MAT1 Defines the material properties for linear isotropic materials.

CONM2 Defines a concentrated mass at a grid point.

Briefly, the elements are related in the following way: GRID elements define geometry based on their location and they yield the active degrees of freedom to be analyzed in structural dynamics. CBAR and RBE2 elements are bar elements defined with their ends attached to grid points. The CBAR elements have their cross sectional properties defined in PBAR elements. Also, the bar elements must identify a material to be composed of, which is defined in a MAT1 element. Structural mass is included in the bar properties, while non-structural mass is accumulated into lumped masses defined with CONM2 elements.

With respect to the GWB structural model, the elements just described are implemented to construct a stick model as depicted in Figure 5.2. The figure demonstrates the geometry based on grid points and that those grid points are connected with beam elements. Also depicted are the discrete masses that are used to represent the fuel, payload, and other non-structural mass. The model has 404 grid points all of which are afforded six degrees of freedom, i.e., the total deformation of the structure is described by the three translational and three rotational displacements of each grid point. Thus, the total GWB structural displacement is comprised of 2,424 degrees of freedom.

The grid points of the GWB model are located relative to the “basic” coordinate frame. In the images of Fig. 5.2 the origin of the basic coordinate frame is indicated with a small circle near the nose of the aircraft. The basic coordinate frame is right handed; the x-axis runs parallel the fuselage with positive x pointing aft; the y-axis is positive in the direction of the starboard wing; and the z-axis is positive in the direction of the vertical tail. The assumed unit system for the GWB is Meter-Kilogram-Seconds (MKS). The grid point locations are defined in meters accordingly.

The beam elements of the model encapsulate not only structural mass between the grid points, but also bending and torsional stiffness. Those stiffness are not specified directly, but rather by specifying the beam material property (Aluminum used throughout) and the beam cross sectional inertias. These beam properties are those which would be tuned in order to achieve equivalence between a stick model and some higher fidelity representation. The observed structural characteristics of the GWB are essentially controlled by these beam properties.

Table 5.1 provides a weights build-up for the structural model. At full weight, the aircraft's center of gravity is at (35.15,0,-1.50) with all values specified in meters and with respect to the previously described coordinate system. The inertia tensor is expressed in terms of the body coordinate system, *i.e.* origin at the center of gravity, positive x out the nose of the aircraft, positive y out the starboard wing, and positive z away from the vertical tail. In that frame, the aircraft's inertia tensor (with units of $kg \cdot m^2$) is

$$I = \begin{bmatrix} 2.812968 \times 10^7 & 0 & 2.315020 \times 10^6 \\ 0 & 4.375067 \times 10^7 & 0 \\ 2.315020 \times 10^6 & 0 & 7.003581 \times 10^7 \end{bmatrix}.$$

5.2.3 Aerodynamic Model

The aerodynamic components of the model are defined using the following types of bulk data entries (again, see [85] for more detail about NASTRAN modeling elements):

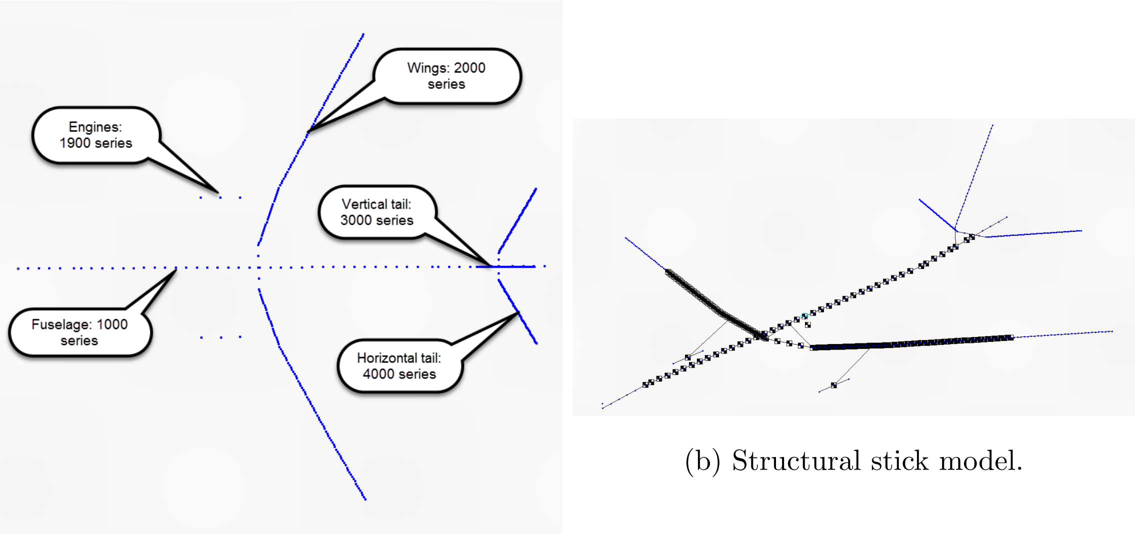

(b) Structural stick model.

(a) Grid numbering scheme.

Figure 5.2: The model is composed of grid points (blue dots) connected by beam elements (black lines). The structural mass is distributed in the beam elements while non structural masses like fuel and payload are idealized as point masses located at grid points (black checkered symbols).

CAERO1 Defines an aerodynamic macro element (panel) in terms of two leading edge locations and side chords.

CAERO2 Defines aerodynamic slender body and interference elements for doublet lattice aerodynamics.

PAERO1 Defines associated bodies for the panels in the doublet lattice method.

PAERO2 Defines the cross-sectional properties of aerodynamic bodies.

AESTAT Specifies rigid body motions to be used as trim variables in static aeroelastic analysis.

Table 5.1: Weights composition of the GWB structural model.

Landing gear	12,519 kg
Passengers	33,660 kg
Baggage	3,084 kg
Center wing tank	32,981 kg
Wing tanks (total)	120,202 kg
Engines (total)	59,975 kg
Structure	98,407 kg
Total	360,828 kg

AELIST Defines a list of aerodynamic elements to undergo the motion prescribed with the AESURF Bulk Data entry for static aeroelastic analysis.

AEFACT Defines real numbers for aeroelastic analysis.

DMI Defines matrix data blocks.

AESURF Specifies an aerodynamic control surface as a member of the set of aerodynamic extra points.

SPLINE2 Defines a beam spline for interpolating motion and/or forces for aeroelastic problems on aerodynamic geometries defined by regular arrays of aerodynamic points.

SET1 Defines a list of structural grid points or element identification numbers.

CORD2R Defines a rectangular coordinate system using the coordinates of three points.

Briefly, these elements are related in the following way: CAERO1 elements are used to define the aerodynamic panels of the aircraft (wings, horizontal tail, vertical tail). A panel element is sub-divided into smaller panels. The number and spacing of the divisions can be modified, and are defined in part with corresponding AEFACT cards. On some CAERO1 elements, control surfaces are defined as a subset of the sub-divided panels using an AESURF card. The definition of a control surface requires an AELIST card to identify which aero-panels comprise the surface, as well as a CORD2R card to define the hinge line of the actuator. The deflection of different actuators can be locked together using AELINK cards. Next, an aero-panel must be “attached” to the structure in some manner. This task is accomplished with SPLINE2 elements. Using a spline element requires a SET1 card to identify the structural grid points that should be included in the interpolation set for the spline. The panels of the CAERO1 cards must be associated with a PAERO1 card to identify slender bodies that should be included in any interference computations. The slender bodies (fuselage and engines) are defined with CAERO2 cards which require PAERO2 cards to define the shape of the body. Finally the DMI card is used in order to modify the downwash of the aerodynamic panels in order to reflect the incidence angles of the wing and horizontal tail (note: the purpose of the DMI card is much more general that just described. *i.e.* the DMI card is not inherently categorized as an aerodynamic property card).

The full aerodynamic model is depicted in Fig. 5.3a. Aside from the main wing, all of the large aircraft elements are modeled with single aerodynamic elements, i.e. right/left horizontal stabilizer, vertical tail, fuselage, and engines. As shown in Fig. 5.3b, the main wing is broken into several aerodynamic panels to better approximate the reference geometry. Also, the aerodynamic panels are defined with their chordwise edges parallel to the streamwise direction. As a result, no incidence or wing twist can be defined by the geometry of the panels alone. Instead, DMI cards must be used to alter the nominal downwash experienced by a panel. All panels of the main wing are thus modified to have four degrees of positive installation incidence while the panels of the horizontal stabilizer are given four degrees of negative installation incidence. For an aircraft of this size the incidence of the horizontal stabilizer is generally made variable though a low-bandwidth screw-style actuator. The fixed value of incidence modeled here is easily changed to accommodate the generation of flight dynamic models that trim well in desired regions of a flight envelope. These values of incidence and other key aerodynamic geometry values are listed in Table 5.2.

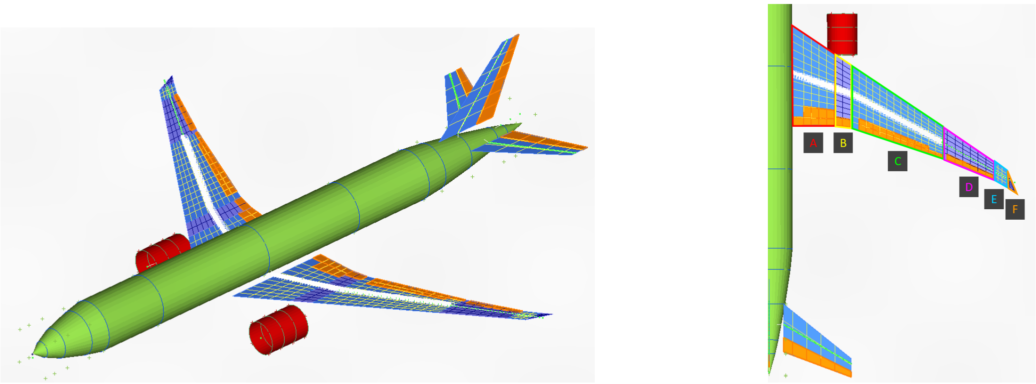

(a) Aerodynamic model.

(b) Wing panel sectioning.

Figure 5.3: Full GWB aerodynamic model and wing panel sectioning. The panel labels in the right figure reflect the naming scheme used in the model listing in the appendix. The color coding of labels in the right figure applies only to the bordering of each wing panel to aid identification of the individual panels.

The clearest difference between the reference aircraft and the GWB aerodynamic model is in the wing-board actuator definitions. As depicted in Fig. 5.4, the GWB actuator set builds on that employed in the reference model. Starting from the starboard wingtip and working inward we find that the single outboard aileron surface has been split into three distinct surfaces comprised of the same area. Next, the five outboard spoiler elements are implemented without change. However, the section of trailing edge aft of the outboard spoilers that is nominally a high lift device has been modeled as an array of "flap" elements. The inboard aileron (only other trailing edge device on the 777) is modeled similarly on the GWB, as are the two elements of the inboard spoiler. Again, looking to the trailing edge aft of the inboard spoiler elements we see that the GWB has been supplied a set of three inboard flap array elements.

Table 5.2: Key geometric properties of the aerodynamic model.

Component	Property	Value
Wing	Span	64.8 m^2
	Area	482.6 m
	Mean aerodynamic chord	8.23 m
	Leading edge sweep	34.5 deg
	Installation incidence	+4 deg
Horizontal tail	Span	21.5 m
	Area	101.3 m^2
	Mean aerodynamic chord	5.06 m
	Leading edge sweep	37 deg
	Installation incidence	-4 deg
Vertical tail	Span	9.5 m
	Area	53.2 m^2
	Mean aerodynamic chord	6.04 m
	Leading edge sweep	45 deg

5.3 Analysis

5.3.1 Modal Analysis

Aside from the weight and balance information already reported, the key properties of the structural model are the results of an eigenmode analysis for the un-damped structure. This analysis supplies the information required to assemble the modal representation of linear structural dynamics as described in [42]. Briefly, recall that the connections, properties, and degrees of freedom in the finite element model are used to construct a global expression of

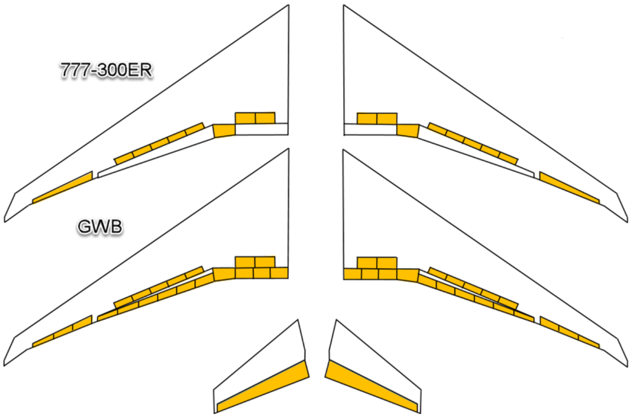

Figure 5.4: Comparison of longitudinal actuator implementation between the Boeing 777 and the Generic Wide Body.

undamped, unforced dynamics. Recall that the total structure is composed of grid points connected by elements, and each grid point of the structure has six degrees of freedom. Consider concatenating the degrees of freedom for all of the grid points into a single vector and calling that vector the generalized displacement vector, $\vec{u}$. Through the formulation of the finite elements of the structure, linear dynamics can be composed for the total structure in terms of the generalized displacement vector, a global mass matrix $\mathbf{M}$, and a global stiffness matrix $\mathbf{K}$. These dynamics are expressed as

$$\mathbf{M}\ddot{\vec{u}} + \mathbf{K}\vec{u} = 0. \tag{5.1}$$

The eigenvalue problem comes from assuming displacements to be in the form of harmonic motion, for example

$$\vec{u} = \vec{\phi} \sin \omega t, \tag{5.2}$$

where $\vec{\phi}$ is some unknown constant vector with the same dimension as $\vec{u}$. Substituting this motion into the dynamics of (5.1) yields the following,

$$-\omega^2 \mathbf{M}\vec{\phi} \sin \omega t + \mathbf{K}\vec{\phi} \sin \omega t = 0. \tag{5.3}$$

This last expression is a generalized eigenvalue problem,

$$(\mathbf{K} - \mathbf{M}\omega^2)\vec{\phi} = 0. \tag{5.4}$$

Given $\mathbf{M}$ is of dimension $n \times n$, the solution to the generalized eigenvalue problem in (5.4) yields n eigenvectors ϕ and n corresponding values of ω^2. The usual notation for an eigenvalue is $\lambda = \omega^2$. Because the model is unconstrained in six degrees of freedom (rigid body translation and rotation) the first six eigenvalues are expected to be zero. Table 5.3 enumerates eigenvalues of the first 22 non-rigid body modes.

Table 5.3: Eigenvalues of the first several GWB modeshapes.

Symmetric		Antisymmetric	
Mode	Freq (Hz)	Mode	Freq (Hz)
1	1.22	2	1.66
3	3.11	4	3.23
5	3.38	6	3.40
7	3.60	8	4.41
9	4.46	10	5.55
12	6.82	11	6.69
14	7.41	13	7.26
16	8.84	15	8.47
18	13.15	17	9.50
20	13.78	19	13.15
22	14.55	21	14.34

5.3.2 Static Aeroelastic Analysis

The static aeroelastic analysis like the one available in NASTRAN can provide the remaining information necessary to build a flight dynamic model for a flexible vehicle. The following is a summary of how the structural and aerodynamic model data are processed as a prerequisite for an aeroelastic trim routine. The "set" terminology used below mirrors that used in the NASTRAN documentation [86].

Using the doublet lattice method, the aerodynamic properties of the vehicle are computed assuming a rigid body. More specifically, the panels of the aerodynamic model are defined with four points; one at each panel corner. These points are referred to as the k-set. Within each panel there is a single point, called a control point. The downwash of the flow field is computed at each control point. These control points are collectively referred to as the j-set. As a panel is deflected with respect to the flow, the points of the k-set are displaced. The implementation of the doublet lattice method in NASTRAN computes a substantial derivative matrix, D_{jk}, that describes how a displacement of panel points effects the downwash for that panel. Now, because the technique relies on potential flow theory, a change in downwash at one point in the flow field impacts the complete flow field, i.e. the downwash at every other control point. An influence matrix, A_{jj}, encodes the influence that a change in downwash at one point in the j-set has on every other point in the j-set. The downwash values at each control point can be used to determine pressure differentials across panels. And from those differentials, aerodynamic forces and moments can be computed. The relationship between downwash intensity at control points and forces exerted on panels is aggregated into an integration matrix, S_{kj}.

The aero-structural coupling technique requires some method of relating deformation of the structural grid point to deformation of the aerodynamic panel points. For NASTRAN, that need is accomplished through spline functions. These splines are encoded into an interpolation matrix G_{ka} which transforms a displacement of the structural grid points (the a-set) to a displacement of the aerodynamic panel points (the k-set). By chaining the prior relationships together, one can obtain a matrix that describes the forces experienced by structural grid points due to the aerodynamic forces and moments generated by displacement of the structural grid points. This matrix, Q_{aa} is defined as

$$Q_{aa} = G_{ka}^{\intercal} S_{kj} A_{jj}^{-1} D_{jk} G_{ka}. \tag{5.5}$$

Similar to the substantial derivative matrix D_{jk} that relates displacements of aerodynamic panel points (k-set) to downwash magnitudes experienced at aerodynamic control points (j-set), there is also a substantial derivative matrix D_{jx} that relates displacements of "aerodynamic extra points" (x-set) to downwash magnitudes experienced at aerodynamic control points (j-set). The set of aerodynamic extra points includes rigid body states like angle of attack, α, and side-slip angle, β, as well as deflections of control surfaces. Again by chaining together the appropriate relationships, we obtain a matrix that describes the forces experienced by structural grid points due to displacements of rigid body states and control surface deflections. This matrix, Q_{ax}, is defined as

$$Q_{ax} = G_{ka}^{\intercal} S_{kj} A_{jj}^{-1} D_{jx}. \tag{5.6}$$

Now we use this information in assembling expressions of flight dynamics. First, recall that the global displacement vector of the structure, $\vec{u}$, belongs to the a-set. Aerodynamic force and moment coefficients can be determined by appropriate summation of the forces and torques obtained from a unit deflection of specific aerodynamic extra points. For example, a unit deflection of the angle of attack, α, extra point would generate a global force vector on the structure, $\vec{F}$, computed as

$$\vec{F} = Q_{a\alpha} \alpha. \tag{5.7}$$

The corresponding lift force is found by summing the components of $\vec{F}$ oriented in the Z direction (recall that the structure coordinate system was defined with $+z$ oriented out the top of the aircraft). This summation of specific elements in $\vec{F}$ can be expressed as a dot product between the force vector and a binary "summation" vector, $\vec{s}$. For example, to add the first and fourth entries of a five element force vector, the appropriate summation vector would be

$$\vec{s} = [1\ 0\ 0\ 1\ 0], \tag{5.8}$$

Applying this process to the results of the static aeroelastic analysis for the GWB at a flight condition of Mach 0.5 at 1000 m altitude yields the aerodynamic force coefficients listed in Table 5.4. Note, these values result from the trimmed deformation of the airframe; many textbooks would refer to these as "aeroelastically adjusted" stability derivatives.

Table 5.4: Aerodynamic stability derivatives of the GWB at Mach 0.5 and 1000 m altitude.

	zero	α	β	p	q	r	δ_{elev}	δ_{rud}	δ_{ail}
C_L	0.2041	4.6618	-	-	9.3708	-	0.366	-	-
C_S	-	-	-0.2969	-0.1664	-	0.2910	-	-0.1651	0.0063
C_M	0.1834	-1.8359	-	-	-22.1450	-	-1.3338	-	-
C_N	-	-	0.1280	0.0251	-	-0.1356	-	0.0817	-
C_ℓ	-	-	-0.1017	-0.4188	-	0.0502	-	-0.0198	0.0307

As an example of how the GWB model can be used to inform the assembly of a flexible aircraft flight dynamics model we will consider the approach detailed in [42]. In that approach, the linear longitudinal dynamics are derived in terms of rigid body states: forward body velocity, u, angel of attack α, pitch angle, θ, and pitch rate, q, as well as a number of modal coordinates, η_i. The modal coordinates reflect a reduced order approximation of structural displacement, i.e. the generalized displacement vector is approximated using a subset of the modeshapes as

$$\vec{u} \approx \tilde{\mathbf{\Phi}}\vec{\eta}. \tag{5.9}$$

If, for example, the flight dynamics model were to approximate structural displacement with only two modes, the linear longitudinal dynamics would have the usual form

$$\dot{\vec{x}} = A\vec{x} + B\vec{u}, \tag{5.10}$$

where the state vector would be composed as

$$\vec{x}^{\intercal} = [u \ \alpha \ \theta \ q \ \eta_1 \ \dot{\eta}_1 \ \eta_2 \ \dot{\eta}_2]. \tag{5.11}$$

The control vector would be composed of control surface deflections e.g., elevator deflection,

$$u = \delta_e. \tag{5.12}$$

For this kind of dynamics construction the A matrix in (5.10) would be partitioned as depicted in Fig. 5.5. With respect to this partitioning the A_r partition can be informed with aerodynamic stability derivatives. The partition which captures the impact of structural displacements on rigid body dynamics is A_{re}. This partition requires the computations of lift and moment derivatives based on modal displacements, e.g. C_{L_η}. This example derivative can be computed from the static aeroelastic analysis by summing the vertical force generated by a unit displacement of the first mode. The unit displacement of the first mode is just the first mode shape, $\vec{\phi}_1$. Using (5.5), we obtain the global force vector applied to the structure caused by the deflection of the first mode. Finally, an appropriate summation vector can be used to accumulate the vertical forces from the global force vector to yield a dimensional force derivative

$$C_{L_{\eta_1}} = \vec{s} Q_{aa} \vec{\phi}_1. \tag{5.13}$$

The other derivatives to be computed for A_{re} can be computed similarly. The next partition, A_{er}, characterizes the generalized force, Q, imparted on the structural modes due to changes in rigid body states. An example derivative used in this partition would be the generalized force imparted on the first mode due to a change in angle of attack, $C_{Q_{1_\alpha}}$. This derivative can be computed using the aerodynamic extra point force relationship in (5.6) and projecting the global force vector on the mode shape of interest,

$$C_{Q_{1_\alpha}} = \vec{\phi}_1^{\intercal} Q_{a\alpha} \alpha. \tag{5.14}$$

The final partition A_e captures both the "pure" structural dynamics and the influence that displacement of one mode can have on other structural modes through aerodynamic interaction. Recall that the total structural displacement is approximation with a reduced number of mode shapes (5.9). Substituting that approximation in the global structural dynamics yields

$$\mathbf{M}\Phi\ddot{\vec{\eta}} + \mathbf{K}\Phi\vec{\eta} = \vec{F}. \tag{5.15}$$

Next, pre-multiply (5.15) by $\Phi^\intercal$,

$$\Phi^\intercal\mathbf{M}\Phi\ddot{\vec{\eta}} + \Phi^\intercal\mathbf{K}\Phi\vec{\eta} = \Phi^\intercal\vec{F}. \tag{5.16}$$

The modeshapes can be normalized such that $\Phi^\intercal\mathbf{M}\Phi = \mathbf{I}$, and $\Phi^\intercal\mathbf{K}\Phi = \Lambda$, where $\mathbf{I}$ is an identity matrix, Λ is a diagonal matrix composed of the eigenvalues. The diagonal structure of these dynamics allow an initial decoupling of the modes. The partition A_e is nominally composed of these decoupled modal dynamics (with an estimate for damping added to each considered mode). However, for the aero-structural system at hand, the generalized force vector $\vec{Q} = \Phi^\intercal\vec{F}$, can include aerodynamic force generated due to structural displacement. This effect re-couples the modal dynamics with force derivatives of the form $C_{Q_{\eta_i \eta_j}}$, i.e. a generalized force generated on the i-th mode due to deflection of the j-th mode. These generalized force derivatives can be computed from the static aeroelastic analysis as

$$C_{Q_{\eta_i \eta_j}} = \vec{\phi}_i^\intercal Q_{aa}\vec{\phi}_j. \tag{5.17}$$

We now illustrate the use of the GWB model in this type of flight dynamics formulation. Figure 5.6a depicts the gust-to-pitch rate Bode-magnitude plot for the linear flight dynamics where 11 symmetric modes were used to approximate structural displacement. Note the short period and first structural mode are separated by less than one decade. Figure 5.6b demonstrates the contribution to changes in wing root bending moment from each of the first four structural modes when the aircraft is subjected to a vertical discrete gust. This plot demonstrates how the availability of the full aero-strucural model allows for load recovery techniques like the modal displacement or summation-of-forces methods to compute internal loads at locations of interest.

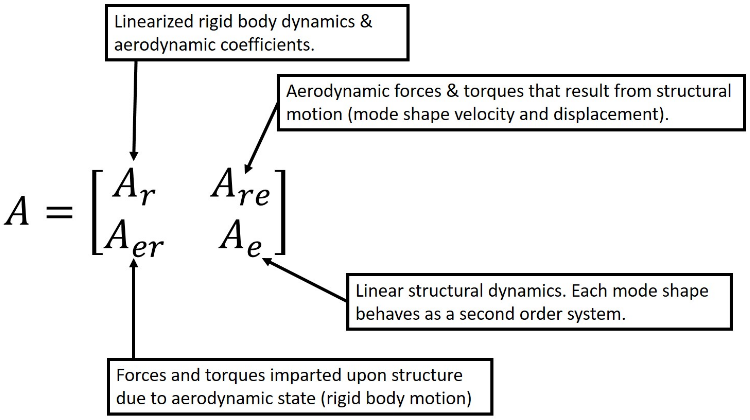

Figure 5.5: Partitioning that results in a typical approach to aero-structural flight dynamics.

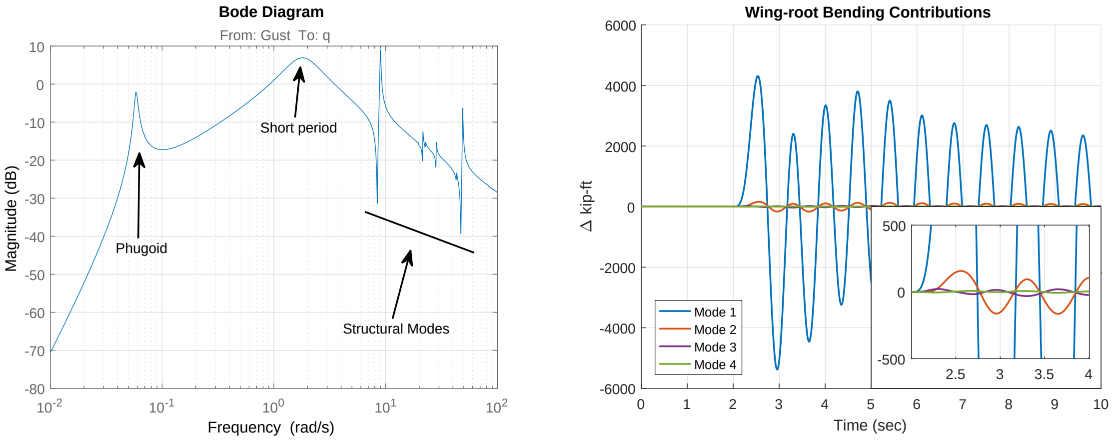

(a) Bode magnitude of vertical gust (m/s) to pitch rate (rad/s).

(b) Modal contributions to wing root bending moment from gust excitation.

Figure 5.6: Analysis highlights for an example set of GWB linear longitudinal dynamics.

5.4 Simulation

The Generic Wide Body aircraft model was reported for the open literature as a completely un-reduced aero-structural model with the intent that the raw model information granted the most latitude in its use as a tool for simulating and validating aeroelastic control schemes. While the example in the previous section briefly demonstrates the use of raw model data to create longitudinal flight dynamics, the breadth of simulation and validation capability afforded by the model goes far beyond what was demonstrated. For examplesc control design studies may focus on: lateral-directional or full six degree-of-freedom dynamics; effects of controllers designed for rigid body behavior being flown on a flexible airframe; effects of sensor and actuator nonlinearities; effects of various control surface "ganging" strategies in load alleviation scenarios; or effects of flying a control system through various regions of the flight envelope. Creating and documenting a new dynamic model for each case would be cumbersome and quite likely error-prone.

The Flexible Aircraft Control Evaluation Tool (FACET) is a MATLAB/Simulink project developed to provide a consistent interface to the GWB model data with configuration options to address the needs of a wide variety of control system investigations. Upon starting the tool, the user is prompted to configure (or load a prior configuration) the following options:

Plant The plant dynamics can be configured as full six degree-of-freedom, or constrained to longitudinal or lateral-directional degrees of freedom. For any of these rigid body dynamics options, the plant can be configured to include or exclude structural dynamic behavior, i.e. the plant can be configured as a purely rigid body or as an aeroelastic system.

Sensors Configurations include ideal (where exact measurement equations are applied), or non-ideal (where the non-ideal implementation allows the addition of sensor noise, measurement quantization, and sensor delay).

Actuators Here configuration options include ideal (where commanded deflections are attained instantaneously) and non-ideal (where options include first or second order actuator dynamics, saturation, deadband, hysteresis, delay, and rate limitations).

Estimator Options include the ideal estimator (perfect and direct state measurement without estimator dynamics) and a linear continuous or discrete-time Kalman filter.

Flight Condition Here the user can select the airspeed (Mach number) and altitude from within a given flight envelope, as well as the type of atmospheric disturbances to be applied (discrete or continuous gusts for example).

These configuration options are implemented through "variant" subsystems in the Simulink framework. As depicted in Fig. 5.7, each major component of the simulation has variant implementations. The architecture of the simulation is solidified by the signal buses that connect these major components. In other words, no matter how the simulation is configured, the communication between major components is standardized. One major advantage of this architecture is the ability to rapidly compare system behavior for different selections of plant, actuator, or sensor, or controller dynamics. The variety of model implementations is displayed in Fig. 5.8 where variations of the frequency and damping of the short period rigid body mode are depicted with respect to the nominal flight envelope.

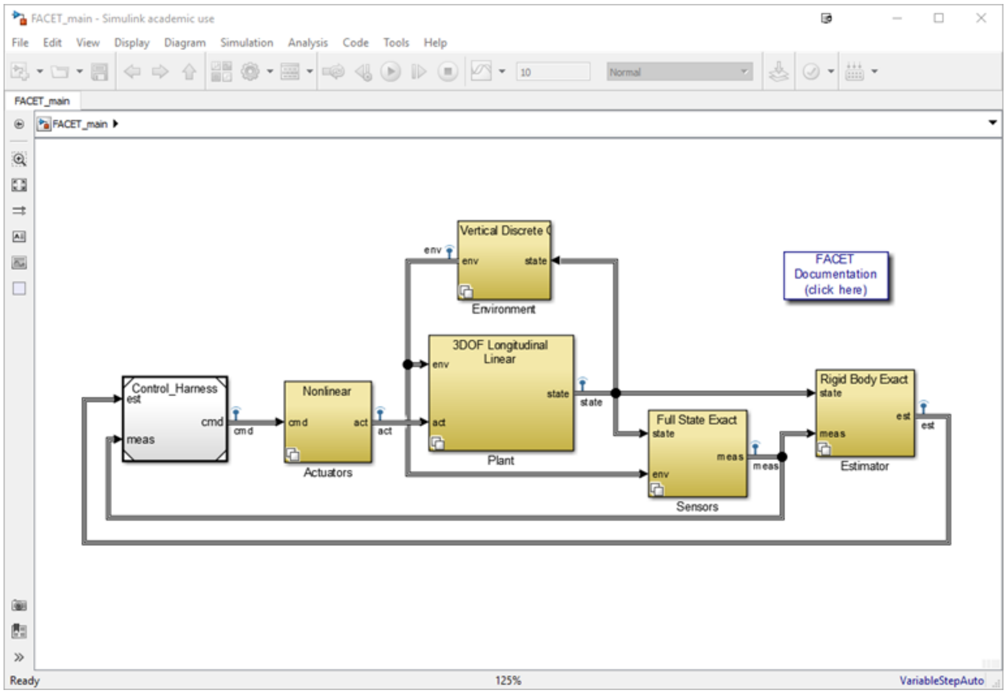

Figure 5.7: Top level of the FACET Simulink diagram.

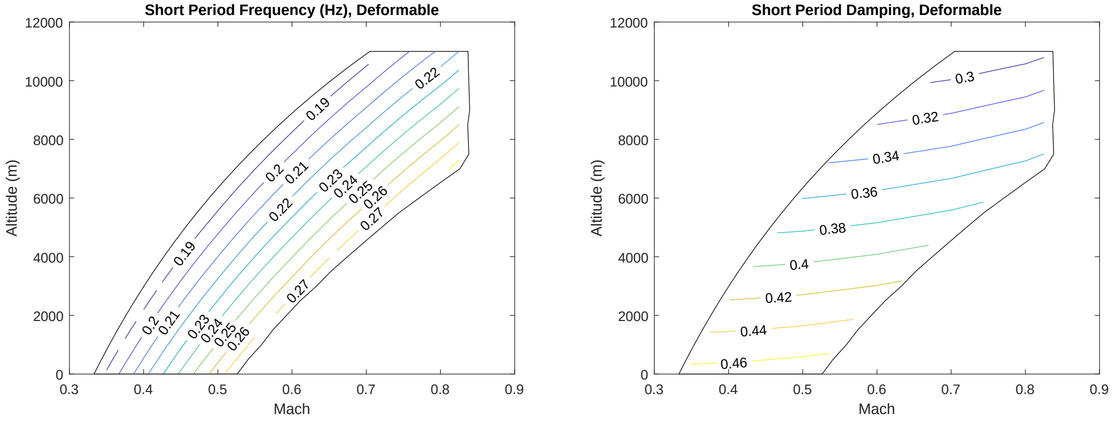

(a) Frequency (Hz)

(b) Damping ratio

Figure 5.8: Variation in short period frequency and damping over the nominal GWB flight envelope.

Chapter 6

AEROELASTIC TEST ARTICLE

Recent years have seen rapid developments in technologies that affect aeroelastic control challenges: new aircraft are designed with increased flexibility, where interactions between rigid-body and elastic dynamics are tightly coupled. Operational envelope expansion and new designs lead to structural, aerodynamic, and actuation nonlinearities. Distributed sensing and actuation, new developments in control law synthesis, and computing power are each expanding the design space in which active control positively impacts the aircraft response to gusts. Despite major developments in computational modeling and simulation of aeroelastic and aeroservoelastic systems, uncertainty of the mathematical models of such systems can still be considerable in many cases. Experimental studies of sensing, actuation, and control approaches to the aeroelastic control problem are still extremely valuable.

Recall the state of affairs described in Chapter 1: the cost of flight testing new control technologies at full scale is very high. Flight testing small UAVs can be more affordable but it suffers from its own challenges regarding scaling, hardware, and flight operations. In both cases obtaining desired gust inputs in a repeatable way is challenging. Wind tunnel tests for aeroelastic control studies offer controlled and repeatable environments for development at lower costs than flight tests [17, 18], but have traditionally revolved around precisely scaled and precisely tuned aeroelastic test articles that create impediments to rapid test because of high cost, complexity, and care (fragility).

There is, therefore, a need for small-scale aeroservoelastic models of flight vehicles for aeroelastic control technology tests that would represent the key physical mechanisms and interactions involved and would allow rapid access at low cost. We have developed such a test-bed for demonstration of control algorithms for the low-speed 3' x 3' wind tunnel at the University of Washington. The sections to follow describe this wind tunnel test-bed including model requirements, design, construction, and validation tests with details of the dynamics to be used for aeroelastic control system research.

6.1 Development

The design of the new test article was dominated by two basic guidelines: First, the test environment would be the $3' \times 3'$ test section of the low-speed wind tunnel at the University of Washington. Second, the test article would need to exhibit aerodynamically coupled rigid-body and structural dynamics to be the focus of active control law design and experiment. The sections that follow describe the test article configuration, sizing, and design details that reflect the convergence of these guidelines.

6.1.1 Model Configuration

Figures 6.1 and 6.2 illustrate the primary elements of the final configuration and the test article in the context of the wind tunnel test section. The basic configuration of the test article is a conventional wing-fuselage-tail arrangement; this choice reflects the desire to capture conventional flight dynamics if the article were built completely rigid. Note that the test article is not intended to precisely scale aerodynamic properties of any particular aircraft. Rather, the goal is to exhibit generic dynamic characteristics that present challenges to active control systems involving flexible aircraft dynamics. Toward that goal, the configuration of the test article is composed of three main structural components each of which can be tailored to include or exclude particular dynamic traits. The three main structural elements are the fuselage beam, the wing beam, and the cylindrical tip mass attached to the end of the wing beam. As an example, the first torsional mode of the wing structure can be exaggerated or attenuated by exchanging the tip mass for one of longer or shorter dimension. Design considerations like aerodynamic fairings, wing twist, wing taper, etc. are foregone here because aerodynamic efficiency has relatively little bearing on the achieved aeroelastic dynamics. Finally, the test article is mounted to the tunnel with an assembly that permits a rigid-body pitch degree of freedom.

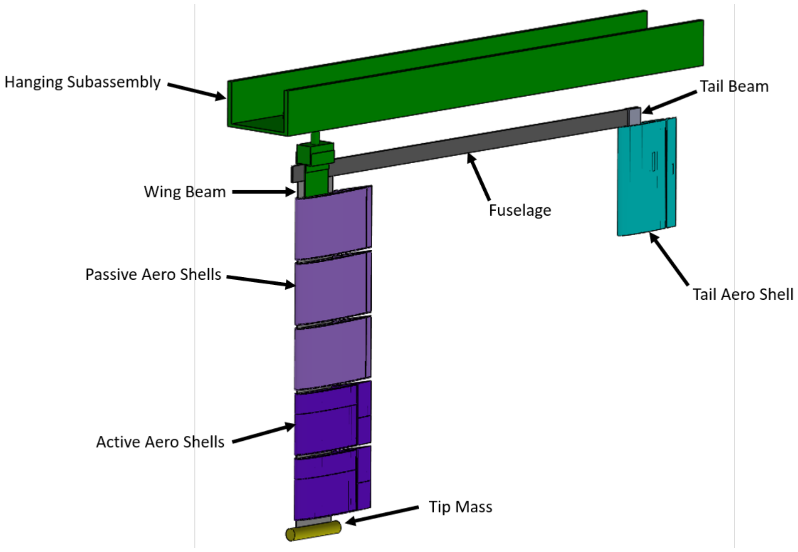

Figure 6.1: Primary elements of the test article and mounting assembly.

Note in Figure 6.2 that the test article is "ceiling mounted" in the wind tunnel test section. Mounting the hardware vertically and from above minimizes gravitational effects on the structural dynamics and alleviates a wing-beam buckling limitation that would exist in a floor mounted configuration. Also, the existing wind tunnel test section infrastructure is much more conducive to vertically mounted models. If gravitational effects are deemed important for some tests, horizontally mounted models can be easily tested in the University of Washington's Kirsten Wind Tunnel.

6.1.2 Structural Sizing

Having the overall configuration decided, the sizing of the main structural components was conducted using a structural dynamic optimization based on handbook formulas. For the optimization the wing beam was parameterized by its cross sectional width (w) and height (h) while the tip mass was parameterized by its radius (r) and length (ℓ). The mathematical

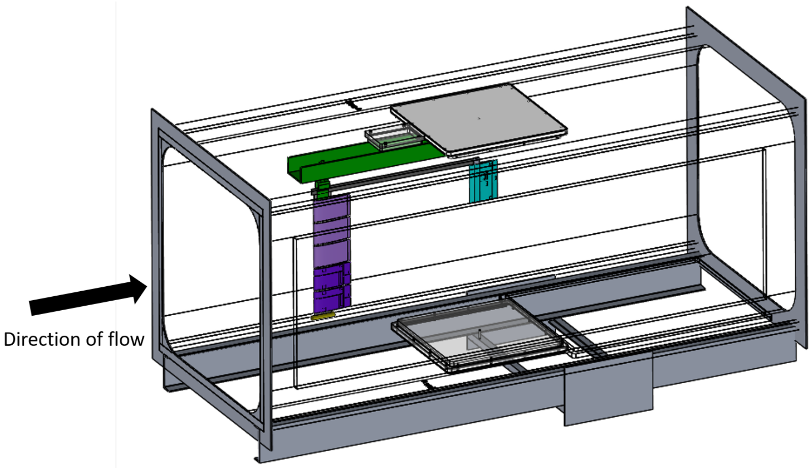

Figure 6.2: Test article mounted in the wind tunnel test section.

optimization problem has the following form,

$$
\begin{aligned}
\min_{w,h,r,\ell} \quad & J(r,\ell) \\
& \text{subject to} \\
& g_1(w,h,r,\ell) \leq 0, \\
& \quad \vdots \\
& g_n(w,h,r,\ell) \leq 0,
\end{aligned}
\tag{6.1}
$$

where the cost function and $n = 12$ constraint equations are detailed in the following. The cost function is the mass of the wing tip cylinder (with material density ρ_{tm}), to be minimized

$$J(r,\ell) = \rho_{tm} \cdot \pi r^2 \ell. \tag{6.2}$$

The first eight constraint equations are upper and lower bounds on each of the four optimization variables (implemented to prevent unreasonable dimensions in a solution). The ninth constraint is a maximum strain requirement;

$$\frac{\sigma_{max}}{\sigma_{yield}} - 1 < 0, \tag{6.3}$$

where σ_{yield} is the yield stress of the wing beam material. The value σ_{max} is the maximum stress on a uniform cantilevered beam carrying a uniform distributed load (approximate and conservative),

$$\sigma = \frac{My}{I}, \tag{6.4}$$

where I is the area moment of inertia of the beam cross section, y is the maximal cross section height from the cross section area centroid, and M is the value of bending moment at the wing root. The wing root moment is approximated as the second integral of a uniform load distribution where the load comes from an approximation of the aerodynamic lift corresponding to a 10 degree steady angle of attack. The lift approximation is made assuming an ideal lift slope ($C_{l_\alpha} = 2\pi$) with a standard correction for application to a finite wing, [1]

$$L = qSC_{L_\alpha}\alpha \tag{6.5}$$

$$C_{L_\alpha} = \frac{\pi Æ}{1 + \sqrt{1 + (\pi Æ/C_{l_\alpha})^2}}, \tag{6.6}$$

where q is the flight dynamic pressure, S is the reference area, α is the applied angle of attack, and $Æ$ is the finite wing's aspect ratio.

The tenth and eleventh constraints address the natural frequencies of the first bending and torsional modes of a uniform cantilevered beam. For a beam with distributed weight (w), a tip weight (W), and length (L), the natural frequency of the first bending mode (in Hz) is approximately [87]

$$\omega_b \approx \frac{1}{2\pi}\sqrt{\frac{3EIg}{WL^3 + 0.236wL^4}}, \tag{6.7}$$

where E is the material modulus of elasticity and g is a constant gravitational acceleration. The constraint for the optimization provides an upper bound on ω_b. Similarly, for a distributed rotational inertial (I_s) and a tip inertia (I), the natural frequency (in Hz) of the first torsional mode is approximately [87]

$$\omega_t \approx \frac{1}{2\pi}\sqrt{\frac{GJ}{(I + I_s/3)L}}, \tag{6.8}$$

where G is the material shear modulus of elasticity and J is the torsional stiffness constant of the beam cross section. For the sizing of the first model the optimization imposes a lower bound constraint on ω_t to ensure the mode is outside the range of actuation bandwidth and outside the concern of dynamic interaction with other structural modes through control law action. However, in order to evaluate designs of future models, where more elastic modes are brought into the bandwidth of actuation and into interaction with other modes, versions of the optimization were run with this constraint used as an upper bound to *ensure* the torsional mode be present for such interaction. It was found that both designs could be accomplished with a simple exchange of tip mass; a shorter tip mass satisfied the first design case (only wing bending within actuation range) while a longer and narrower mass could provide the necessary rotational inertia to reduce the frequency of the torsional mode as desired.

The final constraint addresses beam tip deflection at the maximum expected static load. While the static stress constraint ensures structural integrity, the design must also limit the deflection of the wing to a range of deformations under load that would keep the wing centered and away from the wakes of vanes of the gust generation system and prevent nonlinear structural behavior due to large deformation. The allowed tip deflection under max static load can be tailored to the needs of each model to be built and tested. For the uniform cantilevered beam with uniform distributed load q (a simple way to account for tip deflection, using simple, conservative math models) the tip deflection is given by [88]

$$y_t = \frac{qL^4}{EI}. \tag{6.9}$$

In the optimization y_t is constrained by an upper limit.

Figure 6.3 provides representative results from the optimization studies. As the operational speed and wing span are not fixed at a particular value, a parameter space of the two was meshed and the optimization solved at each point on the resulting grid. The simplicity and small dimension of the design problem presented above allowed a complete optimization survey of the gridded parameter space ($\sim$440 conditions) in a matter of minutes on a basic desktop computer.

The results for the preliminary tests (torsional mode at high frequency) all returned beam

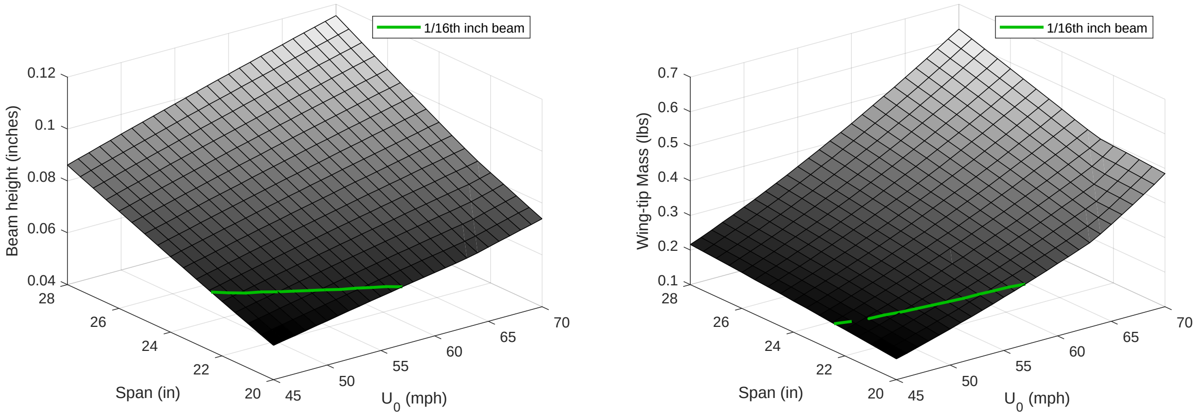

(a) Optimal beam heights.

(b) Optimal tip mass values.

Figure 6.3: Sample of structural optimization results with solutions for a 1/16" beam highlighted.

cross sections at their maximal width (3") and with the natural frequency of the first wing bending mode at its upper limit (2 Hz). The height of the beam cross section and the weight of the wing tip mass, as depicted, demonstrate a fair amount of variation in optimal solutions over the parameter space. The highlighted curves correspond to a family of solutions with 1/16" beam height (one of several stock aluminum bar/beam thicknesses which, if procured directly, alleviates need to mill or otherwise fabricate the desired dimension).

6.1.3 Design Details

Ultimately, the design chosen from the sizing optimization was one of the 1/16" wing beam designs with the shortest wing span. Note that optimization sized the tip mass and wing beam. The fuselage beam was sized such that when made of aluminum the first body bending mode would be under 5 Hz, but when made of steel the mode would have a natural frequency greater than 10 Hz.

From these basic sizing parameters the detailed design was completed with an emphasis on modularity and simplicity. For example, the aerodynamic shells on the wing are designed as either active (contain a servo motor and control surface) or inactive, but are otherwise interchangeable in terms of size and mounting assembly to the wing beam. The airfoil for both the wing and horizontal stabilizer is a symmetric and relatively thick NACA-0012 to help accommodate an embedded servo motor. As another example, the fasteners connecting the fuselage, wing, and tip-mass are fitted with nyloc self-locking nuts, but are all left exposed (no aerodynamic fairing) for ease of inspection. Additional details of the aerodynamic configuration are depicted in Figure 6.4; details of the structural configuration are provided in Table 6.1 and depicted in Figure 6.5.

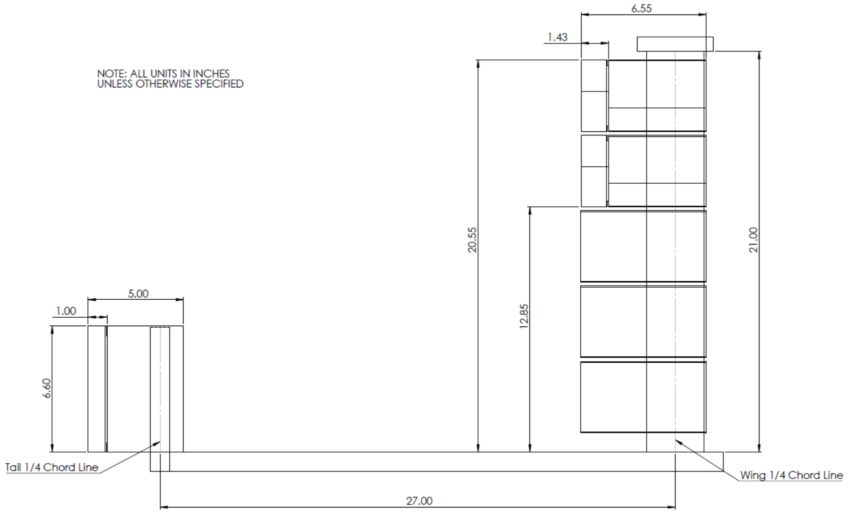

Figure 6.4: Details of the test article aerodynamic configuration.

In terms of actuation the model has two aileron control surfaces and a single elevator surface. Each surface is driven by an RC-type servo motor small enough to be embedded inside the contour of the corresponding aero-shell. In particular, the MKS HV6130 thin-wing servo was selected based on its size, torque, and power requirement. Unfortunately, the dynamic bandwidth of RC-type servo motors is not part of the product specification as would otherwise be standard for an industrial type servo. As a result, Sec. 6.3 describes a

Table 6.1: Overview of structural components.

(a) Materials

Component	Material
Wing Beam	Aluminum 6061-T6
Tip Cyliner	Brass
Aero-shell	Polylactic Acid (PLA)
Fuslage Beam	Low Carbon Steel
Tail Beam	Aluminum 6061-T6

(b) Masses

Component	Weight (lb)
Wing Beam	0.367
Tip Cylinder	0.276
Active Aero-shell	0.209
Passive Aero-shell	0.132
Fuselage Beam	0.986
Tail Beam	0.146

system identification effort undertaken to identify the dynamic capability of the servos.

The mounting assembly depicted in Fig. 6.2 demonstrates that a traditional force and moment balance is not part of the experimental apparatus: all measurements are made from sensors on the test article itself. The first of the quantities to be measured is the rigid-body rotation angle (pitch angle). A Hall effect sensor was fitted to measure this rotation atop the hanging assembly. This sensor is a non-contact sensor which employs two components: a magnet attached to the test article and a device to measure rotation of the associated magnetic field.

Next, a pair of uni-directional accelerometers are mounted at the forward and aft corners of the wing beam at the wing tip. Because the model is constrained from rigid-body plunge translation, the displacements measured at the wing tip can be used to measure the wing's bending and torsional motions. In addition, a strain gauge is attached at the wing root for a direct measurement of bending strain. The accelerometers and strain gauge are complimentary in sensing the structural state of the wing (a quantity of interest in gust load alleviation control law design).

Finally, rotary potentiometers are installed on the output shaft of each of the control

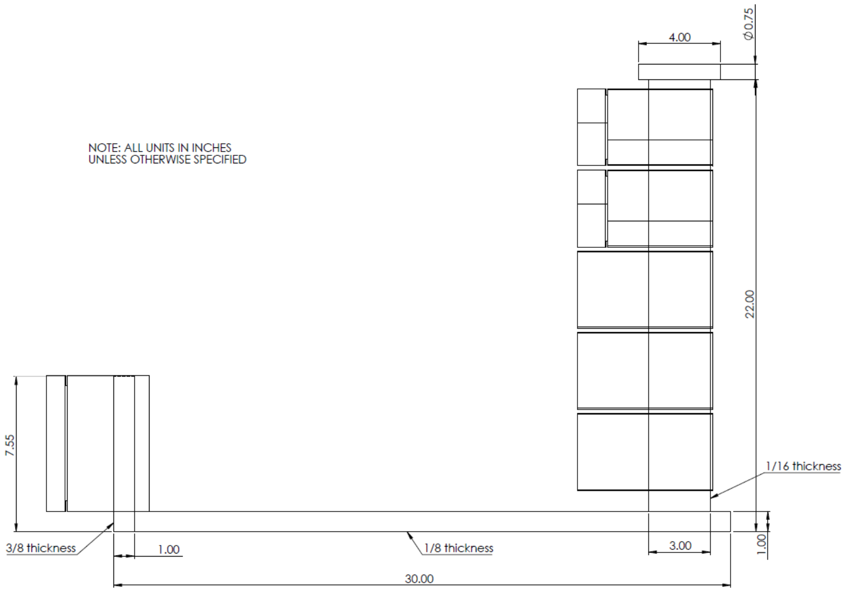

Figure 6.5: Details of the test article structural configuration.

surface servo motors. Low-cost miniature servo motors are usually input-only devices, typically driven by a Pulse Width Modulated (PWM) signal. The potentiometers allow for more complete feedback control, and provide a measure of health monitoring as the motors are subject to gear slippage, overheating, and variable performance with variation in input voltage. The general location of these potentiometers as well as the locations of the other sensors and actuators are shown in Figure 6.6.

6.2 Modeling

Mathematical models that capture the physical behavior of a system to be actively controlled are the foundation for any control law synthesis for such systems. Their development requires a tradeoff between fidelity and complexity. This section describes the approach used in modeling the new wind tunnel models for GLA technology tests.

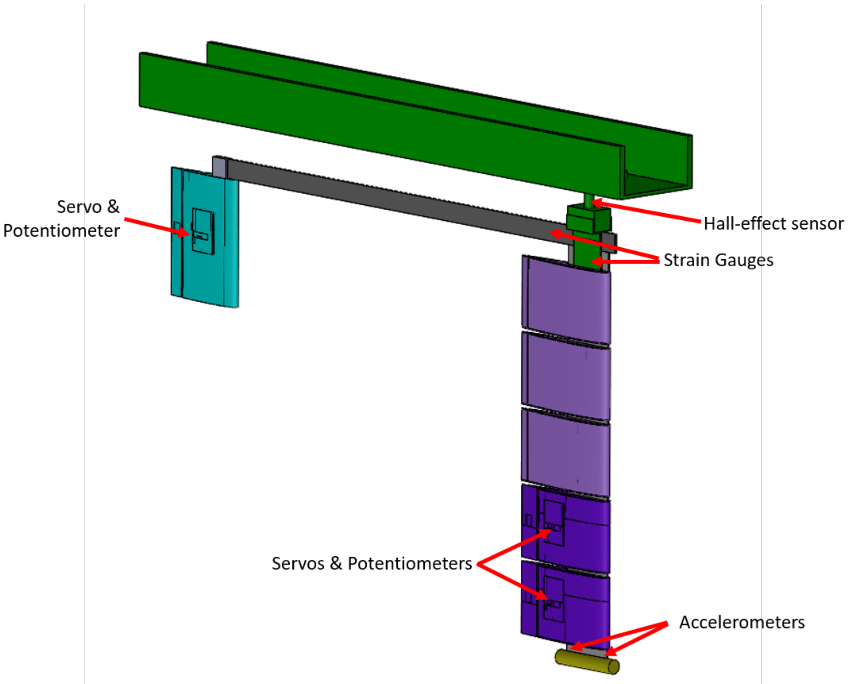

Figure 6.6: General arrangement of sensors and actuators on the test article.

6.2.1 State Space Model

The modeling method employed for this work originated in the 1960s [3] and is a standard method detailed in flight dynamics and control textbooks [43, 42]. The basis of the method is to utilize the mean-axis approximation such that unforced rigid-body and structural dynamics are decoupled. The two sets of dynamics are then coupled through the forcing functions, i.e. aerodynamic loads become dependent on the deformed shape of the structure, and generalized forces on the structure become dependent on the aerodynamic state of the rigid body. These dependencies are derived assuming small structural deflections, small angles of aerodynamic incidence, and small changes in mass or inertia of the structure. Chapter 5 provided a description of how a linear time-invariant state space representation can be generated using the quasi-steady aerodynamic analysis of a NASTRAN finite element model of a flexible aircraft. Such a model has the form

$$\dot{\mathbf{x}}(t) = \mathbf{A}\mathbf{x}(t) + \mathbf{B}\mathbf{u}(t), \tag{6.10}$$

where the state vector, $\mathbf{x}(t)$, is comprised of the common rigid-body states (angle of attack, pitch angle, forward speed, etc.) as well as motions in modal coordinates of the structural states. Modal coordinates are used to approximate structural deflection ($\mathbf{q}$) in terms of a specific reduced order basis,

$$\mathbf{q} \approx \mathbf{\Phi}\eta, \tag{6.11}$$

where $\mathbf{\Phi}$ is a matrix of normal modes (or other selected modes) and η is the vector of modal coordinates. Again, the dynamics are inherently partitioned as depicted in Fig. 5.5. In terms of modeling confidence the purely structural dynamics partition (A_e) is the most accurately modeled partition because the associated assumptions are the least strained by actual implementation. On the other hand, the remaining partitions rely on the quasi-static analysis of the NASTRAN model and are not as amenable to isolation for test or validation. The notion of modeling confidence will be revisited later; here we can note an expectation that rigid-body assumptions are automatically strained by the physical attachment of the test article to the hanging assembly.

6.2.2 Finite Element Analysis

NASTRAN was used to create a detailed structural dynamic model of the complete system. The NASTRAN model is composed of discrete concentrated masses and of beam elements (sometimes referred to as a “ball-and-stick” model). Doublet Lattice Method (DLM) unsteady aerodynamic modeling was used together with NASTRAN splining between structural and aerodynamic meshes. Figure 6.7 shows both the structural and combined aero-structural NASTRAN models of the wind tunnel test article.

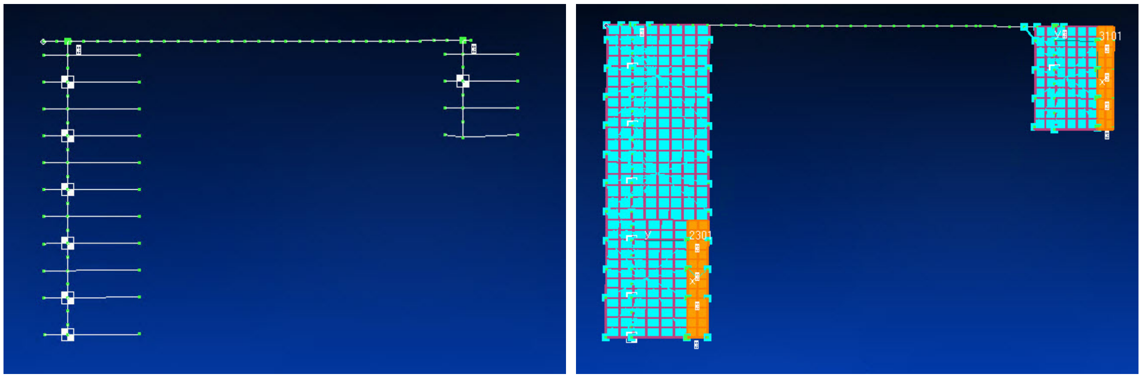

(a) Structural FEM (b) Aero-structural FEM

Figure 6.7: Visualizations of the structural and aero-structural finite element models of the test article.

As discussed in Section 6.1, the test article has been configured with an emphasis on interchangeable configurations, i.e., through changes to tip mass and fuselage stiffness additional structural modes can easily be brought into interaction with the active gust load and flight control systems. Beyond the simple handbook approximations that idealize portions of the various configurations, the NASTRAN aero-structural models provide *full vehicle* structural characterizations. For example, Table 6.2 summarizes structural mode shapes for the complete model as obtained from the FEM.

Table 6.2: Mode shapes and frequencies of the NASTAN aero-structural model.

Mode shape description	Frequency (Hz)
Rigid-body pitch	0.0
First wing bending	1.7
First fuselage vertical bending	11.3
First fuselage lateral bending	16.9
Second wing bending	22.8

6.3 Pre-tunnel Testing

The detailed design of the test article included some assumptions that needed to be verified before incorporating in the final product. The first assumption had to do with the dynamic capability of the RC-type servo motors used to actuate the control surfaces. The second assumption was that the 3D-printed aerodynamic shells could be attached to the wing and that foam "filler" could be used to fill the intra-shell gaps without significantly affecting the desired structural properties. The following sections detail the validation of those assumptions as well as the ground vibration test results used to validate the FEM before progressing to aerodynamic tests.

6.3.1 Actuator System Identification

A traditional frequency sweep procedure was used for system identification of the servo actuators. Figure 6.8 depicts the arrangement of servo, output shaft, and potentiometer used for the system identification tests. The potentiometer is a rotary-type device used to measure angular displacement of the servo output shaft. The figure depicts the assembly broken out from the servo bay of the aero-shell; when assembled the white bay doors are flush with the yellow plastic of the aero-shell.

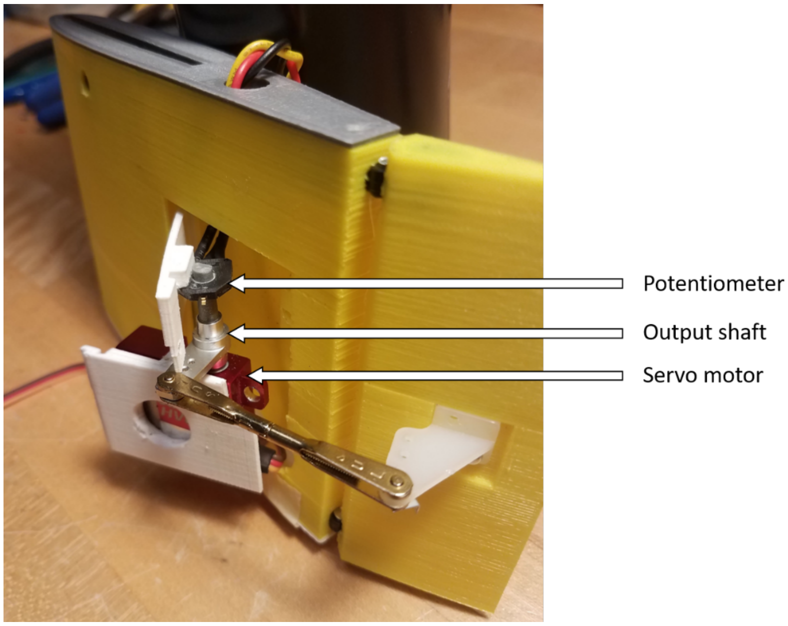

Figure 6.8: Hardware configuration for servo system-identification tests.

The servo under test is an MKS HV6130 thin wing servo. Both the command and measurement roles of the experiment are performed with a Simulink Real-time Desktop application. The signal flow of the experiment is summarized in Figure 6.9. Essentially the same architecture is used in closed loop control wind tunnel experiments; the delays, measurement resolution, etc. are representative of the final conditions.

Figure 6.10 depicts time histories of both the swept-sine input signal and potentiometer measurement signals as well as the corresponding mean-square signal coherence between the input and output. The sinusoidal input varies linearly in frequency over the sixty second test duration with uniform commanded amplitude;

$$u(t) = A\sin(\omega t),\ \omega \in [0.1\ 10],\ A = 15^\circ. \tag{6.12}$$

The right plot of Figure 6.10 shows excellent input-output coherence over the range of 0.5 to 8.0 Hz; suggesting strongly linear behavior well suited for representation with an LTI transfer function in that range.

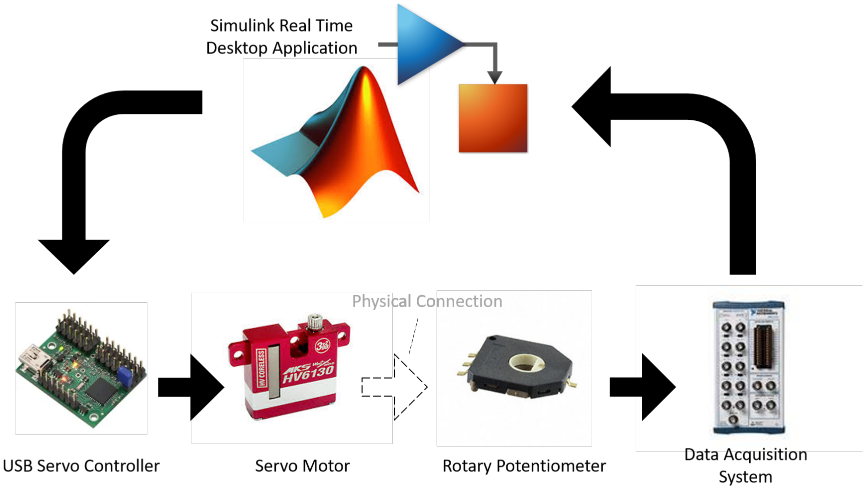

Figure 6.9: Signal flow in servo command and measurement loop.

Figure 6.11 depicts the estimated Frequency Response Function as well as two candidate transfer functions. The transfer functions were estimated assuming a second-order system. The first estimate assumes a parameterization with a single zero

$$\hat{G}_1(s) = \frac{k(s+b_0)}{s^2 + a_1 s + a_0}, \tag{6.13}$$

while the second estimate assumes a parameterization without a zero

$$\hat{G}_2(s) = \frac{k}{s^2 + a_1 s + a_0}. \tag{6.14}$$

Of the two transfer functions, both are reported to achieve better than 90% fit (a measure reported by the transfer function estimate routine). Table 6.3 reports the coefficients of the parameter estimates and the percentage fit achieved by either model.

The transfer function estimation routine only attempts to fit the frequency response function estimated from the sine-sweep test data. To help evaluate which of the candidate transfer function estimates may be most suitable, one option is to play back the swept-sine input and compare the simulated time domain response from the candidate models compared to the original measurements. Figure 6.11 shows that both estimated models

Table 6.3: Servo transfer function estimate results.

Model	gain (k)	b_0	a_1	a_0	Fit percentage
w/zero	3.7	312.5	52.8	1215	91.4
w/o zero	1394	-	62.2	1461	90.9

closely match the frequency response function in the $1-10\ Hz$ range, and within that range the discrepancies are greatest in the higher frequencies.

Figure 6.12 depicts some time domain comparisons of the candidate transfer functions; the left plot demonstrates how the expected output of the transfer functions compares to measurements in swept-sine experiment. Also in Fig. 6.12 there is a comparison of prediction to measurement for a step input to the servo system (a data set which was not part of the parameter estimation). The utility of the step response is to check that the *qualitative* response from the estimated model matches the measured signal. For example non-minimum phase behavior, overshoot, settling behavior, etc. In this case, both models exhibit a small amount of overshoot where the measured data demonstrates an overdamped response. Ultimately, the model without a zero was used for control system design as it showed slightly better agreement with the step response and had only slightly poorer fit to the frequency response function of the swept-sine experiment.

6.3.2 Structural Validation

Recall from Section 6.1, a standard technique in designing an aeroelastic wind tunnel model is to construct a simple metallic “backbone” structure which possesses the desired structural properties (stiffness, mass distribution, etc.) and then attach extremely light-weight aerodynamic “shells” to the backbone to give the model the correct aerodynamic shape. The shells should be designed so they have minimal impact on the structural properties of the model. For the test article, it was decided to use steel or aluminum backbone material and plastic

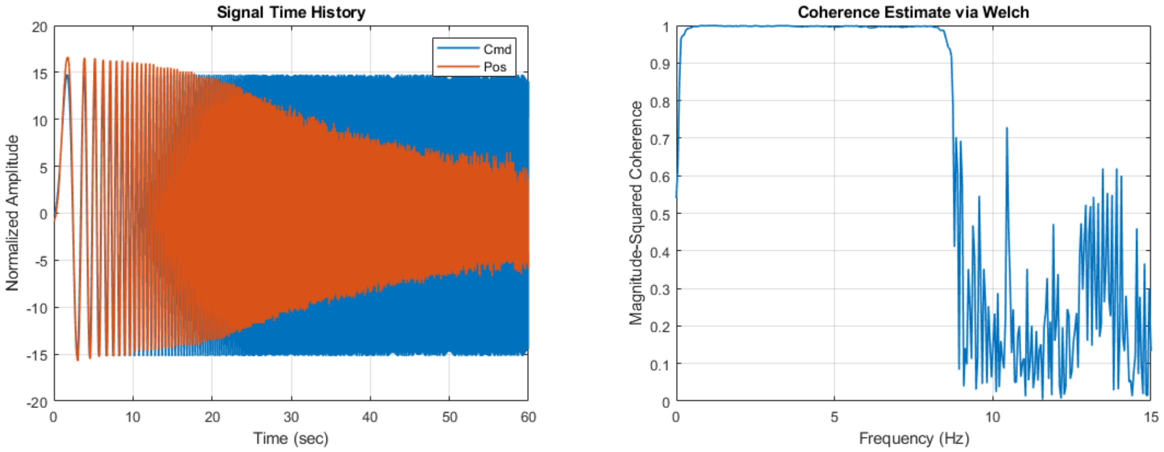

(a) Input-output time histories.

(b) Mean-squared signal coherence.

Figure 6.10: Signals used for servo system identification.

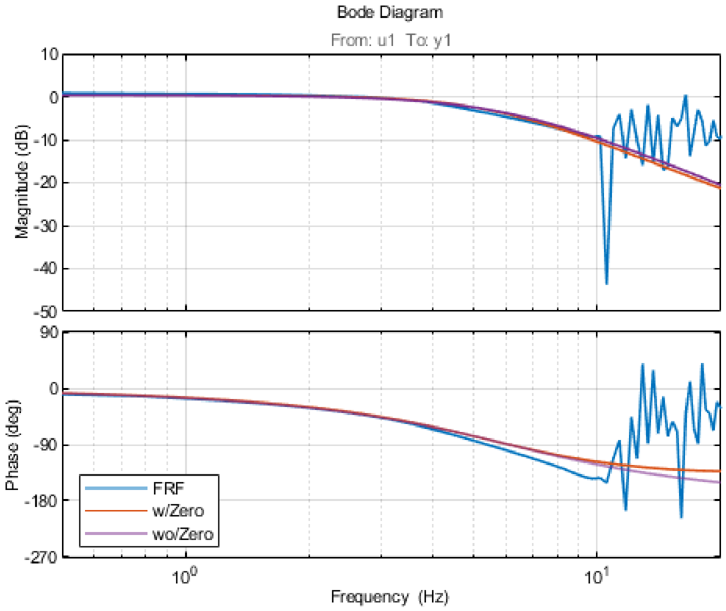

Figure 6.11: Estimated frequency response function and candidate transfer functions.

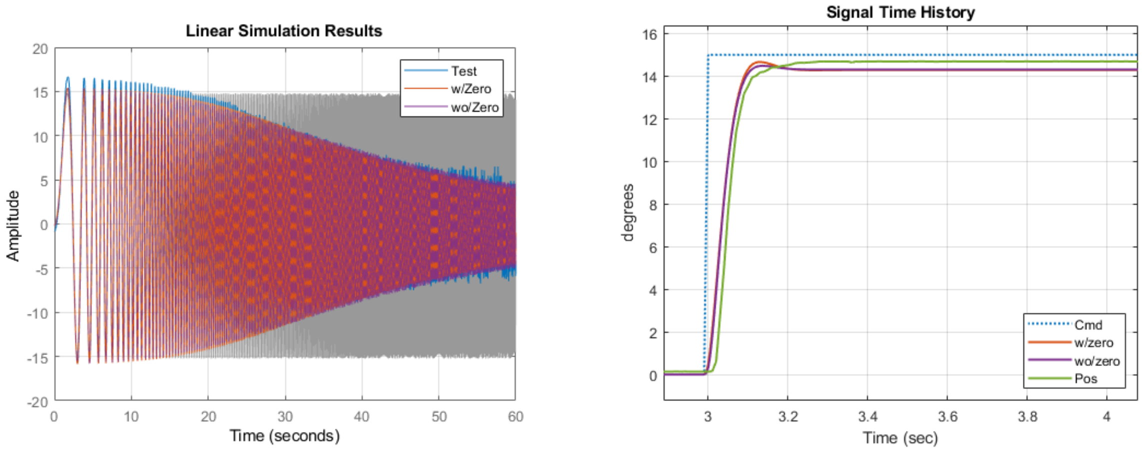

(a) Sweep response comparison.

(b) Step response comparison.

Figure 6.12: Time domain comparisons of transfer functions.

(3D printed) aero-shells. During development and fabrication of the test article, a series of vibration tests were carried out; first to assess the impact of 3D printed aero-shells on the structural dynamic characteristics of the backbone structure, then to assess the effects of foam-filler material between aero-shells, and finally to validate and tune the NASTRAN finite element model.

Vibration Testing Apparatus

The structural vibration tests were conducted using a laser vibrometer and impact hammer. The primary elements of the testing apparatus are depicted in Fig. 6.13; the excitation force is measured with an instrumented impact hammer and the system response is measured by the laser vibrometer. A signal analyzer system was used to record and relate the excitation and measurement signals. Table 6.4 catalogs the specific instruments used in the experiment.

Table 6.4: Equipment used in laser vibrometer experiments.

Component	Make	Model
Laser sensor head	Polytec	OFV-505
Vibrometer controller	Polytec	OFV-5000
Impact hammer	PCB Piezotronics	086C01
Signal analyzer	Spectral Dynamics	Jaguar

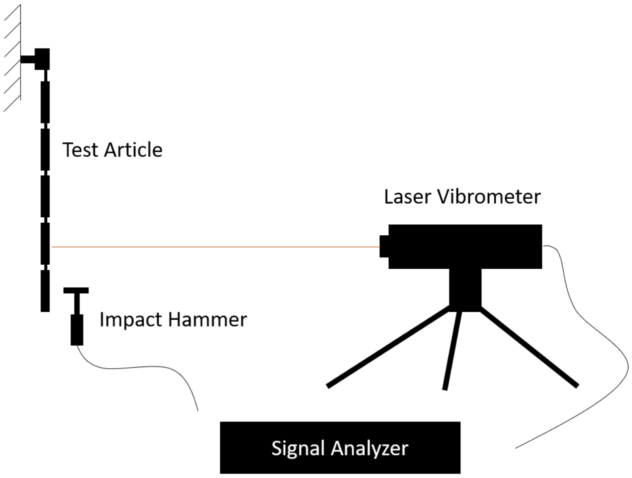

Figure 6.13: Primary elements of the vibration testing apparatus.

Aero-shell Assessment

The first set of experimental results were collected in an effort to determine whether or not the installation of plastic aero-shells to a simple wing beam would impact the frequency of the beam's first structural mode beyond that expected from added mass. The laser was used to measure the wing bending displacement at the 3/4 length of the beam (as measured from the point of cantilever). The essential characteristics of the wing beam are summarized Table 6.5. In the second case four 3D-printed aerodynamic shells were attached to the beam using a press-fit. The shells weigh 0.18 *lbs* each and only make contact with the wing beam at the edges of each shell since the shells are hollow. In this test there is a 0.75 *in* span-wise separation between each shell. The shells are 4.0 *in* wide and have a chord measuring 6.5 *in*. Each shell forms a NACA-0012 airfoil which gives a maximum shell thickness of 0.8 *in*.

Given the simplicity of the structure under test, the first bending frequency was predicted with analytical techniques for both cases. The first natural frequency of a uniform cantilevered beam is given by [87],

$$f_1 = \frac{3.52}{2\pi}\sqrt{\frac{EIg}{w\ell^4}}, \tag{6.15}$$

where E is the material Young's modulus, I is the beam's cross sectional inertia, g is the gravitational constant, w is the weight per unit length of the beam, and ℓ is the length of the beam. For the first test case the assumptions of this analytic form are well satisfied and the prediction is expected to be highly accurate. For the second test case with the aero-shells, Eq.(6.15) is reused as an approximation by simply adding the aero-shell masses to the distributed mass of the beam. The effect of added aero-shell mass is to lower the first natural frequency; the motivation for the experiment is to determine if the mounting of the aero-shells has the effect of increasing the effective stiffness of the beam. If the shells add stiffness, then by (6.15), the first natural frequency should decrease from added mass, but less than the prediction where stiffness remains fixed.

Figure 6.14 reports a comparison of the analytic and experimental values of the first natural frequency of the cantilevered wing beam. In that figure the yellow diamond depicts the experimental frequency to be expected if the analytic vs. experiment difference observed in the beam only case were subtracted from the analytic prediction of the aero-shell case. Given that the experimental frequency of the aero-shell case was lower than otherwise predicted, it was concluded that the shells do not substantially increase the wing's effective stiffness.

Table 6.5: Wing beam properties.

Property	Value
Material	Aluminum 6061
Length	20 *in*
Width	3 *in*
Height	1/16 *in*
Weight	0.347 *lb*

Foam-filler Assessment

In order for the aero-shells to have a minimal impact on the effective stiffness of the wing, the shells should not come into contact with one another during normal wing deformation. However, gaps between the shells degrade the nominal aerodynamic shape of the wing. Hence, a foam filler material was selected to fill the gap while not substantially changing the effective beam stiffness. Using the same laser vibrometer testing apparatus of Fig. 6.13, a series of four tests were conducted to assess the impact of the chosen filler material. The four configurations are enumerated in Table 6.6.

Figure 6.15 demonstrates the differences in the measured first wing bending due to foam for both the case when the tip mass is removed and when it is installed. From the figure, it can be seen that without the tip mass the foam appears to slightly lower the first bending frequency. However, with the tip mass installed the foam appears to have much less effect.

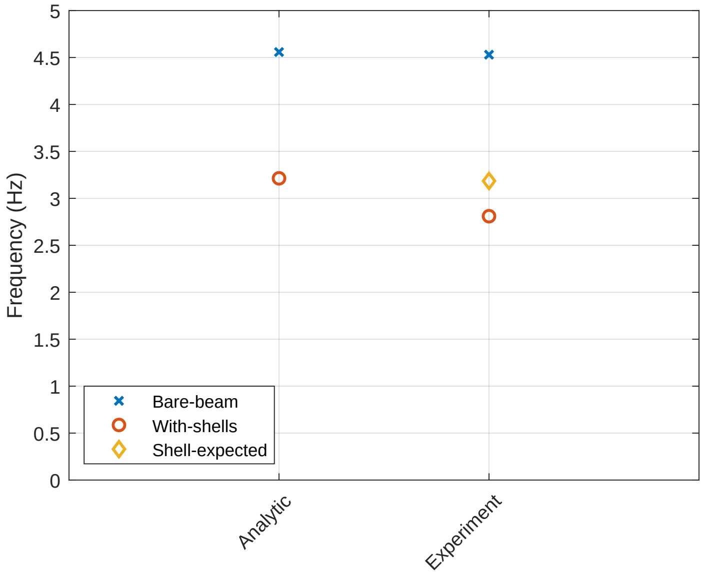

Figure 6.14: Changes in first wing bending frequency due to aero-shells.

Table 6.6: Test configurations of foam-filler experiments.

Configuration	Description
(-Foam,+Tip)	No foam inserts between shells; tip mass is attached to the end of the wing
(-Foam,-Tip)	No foam inserts; no tip mass
(+Foam,-Tip)	Foam inserts installed; no tip mass
(+Foam,+Tip)	Foam inserts installed; tip mass attached

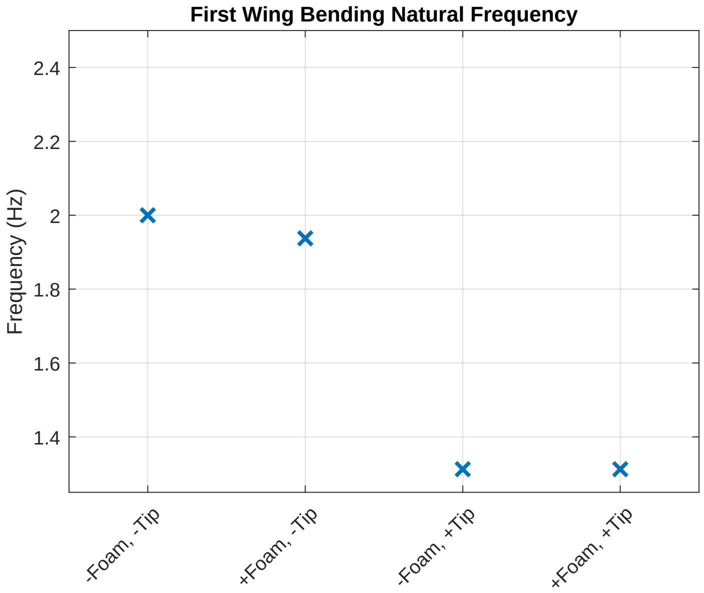

Figure 6.15: Changes in first wing bending frequency due to foam and tip mass.

The measurement of first wing bending frequency comes from a single peak on an auto-power spectral density plot from one of the impact-hammer tests. On the other hand, using the logarithmic decrement method, one such test yields several opportunities to estimate the damping ratio of the mode. Figure 6.16 gives a comparison of these estimates for each of the four configurations. The results in Fig. 6.16 are not conclusive; i.e., a statistically significant change in damping ratio was not recorded with the addition of filler foam between the aero-shells.

FEM Validation

The purely structural portion of the NASTRAN model of the test article is a ball-and-stick type with four overall structural elements: the wing, the fuselage, a horizontal tail, and a wing-tip mass. The structure of the finite element model is constrained where the quarter-chord of the wing meets the fuselage. The motion constraint is in every degree of freedom except for rotation about the pitch axis. While this finite element model is the one used for

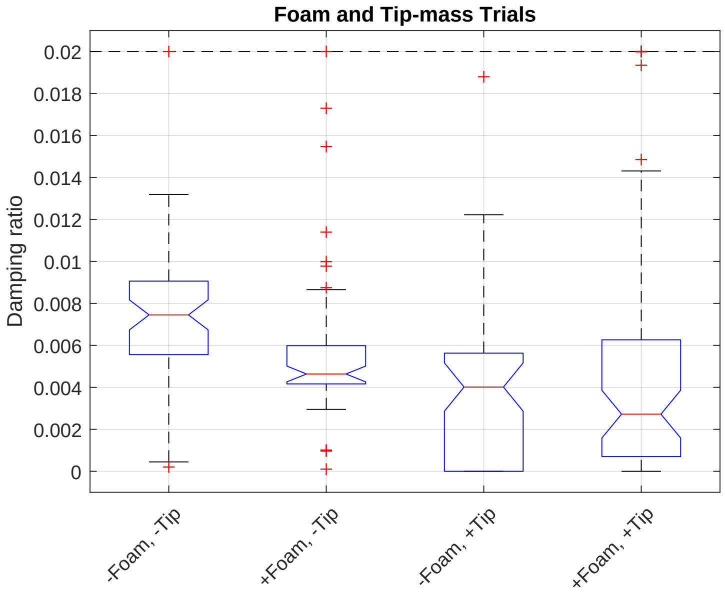

Figure 6.16: Changes in first wing bending damping due to foam and tip mass.

the creation of the mathematical model for simulation and control, the vibration tests were not practical to conduct with the rigid-body degree of freedom left unconstrained. Thus, a variant of the FEM that was fully constrained was used for comparison to vibration data taken from the full model. In practice, this choice led to two sets of tests: vibration tests were performed with the impact hammer and laser vibrometer on first the wing, and then on the tail. In both cases the model was clamped at the wing-fuselage joint to prevent any rigid-body motion. These two sets of full test article vibration tests show the modal frequencies given in Table 6.7.

Following this testing, modifications were made to the NASTRAN model to improve the correlation with the structural vibration test results. Emphasis was made to align the lower frequencies' modes, especially those within the actuator bandwidth. The following specific changes were made.

- Added weight in concentrated masses to the wing to account for systems (wiring, accelerometers, etc).

Table 6.7: Full test article structural vibration test results.

Mode Shape Description	Frequency (Hz)
First wing bending	1.4
First fuselage vertical bending	3.1
Second wing bending	10.1
Fuselage lateral bending	18.5
Second fuselage vertical bending	21.6

- Increased thickness of fuselage spar from 0.125 in to 0.129 in.

- Reduced fuselage density to 7750 kg/m3.

The resulting NASTRAN aero-structural model frequencies are given in Table 6.8.

Table 6.8: Mode shapes and frequencies of the NASTRAN aero-structuralmodel post test-correlation.

Mode Shape Description	Frequency (Hz)
First wing bending	1.4
First fuselage vertical bending	3.0
Second wing bending	10.5
Fuselage lateral bending	23.1
Second fuselage vertical bending	26.8

Finally, the wing root clamp was removed from the NASTRAN model to evaluate the model when it is free to rotate in pitch. The modal frequencies are shown in Table 6.9.

Table 6.9: Mode shapes and frequencies of the NASTRAN aero-structural pitch free model.

Mode Shape Description	Frequency (Hz)
First wing bending	1.4
Second wing bending	10.5
Fuselage vertical bending	17.8
Fuselage lateral bending	23.2

For the first wing bending mode, the initial NASTRAN model prediction was 1.7 Hz, the structural vibration test result was 1.4 Hz, and the correlated NASTRAN model result was 1.4 Hz. The structural test result frequency aligns exactly between the structural vibration test result. For the the fuselage vertical bending mode, the initial NASTRAN model prediction is 16.9 Hz, the structural vibration test result was 21.6 Hz, and the correlated NASTRAN model result was 17.8 Hz. For this mode the NASTRAN model frequency is 18% below the test result. This margin of error was determined to be acceptable due to the fact that this mode is well beyond the actuator bandwidth.

6.4 Wind Tunnel Test

Proceeding into the first rounds of wind tunnel testing the preliminary dynamics model was already an evolution from the purely computationally derived dynamics. In particular, the identified dynamics of the servo actuators, the frequency-tuning adjustments to the finite element model, and the experimentally-determined structural damping ratios of Section 6.3 were all included to form what is called the “GVT” model (as this model incorporates all data collected up to and including Ground Vibration Tests). Figure 6.17 demonstrates the substantial features of the GVT-model by visualizing the elevator to wing-root strain transfer function. This figure guided the planned test scenarios of experimental validation. For example, the servo bandwidth (by design) does not encompass the second wing bending

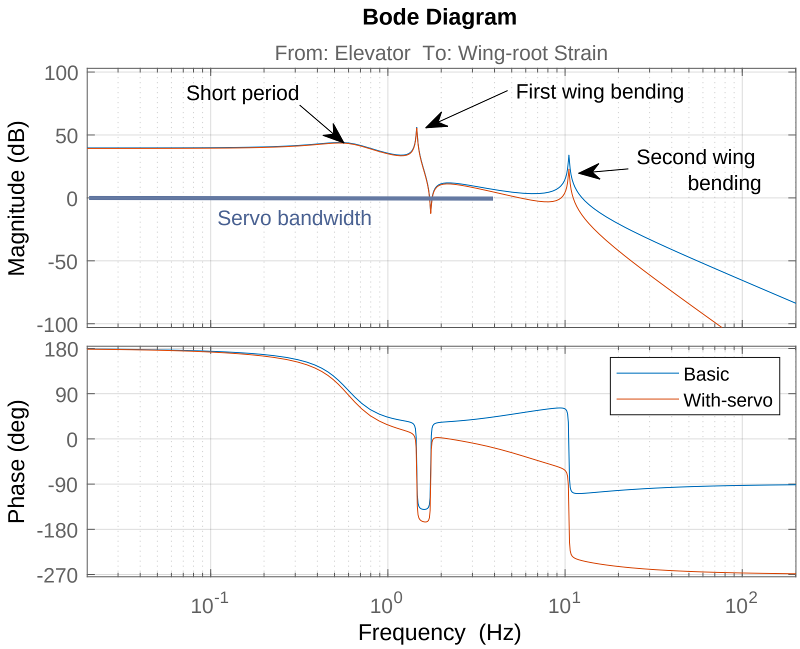

Figure 6.17: “GVT” model visualized with the elevator to wing-root strain transfer function and a comparison of changes due to servo dynamics.

natural frequency, so to perform any identification of the second wing bending frequency it must be energized by some other means. This can happen by either random excitation from wind tunnel turbulence or by an actuator impulse. On the other hand, the short period and first wing bending modes are within the servo bandwidth and should be identifiable with swept-sine actuator inputs; mirroring the process used in the servo system identification of Section 6.3. The sections to follow detail the results of targeted modal identification tests as well as an overall system dynamics identification.

6.4.1 First Wing Bending

The first targeted tests were conducted to validate the frequency and damping of the first wing bending mode. Of the many configurations tested, one of the best datasets for identification of the frequency of this mode is a series of aileron sine-sweeps conducted at varied amplitudes. Figure 6.18 shows the power spectral density estimates for the strain signal corresponding to the swept inputs of various amplitudes. The frequency at the power peak has an average of 1.39 Hz, with a standard deviation of 0.03 Hz. Comparing this value to the prediction shows the measured value is 0.06 Hz less than predicted; taking the measured value as truth, the GVT-model over-predicted this modal frequency by approximately 4.3%. The frequency of this mode did not significantly change as a function of dynamic pressure.

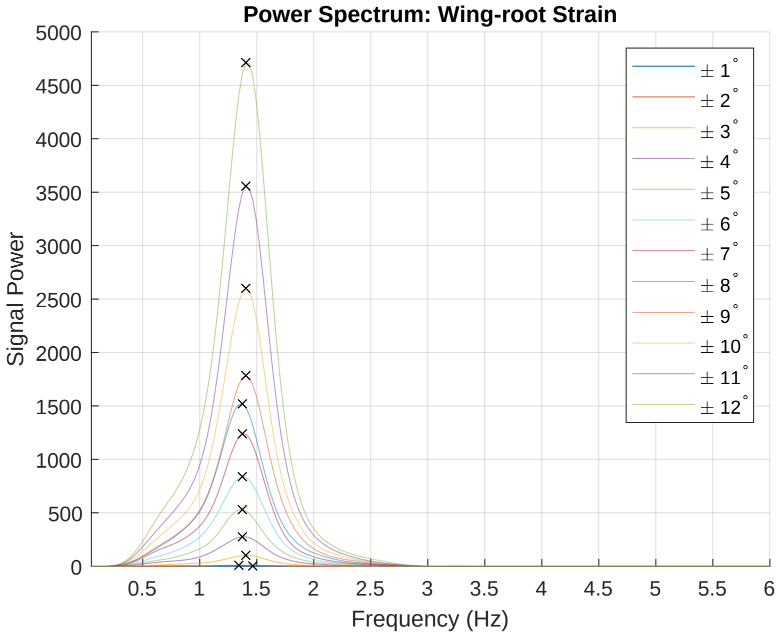

Figure 6.18: Power spectral density estimates used in first wing bending frequency identification.

To measure the damping ratio of the first wing bending mode, a dwell input was commanded near the expected first wing bending frequency and then abruptly stopped. Then, the exponential decay of wing bending motion was measured at the wing tip. Figure 6.19 demonstrates the input signal and corresponding laser-measured displacement for inboard aileron motion. Similar runs were conducted for the other actuators, but the results here are typical of the other runs. Figure 6.20a highlights the portion of the laser measurement signal immediately following the end of the dwell input and identifies the peaks used in estimating damping ratio with the logarithmic decrement method. These dwell runs were conducted at various dynamic pressures to determine if the effective damping was decreasing with speed.

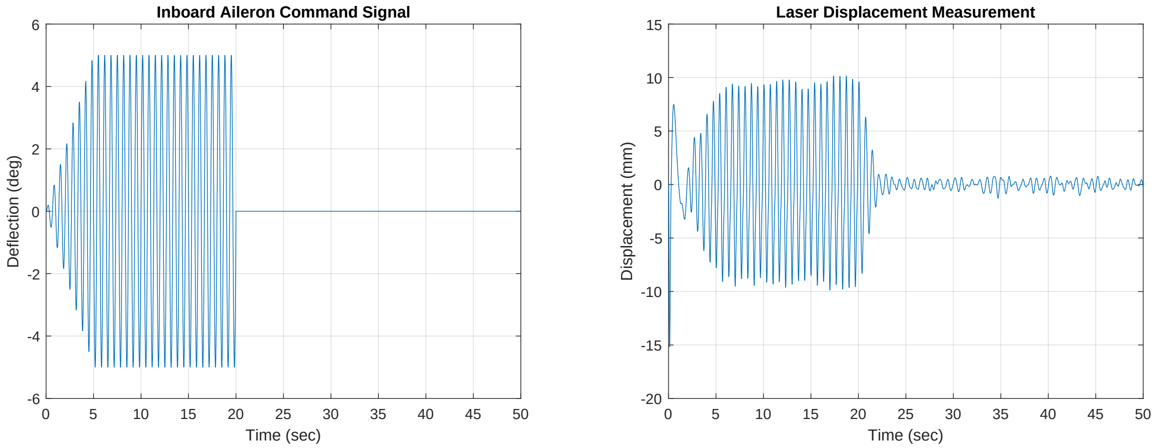

(a) Aileron dwell input signal (b) Laser measurement of wing displacement

Figure 6.19: Time histories of input and measurement signals used in dwell tests for identification of first wing bending damping ratio.

The GVT-model did not predict any substantial change in damping of the first structural mode with changes in dynamic pressure. However, in Fig. 6.20b the opposite is observed: the measured damping increases over the range of test speeds. Regardless of the trend, by either estimate the measured damping at maximum dynamic pressure is at least an order of magnitude greater than the damping predicted by the GVT-model (which recall was $\zeta = 0.005$). These results indicate that the unsteady aerodynamic damping not captured by the modeling method is significant and increasing over the range of test speeds.

6.4.2 Second Wing Bending

The second wing bending mode is not as amenable to identification as it resides outside the actuation bandwidth. From aileron pulse inputs the second wing bending frequency is only

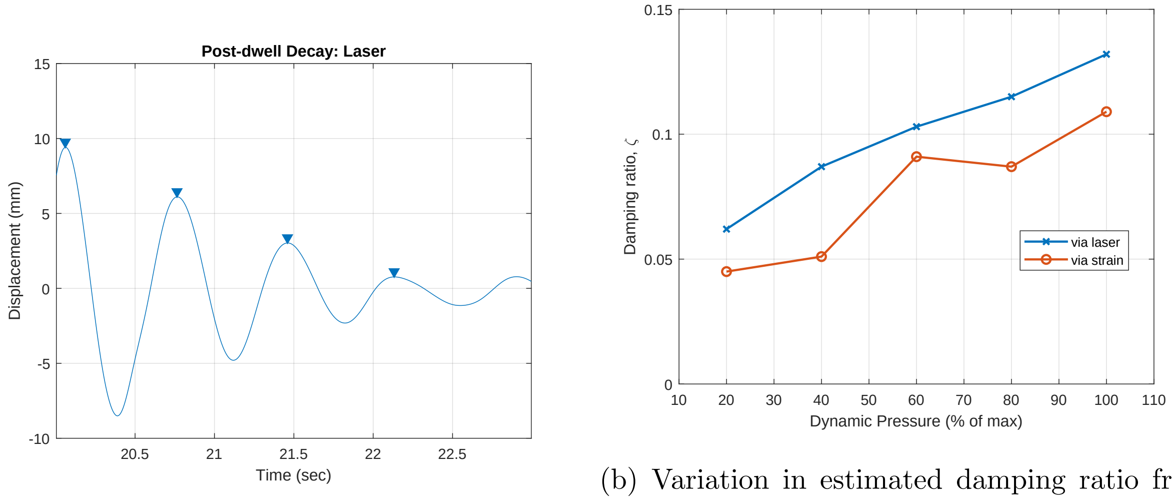

(a) Decay portion of laser measurement with peaks identified for estimation of damping ratio with the logarithmic decrement method.

(b) Variation in estimated damping ratio from inboard aileron dwell; trends presented for damping ratio based on decay of laser signal and wing strain gauge.

Figure 6.20: Logarithmic decrement based identification of the first wing bending damping ratio and its variation with dynamic pressure.

faintly detected and the inputs did not provide sufficient data to estimate a damping ratio for the mode. The predicted frequency for this mode was 10.5 Hz as depicted previously in Fig. 6.17. The identifiable peak in the power spectrum suggested a frequency of 10.3 Hz. Taking this to be the true frequency, the GVT-model overpredicted the second wing bending frequency by only 1.9%. The data used to generate the power spectrum was obtained at the maximum end of test speeds; no observations can be made regarding variation with dynamic pressure.

6.4.3 Short Period

The last round of targeted modal characterization tests were aimed at the short period mode. Recall this mode was expected to have the greatest discrepancy from the analytical model because the modeling method neglects the physical attachment of the test article to the mounting assembly. In fact, the original mounting assembly included a bearing with too much friction for the pitch dynamics to exhibit second order modal characteristics. The bearing and housing were re-designed to reduce rotational friction. Despite the improvement, the characterization of the short period mode is still not as straightforward as the previous two modes.

Figure 6.21a depicts the pitch angle response to a swept-sine elevator input at six different conditions of dynamic pressure. Note, the response amplitude is normalized in each case as the amplitude of the input had to be reduced with increasing dynamic pressure. The corresponding power spectra of these response signals are given in Fig. 6.21b. The series of plots in Fig. 6.21 demonstrate the natural frequency of the short period mode increasing with dynamic pressure. This movement of the rigid-body mode is beneficial as it yields a variety of system dynamics thus enriching the landscape of potential for control system investigations. At 60% of Q_{max} the short period frequency is 0.85 Hz (determined via power spectrum peak) and the mode's damping ratio is $\zeta = 0.2$ (determined via logarithmic decrement from dwell; the same procedure as used in measuring the first wing bending damping ratio).

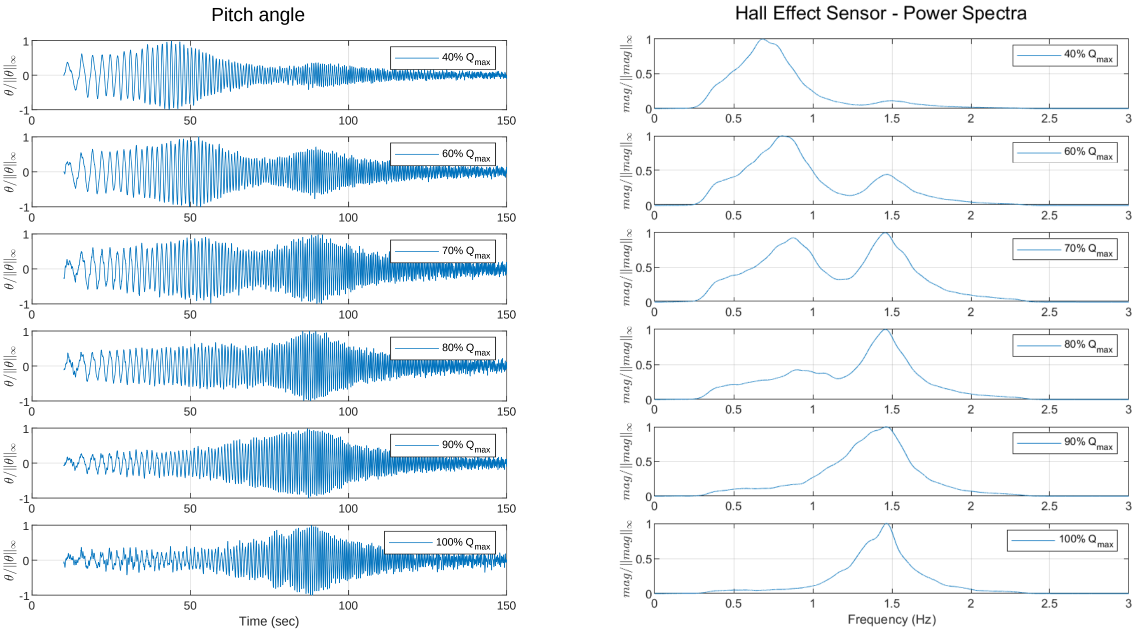

(a) Measurement time history from sine-sweep (b) Power spectra from sine-sweep

Figure 6.21: Movement of the rigid-body mode with increasing dynamic pressure.

6.4.4 Dynamic Model Adjustments

The test scenarios of the previous sections were conducted as a verification of anticipated modal characteristics. However, to be useful as a control system testing apparatus, a characterization of the complete system dynamics would be necessary. For the first round of design objectives the system with more distinct modes (in terms of frequency response) were most desirable, so the system at 60% total dynamic pressure was selected for additional model validation. With the dynamic pressure selected, three frequency sweeps were conducted (one sweep per control surface) to generate input/output relationships for parameterized system identification. Starting with the LTI state space model developed from NASTRAN and corrected with vibrometer data, the elements of the system matrices were allowed to vary in a nonlinear optimization to best fit the input/output relationships of the sweeps. In this parameter optimization the order and structure of the system remain fixed, so any elements which were zero to begin with, remain zero in the optimization. Figure 6.22 demonstrates a comparison between the adjusted model and the experimental data with selected transfer functions. One initial change from the original model to the adjusted model was a downscaling of the control surface effectiveness factors. This change was expected as the original factors were generated according to a doublet lattice aerodynamic model. However, the most impactful change had to do with the rigid-body mode. While the original model suggested the system would exhibit three modes each exciting only two states of the six state system, the adjusted model provides two modes (first wing bending and second wing bending) that follow expectation while the third mode includes substantial excitation of four states (two rigid-body and two structural).

Note that in addition to the three control surface inputs, a fourth input describes the angular displacement of a gust vane. The aeroelastic test article was subjected to a series of gust disturbances and the input-output data supplied to the parameter optimization process to obtain an effectiveness matrix column. The development, test, and modeling of the gust generation system are the details of other work, but Fig. 6.23 demonstrates that a simple effectiveness matrix column provides an excellent correspondence with the measured test article response from experiment. This is an encouraging result because it obviates the need for inclusion of unsteady aerodynamic modeling from gust system command to test article disturbance. In other words, the associated transfer function in Fig. 6.23 that maps gust system input (gust disturbance) to wing root strain can be used as the basis of comparison for active gust load alleviation techniques.

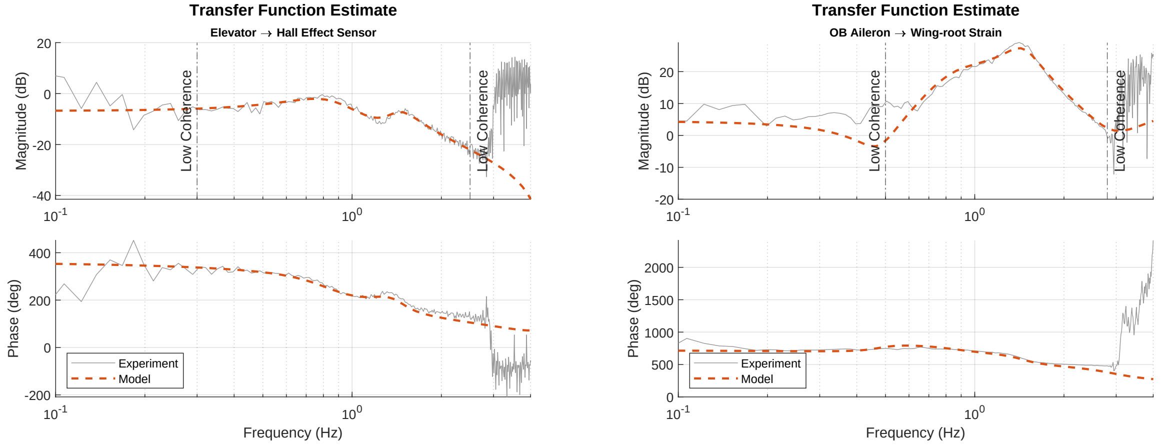

(a) Elevator (deg) to pitch angle (deg)
(b) Outboard aileron (deg) to wing root $\mu-$strain

Figure 6.22: Comparison of experimental frequency response functions to transfer functions of the adjusted analytical model; two of six input-output relationships shown.

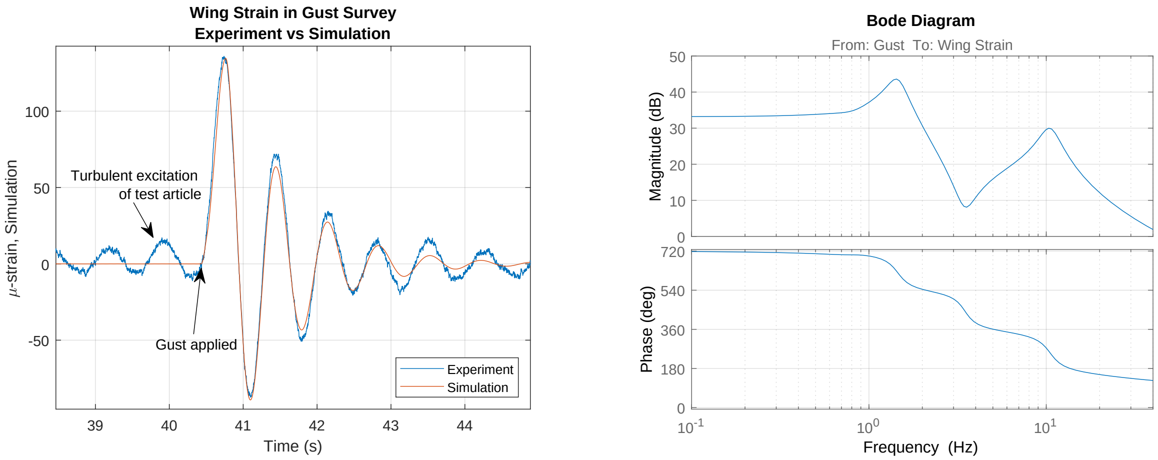

(a) Wing strain in response to gust input, simulation vs. experiment

(b) Transfer function: gust vane (deg) to wing strain ($\mu\epsilon$)

Figure 6.23: Gust input model comparison and transfer function to wing root strain.

Chapter 7

CONCLUSION

The growing challenges in control of flexible aircraft require commensurate growth in capability to analyze, simulate, and validate innovative flight control systems. The multi-controller architecture provides both a means forward in its familial relationship to the switched system framework, and a means backward to harness the success and experience of legacy point-wise designs. In that spirit, we have striven for the contributions of this work - from analyses of robustness for switched system stability guarantees to the simulation and test bed developments - to focus on the most practical means of advancement for flight control of flexible aircraft.

In Chapter 3 we sought to probe the existing stability margin for some measure of tolerable system perturbations. While the analysis did indeed yield conditions on such tolerable variations, one of the main outcomes was the reflection that tolerable perturbations under the Quadratic Stability Margin were limited to the directions spanned by the original system polytope. In order for the method to provide most useful information about perturbations of interest, candidate variations would need to be added to the original system polytope which could in turn trigger the need for the generation of a new QCLF. In other words, gauging tolerable perturbations under the QSM was found possible, but cumbersome.

The Quadratic Stability Margin was shed as a restriction in Chapter 4 where perturbations were taken in arbitrary directions. The real stability radius for an individual system served as a starting point for the discussion which gave rise to the constriction method and associated optimization problems. While it is advantageous that the induced norms allowed by the constriction method are comparable in form to the real stability radius, the optimizations that result from this approach either lack a guarantee of global minimum or require a degree of conservatism be introduced. The significance of these disadvantages are relative to the prescription of system uncertainty, i.e., if an induced norm on a matrix perturbation is the preferred measure of uncertainty for a given system design problem, then a constriction method may be the appropriate choice. On the other hand, it is fairly likely that the vector description of uncertainty and the ℓ_1 or ℓ_∞ norm are of interest. In these cases the expansion methods and their associated optimizations are more appropriate. In either case, the structure derived from common system architectures can be leveraged to simplify the optimization problems where system dimension may otherwise hinder the process.

Chapter 5 detailed our development of the Generic Wide Body aircraft model and its traits that make it particularly suitable to aid the creation, simulation, and evaluation of flight control laws for flexible aircraft. Publishing the model in the open literature as a completely un-reduced aero-structural model using the industry standard modeling language affords the opportunity to conduct sensitivity studies and to make modifications or extensions as new research directions unfold. For example, the un-reduced model provides an avenue for future work in which unsteady aerodynamic analysis can be used to generate higher fidelity control evaluation simulations or possibly conduct active flutter suppression research.

Finally, the aeroelastic wind tunnel model and real time control test apparatus detailed in Chapter 6 provide a gateway to aeroelastic control studies that would be otherwise burdened with the cost and complexity of traditional aeroelastic test beds. The modularity of the test article design, the simulation and hardware-in-the-loop software architecture, and the quick setup/teardown characteristic of the test bed all reflect our ambition to support rapid, low-cost maturation of control system theory to control system experiment. It is our hope that the test apparatus - in concert with the other contributions in this work - will catalyze academic and industry collaboration toward the advancement of flight control for flexible aircraft.

BIBLIOGRAPHY

[1] J. D. Anderson Jr., *Introduction to flight.* McGraw Hill, sixth ed., 2008.

[2] D. McRuer and D. Graham, "Flight control century: triumphs of the systems approach," *Journal of Guidance, Control, and Dynamics*, vol. 27, no. 2, pp. 161–173, 2004.

[3] R. D. Milne, "Dynamics of the deformable aeroplane," aeronautical research council reports and memoranda, University of London (Queen Mary College), 1964.

[4] R. D. Milne, "Some remarks on the dynamics of deformable bodies.," *AIAA Journal*, vol. 6, pp. 556–558, Mar. 1968.

[5] J. I. Arnold and F. B. Murphy, "B-52 control configured vehicles: Flight test results," 1976.

[6] D. McLean and R. Prasad, "A structure load alleviation control system for a large aircraft," *Transactions of the Institute of Measurement and Control*, vol. 2, no. 1, pp. 25–37, 1980.

[7] G. Bendixen, R. O'Connell, and C. Siegert, "Digital active control system for load alleviation for the lockheed l-1011," *The Aeronautical Journal*, vol. 85, no. 849, pp. 430–436, 1981.

[8] B. Moulin and M. Karpel, "Gust loads alleviation using special control surfaces," *Journal of Aircraft*, vol. 44, no. 1, pp. 17–25, 2007.

[9] H. Geisseler, M. Kopf, P. Varutti, T. Faulwasser, and R. Findeisen, "Model predictive control for gust load alleviation," in *Proc. IFAC Conf. Nonlinear Model Predictive Control*, pp. 27–32, 2012.

[10] A. Khalil and N. Fezans, "Performance enhancement of gust load alleviation systems for flexible aircraft using h-infinity optimal control with preview," in *AIAA Scitech 2019 Forum*, p. 0822, 2019.

[11] N. Aouf, B. Boulet, and R. Botez, "H-2 and h-infinty optimal gust load alleviation for a flexible aircraft," in *American Control Conference, 2000. Proceedings of the 2000*, vol. 3, pp. 1872–1876, IEEE, 2000.

[12] R. Botez, I. Boustani, N. Vayani, P. Bigras, and T. Wong, “Optimal control laws for gust alleviation,” *Canadian Aeronautics and Space Journal*, vol. 47, no. 1, pp. 1–6, 2001.

[13] E. Livne, “Aircraft active flutter suppression: State of the art and technology maturation needs,” *Journal of Aircraft*, vol. 55, no. 1, pp. 410–452, 2017.

[14] M. J. Abzug and E. E. Larrabee, *Airplane stability and control: a history of the technologies that made aviation possible*, vol. 14. Cambridge University Press, 2005.

[15] J. D. Blight, R. Lane Daily, and D. Gangsaas, “Practical control law design for aircraft using multivariable techniques,” *International Journal of Control*, vol. 59, no. 1, pp. 93–137, 1994.

[16] T. Hu, A. R. Teel, and L. Zaccarian, “Stability and performance for saturated systems via quadratic and nonquadratic lyapunov functions,” *IEEE Transactions on Automatic Control*, vol. 51, no. 11, pp. 1770–1786, 2006.

[17] J. Zeng, S. Kukreja, and B. Moulin, “Experimental model-based aeroelastic control for flutter suppression and gust-load alleviation,” *Journal of Guidance, Control, and Dynamics*, vol. 35, no. 5, pp. 1377–1390, 2012.

[18] S. Ricci, A. De Gaspari, L. Riccobene, and F. Fonte, “Design and wind tunnel test validation of gust load alleviation systems,” in *58th AIAA/ASCE/AHS/ASC Structures, Structural Dynamics, and Materials Conference*, p. 1818, 2017.

[19] P. Chandrasekharan, *Robust control of linear dynamical systems.* Academic Press, 1996.

[20] D. Hinrichsen and A. J. Pritchard, “Stability radii of linear systems,” *Systems & Control Letters*, vol. 7, no. 1, pp. 1–10, 1986.

[21] D. Hinrichsen and A. J. Pritchard, “Stability radius for structured perturbations and the algebraic riccati equation,” *Systems & Control Letters*, vol. 8, no. 2, pp. 105–113, 1986.

[22] S. Banda, J. Bowlus, R. Robinson, R. Adams, K. Hammett, W. Reigelsperger, M. Barrett, P. Blue, D. Bugajski, D. Enns, R. Hendrick, M. Jackson, B. Morton, G. Stein, J. Bessollo, J. Virnig, G. Walker, R. Colgren, P. Tait, and R. Smith, “Application of multivariable control theory to aircraft control laws,” Tech. Rep. WL-TR-96-3099, USAF Wright Laboratory Flight Dynamics Directorate, Wright-Patterson Air Force Base, OH 45433-7562, May 1996.

[23] D. Hinrichsen and A. J. Pritchard, "Real and complex stability radii: a survey," in *Control of uncertain systems*, pp. 119–162, Springer, 1990.

[24] G. Golub, S. Nash, and C. Van Loan, "A hessenberg-schur method for the problem ax+ xb= c," *IEEE Transactions on Automatic Control*, vol. 24, no. 6, pp. 909–913, 1979.

[25] E. A. Jonckheere, "New bound on the sensitivity of the solution of the lyapunov equation," *Linear algebra and its applications*, vol. 60, pp. 57–64, 1984.

[26] G. Hewer and C. Kenney, "The sensitivity of the stable lyapunov equation," *SIAM journal on control and optimization*, vol. 26, no. 2, pp. 321–344, 1988.

[27] R. Yedavalli, "Improved measures of stability robustness for linear state space models," *IEEE Transactions on Automatic Control*, vol. 30, no. 6, pp. 577–579, 1985.

[28] P.-A. Bliman, "A convex approach to robust stability for linear systems with uncertain scalar parameters," *SIAM Journal on Control and Optimization*, vol. 42, no. 6, pp. 2016–2042, 2004.

[29] G. Chesi, "Establishing stability and instability of matrix hypercubes," *Systems & control letters*, vol. 54, no. 4, pp. 381–388, 2005.

[30] D. J. Leith and W. E. Leithead, "Survey of gain-scheduling analysis and design," *International Journal of Control*, vol. 73, no. 11, pp. 1001–1025, 2000.

[31] F. Blanchini, P. Colaneri, and F. A. Pellegrino, "Simultaneous performance achievement via compensator blending," *Automatica*, vol. 44, no. 1, pp. 1–14, 2008.

[32] R. W. Pratt, ed., *Flight Control Systems practical issues in design and implementation.* The Institution of Electrical Engineers and The American Institute of Aeronautics and Astronautics, 2000.

[33] D. Leith, R. N. Shorten, W. Leithead, O. Mason, and P. Curran, "Issues in the design of switched linear control systems: A benchmark study," *International Journal of Adaptive Control and Signal Processing*, vol. 17, no. 2, pp. 103–118, 2003.

[34] R. Shorten, F. Wirth, O. Mason, K. Wulff, and C. King, "Stability criteria for switched and hybrid systems," *SIAM review*, vol. 49, no. 4, pp. 545–592, 2007.

[35] D. Liberzon, *Switching in systems and control.* Springer Science & Business Media, 2012.

[36] H. Lin and P. J. Antsaklis, “Stability and stabilizability of switched linear systems: a survey of recent results,” *IEEE Transactions on Automatic control*, vol. 54, no. 2, pp. 308–322, 2009.

[37] J. P. Hespanha and S. A. Morse, “Switching between stabilizing controllers,” *Automatica*, vol. 38, no. 11, pp. 1905 – 1917, 2002.

[38] S. Sajja, S. Solmaz, R. Shorten, and M. Corless, “Preservation of common quadratic lyapunov functions and padé approximations,” in *Decision and Control (CDC), 2010 49th IEEE Conference on*, pp. 7334–7338, IEEE, 2010.

[39] R. H. Ordóñez-Hurtado and M. A. Duarte-Mermoud, “Finding common quadratic lyapunov functions for switched linear systems using particle swarm optimisation,” *International Journal of Control*, vol. 85, no. 1, pp. 12–25, 2012.

[40] D. Liberzon and R. Tempo, “Common lyapunov functions and gradient algorithms,” *IEEE Transactions on Automatic Control*, vol. 49, no. 6, pp. 990–994, 2004.

[41] S. Boyd, L. El Ghaoui, E. Feron, and V. Balakrishnan, *Linear matrix inequalities in system and control theory.* SIAM, 1994.

[42] D. Schmidt, *Modern flight dynamics.* McGraw-Hill Higher Education, 2012.

[43] D. McLean, *Automatic flight control systems.* Englewood Cliffs, NJ: Prentice Hall, 1990.

[44] J. R. Wright and J. E. Cooper, *Introduction to Aircraft Aeroelasticity and Loads.* John Wiley & Sons, INC., 2007.

[45] C. M. Shearer and C. E. Cesnik, “Nonlinear flight dynamics of very flexible aircraft,” *Journal of Aircraft*, vol. 44, no. 5, pp. 1528–1545, 2007.

[46] T. R. Quackenbush, J. Keller, A. H. Boschitsch, G. Whitehouse, and R. McKillip, “Modeling tools for real time aeroservoelastic simulation with nonlinear aerodynamics,” in *AIAA Atmospheric Flizht Mechanics Conference. Chicago*, pp. 1–18, 2009.

[47] S. P. Andrews, *Modelling and simulation of flexible aircraft: handling qualities with active load control.* PhD thesis, Cranfield University, 2011.

[48] D. K. Schmidt, “A non-linear simulink simulation of a large, flexible aircraft - flexsim.” Supported by MUSYN, Inc., and NASA Dryden Flight Research Center, March 2013.

[49] D. L. Hull and K. L. Roger, “B-52e ccv flight test data applicable to parameter estimation,” Tech. Rep. AFFDL-TR-75-131, United States Air Force, Air Force Flight Dynamics Laboratory, Wright-Patterson Air Force Base, Ohio, 1975.

[50] D. McLean, “Gust-alleviation control systems for aircraft,” in *Proceedings of the Institution of Electrical Engineers*, vol. 125, pp. 675–685, IET, 1978.

[51] N. Aouf, B. Boulet, and R. Botez, “Robust gust load alleviation for a flexible aircraft,” *Canadian Aeronautics and Space Journal*, vol. 46, no. 3, pp. 131–139, 2000.

[52] G. Ward and U.-L. Ly, “Stability augmentation design of a large flexible transport using nonlinear parameter optimization,” *Journal of Guidance, Control, and Dynamics*, vol. 19, March-April 1996.

[53] J. Becker, H. Lusebrink, and F. Weiss, “Gust load alleviation on airbus a-300,” in *Proceedings of the Congress of the International Council of the Aeronautical Sciences*, vol. 13, p. 44, Spartan Books; London, 1982.

[54] N. Nguyen, E. Ting, D. Nguyen, T. Dao, and K. Trinh, “Coupled vortex-lattice flight dynamic model with aeroelastic finite-element model of flexible wing transport aircraft with variable camber continuous trailing edge flap for drag reduction,” *AIAA Atmospheric Flight Mechanics, AIAA Paper*, vol. 4746, p. 2013, 2013.

[55] Zona-Technology, “Zaero theoretical manual,” Scottsdale, AZ 85258, June 2011. Version 8.5.

[56] B. Hinson, N. Powel, J. Quenzer, and K. Morgansen, “Observability-based guidance algorithm for navigation using a single ranging beacon,” in *Robotics: Science and Systems, Workshop on Autonomous Control, Adaptation, and Learning for Underwater Vehicles*, (Berkley, CA, USA), July 2014.

[57] J. Quenzer and K. Morgansen, “Observability based control in range-only underwater vehicle localization,” in *2014 American Control Conference*, pp. 4702–4707, IEEE, 2014.

[58] A. Wolek, J. Burns, C. Woolsey, J. Quenzer, L. Techy, and K. Morgansen, “A maneuverable, pneumatic underwater glider,” in *2012 Oceans*, pp. 1–7, IEEE, 2012.

[59] J. Quenzer, B. Barzgaran, K. Morgansen, and M. Mesbahi, “Quadratic stability margin in switched control system design,” in *2018 Annual American Control Conference (ACC)*, pp. 4564–4569, IEEE, 2018.

[60] J. Quenzer and K. Morgansen, “Robustness of quadratic stability guarantees for multi-controller systems,” *AIAA Journal of Guidance Dynamics and Control*, in preparation.

[61] L. Techy, R. Tomokiyo, J. Quenzer, T. Beauchamp, and K. Morgansen, “Full-scale wind tunnel study of the seaglider underwater glider,” in *Technical report*, University of Washington, Aeronautics & Astronautics, 2010.

[62] A. Wolek, T. Gode, C. A. Woolsey, J. Quenzer, and K. Morgansen, “Testing a pneumatic underwater glider in shallow water,” in *OCEANS 2015-MTS/IEEE Washington*, pp. 1–8, IEEE, 2015.

[63] J. Quenzer, B. Barzgaran, M. Mesbahi, and K. Morgansen, “The generic wide body aircraft model,” in *2018 AIAA Guidance, Navigation, and Control Conference*, p. 0877, American Institute of Aeronautics and Astronautics, Jan. 2018.

[64] J. Quenzer, A. Zongolowicz, K. A. Hinson, B. Barzgaran, E. Livne, M. Mesbahi, and K. Morgansen, “Model for aeroelastic response to gust excitation,” in *AIAA Scitech 2019 Forum*, p. 2031, 2019.

[65] J. Quenzer, B. Barzgaran, A. Zongolowicz, K. Hinson, M. Mesbahi, K. Morgansen, and E. Livne, “Low-cost wind tunnel studies of gust alleviation control techniques,” in *International Forum on Aeroelasticity and Structural Dynamics*, 2019. Accepted.

[66] B. Grünbaum, *Convex Polytopes*, vol. 221 of *Graduate Texts in Mathematics*. Springer-Verlag New York, 2 ed., 2003.

[67] C. D. Meyer, *Matrix analysis and applied linear algebra*, vol. 71. Siam, 2000.

[68] R. A. Horn, R. A. Horn, and C. R. Johnson, *Matrix analysis*. Cambridge university press, 1990.

[69] Y. Saad and M. H. Schultz, “Topological properties of hypercubes,” *IEEE Transactions on computers*, vol. 37, no. 7, pp. 867–872, 1988.

[70] L. Qiu, B. Bernhardsson, A. Rantzer, E. Davison, P. Young, and J. Doyle, “A formula for computation of the real stability radius,” *Automatica*, vol. 31, no. 6, pp. 879–890, 1995.

[71] J. Löfberg, “Yalmip : A toolbox for modeling and optimization in matlab,” in *In Proceedings of the CACSD Conference*, (Taipei, Taiwan), 2004.

[72] I. CVX Research, "CVX: Matlab software for disciplined convex programming, version 2.0." `http://cvxr.com/cvx`, Aug. 2012.

[73] M. Grant and S. Boyd, "Graph implementations for nonsmooth convex programs," in *Recent Advances in Learning and Control* (V. Blondel, S. Boyd, and H. Kimura, eds.), Lecture Notes in Control and Information Sciences, pp. 95–110, Springer-Verlag Limited, 2008. "`http://stanford.edu/~boyd/graph\_dcp.html`".

[74] L. V. Schmidt, *Introduction to aircraft flight dynamics.* American Institute of Aeronautics and Astronautics, 1998.

[75] H. A. Mooij, *Criteria for low-speed longitudinal handling qualities of transport aircraft with closed-loop flight control systems.* M. Nijhoff for Nationaal Lucht-en Ruimtevaart-laboratorium, National Aerospace Laboratory, NLR, The Netherlands, 1985.

[76] F. M. Hoblit, *Gust loads on aircraft: concepts and applications.* American Institute of Aeronautics and Astronautics, 1988.

[77] B. Etkin and L. D. Reid, *Dynamics of flight: stability and control*, vol. 3. Wiley New York, 1996.

[78] T. L. Lomax, *Structural loads analysis for commercial transport aircraft: theory and practice.* American Institute of Aeronautics and Astronautics, 1996.

[79] D. P. Raymer, *Aircraft Design: A Conceptual Approach.* AIAA Education Series, American Institute of Aeronautics and Astronautics, fourth ed., 2006.

[80] W. F. Phillips, *Mechanics of Flight.* John Wiley & Sons, INC., 2nd ed., 2010.

[81] E. Albano and W. P. Rodden, "A doublet-lattice method for calculating lift distributions on oscillating surfaces in subsonic flows.," *AIAA journal*, vol. 7, no. 2, pp. 279–285, 1969.

[82] P. A. Jackson, K. Munson, and L. Peacock, *Jane's all the world's aircraft 2011-2012.* Jane's Information Group, 2011.

[83] "777-200lr/-300er/-freighter airplane characteristics for airport planning." `http://www.boeing.com/assets/pdf/commercial/airports/acaps/777_2lr3er.pdf`, 2015.

[84] L. Cavagna, S. Ricci, and L. Riccobene, "A fast tool for structural sizing, aeroelastic analysis and optimization in aircraft conceptual design," in *50th AIAA/ASME/ASCE/AHS/ASC Structures, Structural Dynamics, and Materials Conference 17th AIAA/ASME/AHS Adaptive Structures Conference 11th AIAA No*, p. 2571, 2009.

[85] MSC.Software, MSC.Software Corporation 4675 MacArthur Court, Suite 900 Newport Beach, CA 92660, *MSC Nastran 2013.1 Quick Reference Guide*, Nov. 2013.

[86] MSC.Software, MSC.Software Corporation 2 MacArthur Place Santa Ana, CA 92707, *MSC Nastran Version 68 Aeroelastic Analysis User's Guide*, Jan. 2010.

[87] R. G. Budynas, *Roark's Formulas for Stress and Strain, 7th Edition.* McGraw-Hill, New York, 2002.

[88] R. G. Budynas, *Advanced strength and applied stress analysis.* WCB/McGraw-Hill, 1999.

[89] C.-T. Chen, *Linear System Theory and Design.* Oxford University Press, 3 ed., 1999.

Appendix A

OBSERVABLE CANONICAL FORM

For a linear time-invariant system with a transfer function

$$\frac{Y(s)}{U(s)} = \frac{b_0 s^n + b_1 s^{n-1} + ... + b_{n-1} s + b_n}{s^n + a_1 s^{n-1} + ... + a_{n-1} s + a_n},$$

the observable canonical realization is reported in [89] as

$$\begin{bmatrix} \dot{x}_1 \\ \dot{x}_2 \\ \vdots \\ \dot{x}_n \end{bmatrix} = \begin{bmatrix} 0 & 0 & \cdots & 0 & -a_n \\ 1 & 0 & \cdots & 0 & -a_{n-1} \\ \vdots & \vdots & & \vdots & \vdots \\ 0 & 0 & \cdots & 1 & -a_1 \end{bmatrix} \begin{bmatrix} x_1 \\ x_2 \\ \vdots \\ x_n \end{bmatrix} + \begin{bmatrix} b_n - a_n b_0 \\ b_{n-1} - a_{n-1} b_0 \\ \vdots \\ b_1 - a_1 b_0 \end{bmatrix} u$$

$$y = \begin{bmatrix} 0 & 0 & \cdots & 0 & 1 \end{bmatrix} \begin{bmatrix} x_1 \\ x_2 \\ \vdots \\ x_n \end{bmatrix} + b_0 u.$$